FORMATION PATHWAYS AND PHYSICOCHEMICAL PROPERTIES OF AEROSOLS PRODUCED UNDER LOW TEMPERATURE COMBUSTION (LTC) CONDITIONS

by

OMAR EL HAJJ

(Under the Direction of Rawad Saleh)

ABSTRACT

Low-temperature combustion (LTC) represents a promising technology being deployed in emerging advanced compression ignition (ACI) engines. These engines have the potential to reach higher thermal efficiencies and substantially reduce $NO_x$ and particulate soot (i.e., elemental carbon) emissions. For certain hydrocarbon fuels, LTC is dominated by chain-branching reactions involving peroxy radicals ($RO_2$) within the 500K – 700K temperature range. This reaction sequence aligns with a phase referred to as low-temperature heat release (LTHR) or 'cool flame', causing the fuel to display two-stage ignition characteristics. This distinctive behavior plays a vital role in defining autoignition timing and, consequently, the comprehensive performance of ACI engines. This dissertation presents our findings on the formation of 'first-stage organic aerosols (OA)' that occur within the same temperature range as LTHR. We demonstrate, through a series of online and offline measurements, that first-stage OA have fundamentally different formation pathways than what is traditionally recognized for second-stage OA, or incipient soot, that forms at relatively higher temperatures (>1000K). We further established that first-stage OA is comprised of highly oxygenated compounds we refer to as oxygenated primary organic aerosols (OxyPOA), which retains chemical properties similar to

those of secondary organic aerosols (SOA). We also provide evidence of OxyPOA in emissions from spark-ignition and ACI engines, illustrating the relevance of elucidating OxyPOA formation to understanding OA pollution in current and future urban atmospheres. Motivated by the necessity of fuel additives in ACI engines that inhibit radical formation to reduce LTHR and enhance autoignition timing, we extended our investigation to include three additives with differing inhibitory capacities. We mixed each additive with a two-stage ignition fuel, to investigate their effects on the formation of first-stage OA. The results demonstrated that additives with a stronger inhibitory nature were more successful in suppressing first-stage OA formation. Furthermore, each additive displayed unique influences on the chemical makeup of the resulting first-stage OA.

INDEX WORDS: Aerosols, Low temperature combustion (LTC), Advanced compression ignition (ACI), combustion emissions

# FORMATION PATHWAYS AND PHYSICOCHEMICAL PROPERTIES OF AEROSOLS PRODUCED UNDER LOW TEMPERATURE COMBUSTION (LTC) CONDITIONS

by

OMAR EL HAJJ

B.E., Beirut Arab University, Lebanon, 2015

M.E., American University of Beirut, Lebanon, 2018

A Dissertation Submitted to the Graduate Faculty of the University of Georgia in Partial Fulfillment of the Requirements for the Degree

DOCTOR OF PHILOSOPHY

ATHENS, GEORGIA

2023

# FORMATION PATHWAYS AND PHYSICOCHEMICAL PROPERTIES OF AEROSOLS PRODUCED UNDER LOW TEMPERATURE COMBUSTION (LTC) CONDITIONS

by

OMAR EL HAJJ

| | |
|---|---|
| Major Professor: | Rawad Saleh |
| Committee: | Brandon Rotavera |
| | Geoffrey Smith |
| | R. Benjamin Davis |

Electronic Version Approved:

Ron Walcott
Vice Provost for Graduate Education and Dean of the Graduate School
The University of Georgia
August 2023

# DEDICATION

To my family.

# ACKNOWLEDGEMENTS

I am immensely thankful to my advisor Dr. Rawad Saleh, whose expertise and unswerving dedication have immeasurably enriched my scholarly journey. Our discussions were a constant source of learning. I deeply appreciate Dr. Saleh's mentorship and the significant role it has played in my academic pursuits.

My sincere appreciation goes to my PhD committee members, Dr. Brandon Rotavera, Dr. Geoffrey Smith, and Dr. Benjamin Davis. The valuable insights provided by Dr. Rotavera were key in refining and finalizing this work.

I am profoundly grateful to all the lab members who provided invaluable help in my research and contributed to a wonderful work environment. Many thanks to all the graduate students on the third floor of STEM-1 for the stimulating discussions and the collaborative atmosphere they fostered.

Finally, I'd like to extend heartfelt thanks to my mother, father, sister, and brother. Their support, love, and understanding have been indispensable. Shao, I can't express how much your companionship made everything bearable and even enjoyable, your support and love go far beyond anything I could have ever imagined or asked for.

TABLE OF CONTENTS

Page

LIST OF TABLES

Page

LIST OF FIGURES

Page

# CHAPTER 1

# INTRODUCTION

## 1.1. Background

There are more than one billion cars on the road today, 99% of which are powered by an internal combustion engine (ICE) (Chesterton, 2018). ICEs operating on fossil fuels consume about 25% of the world's energy (about 3000 out of 13,000 million tons oil equivalent per year) (Reitz et al., 2020). The U.S. Energy Information Agency (EIA) reported in its annual energy outlook 2022 that the projection in the year 2050 of hydrocarbon and biofuel combustion would still be 97% of the total transportation energy consumed (Nalley & LaRose, 2022). Stringent emissions regulations imposed to lower carbon footprints and the impact of other pollutants on the environment and human health, require new ICE technologies that deliver higher conversion energy and lower emissions. Advanced compression ignition (ACI) technology, which relies on low-temperature combustion (LTC), has been proposed as a next-generation strategy in internal combustion engines. A range of ACI modes have been shown experimentally to offer high brake thermal efficiency with low soot and NOx emissions compared to conventional compression ignition engines (Bedoya et al., 2012; Reitz & Duraisamy, 2015). Several research efforts are focusing on the integration of new biofuels with new ACI engine technologies, such as the U.S. DOE Co-Optimization of Fuels and Engines (Co-Optima) program and the Spark Controlled Compression Ignition (SPCCI) approach in Mazda's Skyactiv-X engines. Combustion particulate (aerosol) emissions affect the quality of the air we breathe and are the most potent in terms of health (Donaldson et al., 2005; Lawal et al., 2016; Mazzoli-Rocha et al., 2014) and climate

impacts (Bond et al., 2013; Pachauri et al., 2014) compared to other kinds of atmospheric aerosols. Thanks to major advancements in control technologies prompted by increasingly stringent regulation, the contribution of vehicle emissions to atmospheric aerosols has decreased significantly over the past few decades (Berggren & Magnusson, 2012). However, vehicle emissions still constitute an important fraction of atmospheric aerosols in urban regions (Calderón-Garcidueñas & Ayala, 2022). A product of a series of complex chemical and physical processes (Johansson et al., 2018; Michelsen, 2017; Wang, 2011), combustion aerosols are comprised of a multitude of carbonaceous compounds with poorly characterized chemical and physical properties. There are major gaps in our understanding of the formation of these aerosols, and the gaps grow wider when advanced biofuels and LTC technologies are in question. As will be discussed later, LTC systems feature lower temperatures and higher pressures than conventional systems (Heywood & Welling, 2009; Silke et al., 2009; Yao et al., 2009) and are expected to produce substantially different aerosol and gaseous emission profiles than conventional combustion systems. Consequently, while the technology behind biofuel low-temperature combustion has been rapidly developing, there is a lack of understanding of the pollution formed under LTC conditions. This leads to uncertainty in how an anticipated large-scale shift towards such systems impacts public-health and climate patterns.

### 1.2. Low temperature combustion (LTC)

Compression ignition (CI) engines suffer from high emissions of NOx and soot aerosols. These emissions have been significantly reduced in the last two decades by employing in-cylinder emission reduction strategies such as exhaust gas recirculation (EGR), higher fuel injection pressure, and varying fuel injection timing (Ahire et al., 2021). For current and future emission standards, these modifications need to be combined with exhaust after-treatment devices to

further decrease emissions which adds new challenges like higher cost, durability issues and larger space requirements in comparison to the engines without exhaust after-treatment technologies (Ahire et al., 2021). Therefore, in-cylinder combustion strategies need to be significantly improved for higher thermal efficiency as well as further reduction in engine-out emissions so that dependence on the aftertreatment technologies can also be reduced.

Advanced compression-ignition (ACI) is a next-generation strategy in internal combustion engines that aims to achieve high efficiency while maintaining low levels of pollution emissions (Dec, 2009; Dec & Hwang, 2009; Moses-DeBusk et al., 2019). Several ACI technologies have been proposed, including homogeneous charge compression-ignition (HCCI), premixed charge compression ignition (PCCI) (Epping et al., 2002; Stanglmaier & Roberts, 1999; Thring, 1989; Zhao et al., 2003), and reactivity controlled compression-ignition (RCCI) (Reitz & Duraisamy, 2015; Splitter et al., 2011), as well as concepts that combine different ACI strategies (Kang et al., 2019; Ortiz-Soto et al., 2019). All these approaches rely on low-temperature combustion (LTC) to reduce pollutant emissions by avoiding the NOx-soot tradeoff that occurs at the combustion conditions typical for conventional diesel combustion (CDC) (Agarwal et al., 2017; Han, 2013). Autoignition and combustion timing are major obstacles impeding ACI development and constricting its operating range (Maurya et al., 2018; Saxena & Bedoya, 2013). Autoignition is defined as the ignition of the air-fuel mixture because of the heat produced from exothermic oxidation reactions without the use of an external heat source such as spark plugs (Affens & Sheinson, 1980; Machrafi, 2010). The autoignition behavior in ACI engines is predominantly influenced by low temperature chemical kinetics, wherein the molecular structure of the fuel has a significant impact. Certain hydrocarbon fuels undergo a sequence of chain branching reactions at low temperatures (<850 K), involving H-abstraction and isomerization of alkyl ($RO_2$) radicals

(Westbrook, 2000). These chain reactions eventually release OH radicals, which contribute to the observed heat release during LTC, known as low temperature heat release (LTHR) (Saxena & Bedoya, 2013; Westbrook, 2000). Fuels characterized by longer and linear structures containing higher proportion of secondary C-H bonds, demonstrate an enhanced rate of isomerization. Therefore, these fuels exhibit a more pronounced low temperature heat release (LTHR) compared to fuels with branched structures (Curran et al., 1998; Lu et al., 2011; Ranzi et al., 1995; Ribaucour et al., 2000; Saxena & Bedoya, 2013). Those fuels exhibiting a low temperature heat release (LTHR) are classified as two-stage ignition fuels. The time delay between the two stages is known as the negative temperature coefficient (NTC). The second stage, or the main autoignition phase, involves the breakdown of hydrogen peroxide ($H_2O_2$) that accumulated during NTC at a temperature of around 1000 K, which releases large amounts of OH radicals, consequently instigating a further temperature increase. The occurrence of LTHR in two-stage ignition fuel prompts a progression in the combustion phasing, leading to an earlier onset of the second stage ignition (Saxena & Bedoya, 2013; Westbrook, 2000).

### 1.3. Fuel additives in ACI

In ACI combustion, the selected fuels need to exhibit a broad spectrum of auto-ignition properties to accommodate a wide range of operations. Given ACI's dependence on autoignition, fuels with high reactivity and low octane ratings can provide a benefit due to their decreased resistance to autoignition. However, their usability can be constrained during high engine loads with fuel-rich conditions due to the high LTHR, leading to excessively early ignition and knock tendencies for richer fuel/air mixture (Peng et al., 2005). Conversely, fuels with a high-octane rating (i.e., low reactivity) could potentially counteract this issue. Still, they underperform during lower loads and cold start conditions (Lu et al., 2011; Maurya et al., 2018).

The use of fuel blends and additives has been proposed as an effective approach to expand the operational range of ACI. Combining fuels with contrasting reactivities or introducing additives into a two-stage base fuel can effectively suppress the formation of OH radicals, and thus delaying the onset of the main ignition phase. Shibata et al. (Shibata et al., 2005) defined this effect as the "LTHR inhibitor effect."

Primary reference fuels (PRFs) are a very common example of blending two fuels with different reactivities to generate mixtures with varying autoignition properties and are used to estimate research octane numbers (RON) and knocking tendencies for fuels in engines. PRFs are blends of *n*-heptane, a straight-chain alkane with a characteristic two-stage ignition behavior and LTHR, which carries a RON value of 0, and isooctane, a branched-chain alkane known for its single-stage ignition behavior, assigned a RON value of 100. The ratio of isooctane in a PRF blend has a direct impact on its autoignition properties. By increasing the isooctane content, the LTHR decreases linearly, resulting in a corresponding linear increase of the RON (Lu et al., 2011; Machrafi, 2008; Tanaka et al., 2003; Waqas et al., 2018). Additives that display similar behavior of inhibiting LTC reactivity include ethanol, methanol, toluene, and *n*-butanol (Hashimoto, 2007; Herrmann et al., 2014; Lee et al., 2019; Lu et al., 2011; Lü et al., 2006; Machrafi, 2008; Saisirirat et al., 2010; Saisirirat et al., 2011; Shibata & Urushihara, 2007; Waqas et al., 2018). In addition to some advanced biofuels that demonstrated superior octane boosting capabilities such as dimethyl ether (DME) (Burke et al., 2015; Herrmann et al., 2014; Rodriguez et al., 2015) and furan derivatives, including 2-methylfuran (2-MF) (Alexandrino, 2020; Singh et al., 2018) and 2,5-dimethylfuran (DMF) (Alexandrino, 2020; Chen et al., 2013; Fioroni et al., 2022; Liu et al., 2013).

The enhancements in autoignition these additives offer can be credited to their proficiency in radical scavenging. Take DMF and ethanol as examples—both induce a non-linear decrease in LTHR when incorporated as additives. Yet, DMF provides more reaction pathways that consume LTC radicals, leading to a more pronounced non-linearity than ethanol, which ultimately translates to superior octane boosting efficiency (Fioroni et al., 2022). This characteristic is responsible for the synergistic behavior certain inhibitors show for RON when used as additives. Synergistic blending refers to the phenomenon where the addition of these compounds results in higher RON values than what would be expected based on a linear-blending model. On the other hand, some additives show an antagonistic blending behavior, where the blend RON is less than that predicted by a linear-blending model (Anderson et al., 2012; Foong et al., 2014; McCormick et al., 2017; Yuan et al., 2017). For instance, ethanol blend synergistically with isooctane, *n*-heptane, *n*-pentane, cyclopentane, and *n*-hexene but antagonistically with toluene (Badra et al., 2017; Foong et al., 2014). Both 2MF and DMF have been observed in several studies to have a significantly larger synergistic effect than ethanol (Christensen et al., 2011; Fioroni et al., 2022; McCormick et al., 2017; Singh et al., 2018).

### 1.4. Aerosol Characterization in LTC

Generally, in combustion literature, the terms ‘soot’ or ‘particulate matter (PM)’ are used to describe aerosol combustion emissions that are comprised of solid aggregates of elemental carbon (EC) that are linked to the main stage ignition. The mechanisms of aerosol formation during the second ignition stage (> 1000 K) are well established as part of the soot formation process. This initiates with the formation of small aromatic species which grow into polycyclic aromatic hydrocarbons (PAHs). Through the assistance of radical chain reactions, these PAHs amalgamate with other hydrocarbons to spawn condensable organic aerosols (OA), signifying

the initial stage of incipient soot formation (Frenklach & Wang, 1991; Michelsen, 2017; Wang, 2011). As temperature rises, these OAs undergo a series of dehydrogenation and clustering, eventually forming Elemental Carbon (EC) or mature soot (Michelsen, 2017). The transformation from incipient to mature soot is governed by the combustion conditions. Worth noting is the significance of EC's equivalence to black carbon (BC)—a potent light-absorbing material with a considerable contribution to climate warming (Bond et al., 2013) in the atmospheric science domain. Additionally, incipient soot, which may also bear light-absorbing qualities in the near-ultraviolet and visible wavelengths, constitutes a major portion of atmospheric brown carbon (BrC) (Saleh et al., 2018), further emphasizing the relevance of these emissions in climate discussions.

Previous studies have reported substantial decrease of mature soot production in engines (Hanson et al., 2010; Kumar & Saravanan, 2016; Lee et al., 2003; Reitz & Duraisamy, 2015; Sellnau et al., 2016; Sellnau et al., 2015; Soloiu et al., 2018) and constant-volume combustion chambers (Fattah et al., 2018; Liu et al., 2012) operated in LTC mode. However, these reports are based on optical techniques that are tailored for measuring CDC aerosol emissions, which are dominated by mature soot. The most common method is the filter smoke number (FSN) obtained from reflectance measurements of particles collected on a filter (Ciatti et al., 2013; Sellnau et al., 2016; Sellnau et al., 2015; Storey et al., 2017). Other methods include smoke and opacity meters which also operates based on light-extinction techniques (An et al., 2018; Kumar & Saravanan, 2016; Soloiu et al., 2018). All these techniques exploit the strong light-absorptive nature of mature soot and convert the observed light absorption into particle mass based on either calibration against or assumed light-absorption properties of mature soot (or BC), since they were originally developed to quantify aerosol emissions mainly from diesel combustion, which

have long been established to be mostly comprised of mature soot. Because LTC emissions are dominated by OC, which is significantly less absorptive than EC (Moses-DeBusk et al., 2019), these techniques would severely underestimate the mass loadings of incipient soot as reported in recent studies that used different measurement techniques that do not use light absorption and are therefore not specific for mature soot.

Northrop et al. (Northrop et al., 2011) showed that even though the production of EC (i.e. mature soot) was largely reduced in LTC of biodiesel, the emissions contained considerable amounts of OA that were characterized using electrical mobility measurements. Lucachick et al. (Lucachick et al., 2016) conducted measurements of particle size distributions from an engine functioning in a dual-fuel ACI mode, utilizing gasoline and diesel. Their findings revealed a predominance of volatile particles. Other studies have revealed that, even at lower FSN and particle number emissions, engines operated in ACI modes are capable of emitting a substantial mass, evident from the material collected on the sampling filter (Prikhodko et al., 2010; Storey et al., 2017). Moses-DeBusk et al. (Moses-DeBusk et al., 2019) reported that the aerosol emissions from an engine operated at HCCI conditions were dominated by OA, as obtained using an OC-EC analyzer. Consequently, the aerosol mass emission rate measured using a Micro Soot Sensor was an order of magnitude smaller than that measured using the OC-EC analyzer, emphasizing the inadequacy of instruments tailored to detect mature soot at quantifying LTC aerosol emissions.

### 1.5. Objectives and summary of chapters

This dissertation aims to illuminate the characteristics and formation of ‘first-stage’ aerosols that are associated with first-stage ignition exhibited by two-stage ignition fuels. Such insights are crucial in evaluating the potential atmospheric impacts of prospective next-generation engine technologies. The dissertation is structured around three central objectives: a) investigate the

difference in physicochemical properties between first and second-stage aerosols emitted from controlled-combustion experiments; b) scrutinize the formation trajectories of first-stage aerosols, their ubiquity in engine emissions, and their potential implications for urban atmospheres; and c) assess the effect of additives, used to enhance ignition properties in ACI, on the development and characteristics of first-stage aerosols. The dissertation is structured as follows:

In Chapter 2, combustion experiments were conducted with toluene and *n*-heptane in an atmospheric-pressure reactor, maintained at a constant equivalence ratio ($\phi$ = 2.3) and $O_2/N_2$ = 0.06. Temperatures were systematically varied from 250 °C to 1035 °C. We chose fuels based on their unique characteristics: toluene, an aromatic compound, and *n*-heptane, a linear alkane notable for its two-stage ignition behavior. We performed real-time measurements of aerosol size distributions, volatility, and light-absorption properties, along with offline molecular-size characterization. Aerosols emitted from both fuels consisted of light-absorbing organics, classified as BrC. At the peak combustion temperature of 1035 °C, aerosol emissions from toluene combustion were twenty times larger than those from *n*-heptane. Furthermore, aerosol emissions from toluene combustion contained larger molecular-size species, were less volatile, and more light absorbing than those from *n*-heptane. In terms of both fuels, a sharp decline in aerosol emission factors was noticed with decreasing temperatures. However, a resurgence of aerosol emissions was observed at lower temperatures, peaking at 290 °C for *n*-heptane combustion, which was not seen for toluene. These findings align with chemical kinetic simulations, verifying that *n*-heptane consumption during first-stage ignition align with first-stage OA emission profiles.

Chapter 3 highlighted the discovery of oxygenated primary organic aerosols (OxyPOA) in the first-stage OA and tied them to engine emissions. This investigation was conducted in collaboration with the Oak Ridge National Lab (ORNL) and the Pacific Northwest National Lab (PNNL). The study involved collecting gas and first-stage OA samples that were emitted during *n*-pentane LTC, a fuel with two-stage ignition behavior, to understand the formation pathways of first-stage OA. We also obtained filters from ORNL of aerosol samples that represent three different scenarios of emissions from engines: 1) cold starts from spark ignition engine, and an engine operated in 2) ACI mode, and 3) conventional diesel combustion (CDC) mode. The chemical speciation of all these samples revealed similarities between first-stage OA and samples from ACI and cold start, both of which contained highly oxygenated compounds we identified as OxyPOA, which retains chemical properties similar to those of secondary organic aerosols (SOA). This insight contests the prevailing belief that oxygenated OA chiefly consists of SOA, while urban POA, which originates from the combustion of hydrocarbon fuels in engines, is primarily hydrocarbon-like OA (HOA). Furthermore, these results emphasize the importance of exploring OxyPOA formation in our pursuit to comprehend OA pollution in contemporary and future urban environments.

In Chapter 4, we explored the effects of incorporating fuel additives that enhance ignition properties in ACI on first-stage OA formation. Additives are used for their ability to provide better control of combustion timing by inhibiting radicals' activity displayed by two-stage ignition fuels. We carried out controlled-combustion experiments maintained at temperatures relevant to LTC and constant equivalence ratio ($\phi = 1$) and $O_2/N_2 = 0.1$, using three binary fuel mixtures. Each mixture utilizes *n*-heptane as the primary fuel and is combined with one of three distinct additives: ethanol, toluene, and DMF, each known for their unique radical scavenging

capabilities. Our findings highlighted that additives possessing a strong inhibitory nature and demonstrating synergistic behavior towards RON were markedly more effective in curbing the formation of first-stage OA, as opposed to those exhibiting antagonistic behavior.

**References**


Agarwal, A. K., Singh, A. P., & Maurya, R. K. (2017). Evolution, challenges and path forward for low temperature combustion engines. *Progress in Energy and Combustion Science*, *61*, 1-56.

Ahire, V., Shewale, M., & Razban, A. (2021). A review of the state-of-the-art emission control strategies in modern diesel engines. *Archives of Computational Methods in Engineering*, *28*(7), 4897-4915.

Alexandrino, K. (2020). Comprehensive review of the impact of 2, 5-Dimethylfuran and 2-Methylfuran on soot emissions: Experiments in diesel engines and at laboratory-scale. *Energy & Fuels*, *34*(6), 6598-6623.

An, Y., Jaasim, M., Raman, V., Im, H. G., & Johansson, B. (2018). In-cylinder combustion and soot evolution in the transition from conventional compression ignition (CI) mode to partially premixed combustion (PPC) mode. *Energy & Fuels*, *32*(2), 2306-2320.

Anderson, J. E., Leone, T. G., Shelby, M. H., Wallington, T. J., Bizub, J. J., Foster, M., Lynskey, M. G., & Polovina, D. (2012). *Octane numbers of ethanol-gasoline blends: measurements and novel estimation method from molar composition* (0148-7191).

Badra, J., AlRamadan, A. S., & Sarathy, S. M. (2017). Optimization of the octane response of gasoline/ethanol blends. *Applied Energy*, *203*, 778-793.

Bedoya, I. D., Saxena, S., Cadavid, F. J., Dibble, R. W., & Wissink, M. (2012). Experimental study of biogas combustion in an HCCI engine for power generation with high indicated efficiency and ultra-low NOx emissions. *Energy Conversion and Management*, *53*(1), 154-162.

Berggren, C., & Magnusson, T. (2012). Reducing automotive emissions—The potentials of combustion engine technologies and the power of policy. *Energy Policy*, *41*, 636-643.

Bond, T. C., Doherty, S. J., Fahey, D. W., Forster, P. M., Berntsen, T., DeAngelo, B. J., Flanner, M. G., Ghan, S., Kärcher, B., & Koch, D. (2013). Bounding the role of black carbon in the climate system: A scientific assessment. *Journal of Geophysical Research: Atmospheres*, *118*(11), 5380-5552.

Burke, U., Somers, K. P., O'Toole, P., Zinner, C. M., Marquet, N., Bourque, G., Petersen, E. L., Metcalfe, W. K., Serinyel, Z., & Curran, H. J. (2015). An ignition delay and kinetic modeling study of methane, dimethyl ether, and their mixtures at high pressures. *Combustion and Flame*, *162*(2), 315-330.

Calderón-Garcidueñas, L., & Ayala, A. (2022). Air Pollution, Ultrafine Particles, and Your Brain: Are Combustion Nanoparticle Emissions and Engineered Nanoparticles Causing Preventable Fatal Neurodegenerative Diseases and Common Neuropsychiatric Outcomes? *Environmental science & technology*.

Chen, G., Shen, Y., Zhang, Q., Yao, M., Zheng, Z., & Liu, H. (2013). Experimental study on combustion and emission characteristics of a diesel engine fueled with 2, 5-dimethylfuran–diesel, n-butanol–diesel and gasoline–diesel blends. *Energy*, *54*, 333-342.

Chesterton, A. (2018). *How many cars are there in the world?* https://www.carsguide.com.au/car-advice/how-many-cars-are-there-in-the-world-70629

Christensen, E., Yanowitz, J., Ratcliff, M., & McCormick, R. L. (2011). Renewable oxygenate blending effects on gasoline properties. *Energy & Fuels*, *25*(10), 4723-4733.
Ciatti, S., Johnson, M., Adhikary, B. D., Reitz, R. D., & Knock, A. (2013). *Efficiency and emissions performance of multizone stratified compression ignition using different octane fuels* (0148-7191).
Curran, H. J., Pitz, W. J., Westbrook, C. K., Callahan, G., & Dryer, F. L. (1998). Oxidation of automotive primary reference fuels at elevated pressures. Symposium (International) on Combustion,
Dec, J. E. (2009). Advanced compression-ignition engines—understanding the in-cylinder processes. *Proceedings of the Combustion Institute*, *32*(2), 2727-2742.
Dec, J. E., & Hwang, W. (2009). Characterizing the development of thermal stratification in an HCCI engine using planar-imaging thermometry. *SAE International Journal of Engines*, *2*(1), 421-438.
Donaldson, K., Tran, L., Jimenez, L. A., Duffin, R., Newby, D. E., Mills, N., MacNee, W., & Stone, V. (2005). Combustion-derived nanoparticles: a review of their toxicology following inhalation exposure. *Particle and fibre toxicology*, *2*(1), 10.
Epping, K., Aceves, S., Bechtold, R., & Dec, J. E. (2002). *The potential of HCCI combustion for high efficiency and low emissions* (0148-7191).
Fattah, I. R., Ming, C., Chan, Q., Wehrfritz, A., Pham, P., Yang, W., Kook, S., Medwell, P., Yeoh, G., & Hawkes, E. (2018). Spray and combustion investigation of post injections under low-temperature combustion conditions with biodiesel. *Energy & Fuels*, *32*(8), 8727-8742.
Fioroni, G. M., Rahimi, M. J., Westbrook, C. K., Wagnon, S. W., Pitz, W. J., Kim, S., & McCormick, R. L. (2022). Chemical kinetic basis of synergistic blending for research octane number. *Fuel*, *307*, 121865.
Foong, T. M., Morganti, K. J., Brear, M. J., da Silva, G., Yang, Y., & Dryer, F. L. (2014). The octane numbers of ethanol blended with gasoline and its surrogates. *Fuel*, *115*, 727-739.
Frenklach, M., & Wang, H. (1991). Detailed modeling of soot particle nucleation and growth. Symposium (International) on Combustion,
Han, M. (2013). The effects of synthetically designed diesel fuel properties–cetane number, aromatic content, distillation temperature, on low-temperature diesel combustion. *Fuel*, *109*, 512-519.
Hanson, R. M., Kokjohn, S. L., Splitter, D. A., & Reitz, R. D. (2010). An experimental investigation of fuel reactivity controlled PCCI combustion in a heavy-duty engine. *SAE international journal of engines*, *3*(1), 700-716.
Hashimoto, K. (2007). *Effect of Ethanol on the HCCI Combustion* (0148-7191).
Herrmann, F., Jochim, B., Oßwald, P., Cai, L., Pitsch, H., & Kohse-Höinghaus, K. (2014). Experimental and numerical low-temperature oxidation study of ethanol and dimethyl ether. *Combustion and Flame*, *161*(2), 384-397.
Heywood, J. B., & Welling, O. Z. (2009). Trends in performance characteristics of modern automobile SI and diesel engines. *SAE International Journal of Engines*, *2*(1), 1650-1662.
Johansson, K., Head-Gordon, M., Schrader, P., Wilson, K., & Michelsen, H. (2018). Resonance-stabilized hydrocarbon-radical chain reactions may explain soot inception and growth. *Science*, *361*(6406), 997-1000.

Kang, D., Shah, A., Rockstroh, T., & Goldsborough, S. (2019). *Utilizing static autoignition measurements to estimate intake air condition requirements for compression ignition in a multi-mode engine-Application of Chemical Kinetic Modeling* (0148-7191).

Kumar, B. R., & Saravanan, S. (2016). Effects of iso-butanol/diesel and n-pentanol/diesel blends on performance and emissions of a DI diesel engine under premixed LTC (low temperature combustion) mode. *Fuel*, *170*, 49-59.

Lawal, A., Davids, L. M., & Marnewick, J. L. (2016). Diesel exhaust particles and endothelial cells dysfunction: An update. *Toxicology in vitro*, *32*, 92-104.

Lee, C.-f., Wu, Y., Wu, H., Shi, Z., Zhang, L., & Liu, F. (2019). The experimental investigation on the impact of toluene addition on low-temperature ignition characteristics of diesel spray. *Fuel*, *254*, 115580.

Lee, C. S., Lee, K. H., & Kim, D. S. (2003). Experimental and numerical study on the combustion characteristics of partially premixed charge compression ignition engine with dual fuel☆. *Fuel*, *82*(5), 553-560.

Liu, H., Bi, X., Huo, M., Lee, C.-f. F., & Yao, M. (2012). Soot emissions of various oxygenated biofuels in conventional diesel combustion and low-temperature combustion conditions. *Energy & Fuels*, *26*(3), 1900-1911.

Liu, H., Xu, J., Zheng, Z., Li, S., & Yao, M. (2013). Effects of fuel properties on combustion and emissions under both conventional and low temperature combustion mode fueling 2, 5-dimethylfuran/diesel blends. *Energy*, *62*, 215-223.

Lu, X., Han, D., & Huang, Z. (2011). Fuel design and management for the control of advanced compression-ignition combustion modes. *Progress in Energy and Combustion Science*, *37*(6), 741-783.

Lü, X., Hou, Y., Zu, L., & Huang, Z. (2006). Experimental study on the auto-ignition and combustion characteristics in the homogeneous charge compression ignition (HCCI) combustion operation with ethanol/n-heptane blend fuels by port injection. *Fuel*, *85*(17-18), 2622-2631.

Lucachick, G., Curran, S., Storey, J., Prikhodko, V., & Northrop, W. F. (2016). Volatility characterization of nanoparticles from single and dual-fuel low temperature combustion in compression ignition engines. *Aerosol Science and Technology*, *50*(5), 436-447.

Machrafi, H. (2008). Experimental validation of a kinetic multi-component mechanism in a wide HCCI engine operating range for mixtures of n-heptane, iso-octane and toluene: Influence of EGR parameters. *Energy Conversion and Management*, *49*(11), 2956-2965.

Maurya, R. K., Maurya, R. K., & Luby. (2018). *Characteristics and control of low temperature combustion engines*. Springer.

Mazzoli-Rocha, F., Carvalho, G. M., Lanzetti, M., Valença, S. S., Silva, L. F., Saldiva, P. H., Zin, W. A., & Faffe, D. S. (2014). Respiratory toxicity of repeated exposure to particles produced by traffic and sugar cane burning. *Respiratory physiology & neurobiology*, *191*, 106-113.

McCormick, R. L., Fioroni, G., Fouts, L., Christensen, E., Yanowitz, J., Polikarpov, E., Albrecht, K., Gaspar, D. J., Gladden, J., & George, A. (2017). Selection criteria and screening of potential biomass-derived streams as fuel blendstocks for advanced spark-ignition engines. *SAE International Journal of Fuels and Lubricants*, *10*(2), 442-460.

Michelsen, H. (2017). Probing soot formation, chemical and physical evolution, and oxidation: A review of in situ diagnostic techniques and needs. *Proceedings of the Combustion Institute*, *36*(1), 717-735.

Moses-DeBusk, M., Curran, S. J., Lewis, S. A., Connatser, R. M., & Storey, J. M. (2019). Impacts of Air-Fuel Stratification in ACI Combustion on Particulate Matter and Gaseous Emissions. *Emission Control Science and Technology*, *5*(3), 225-237.

Nalley, S., & LaRose, A. (2022). Annual energy outlook 2022 (AEO2022). *Energy Information Agency*, 23.

Northrop, W. F., Madathil, P. V., Bohac, S. V., & Assanis, D. N. (2011). Condensational growth of particulate matter from partially premixed low temperature combustion of biodiesel in a compression ignition engine. *Aerosol Science and Technology*, *45*(1), 26-36.

Ortiz-Soto, E. A., Lavoie, G. A., Wooldridge, M. S., & Assanis, D. N. (2019). Thermodynamic efficiency assessment of gasoline spark ignition and compression ignition operating strategies using a new multi-mode combustion model for engine system simulations. *International Journal of Engine Research*, *20*(3), 304-326.

Pachauri, R. K., Allen, M. R., Barros, V. R., Broome, J., Cramer, W., Christ, R., Church, J. A., Clarke, L., Dahe, Q., & Dasgupta, P. (2014). *Climate change 2014: synthesis report. Contribution of Working Groups I, II and III to the fifth assessment report of the Intergovernmental Panel on Climate Change*. Ipcc.

Peng, Z., Zhao, H., Ma, T., & Ladommatos, N. (2005). Characteristics of homogeneous charge compression ignition (HCCI) combustion and emissions of n-heptane. *Combustion science and technology*, *177*(11), 2113-2150.

Prikhodko, V. Y., Curran, S. J., Barone, T. L., Lewis, S. A., Storey, J. M., Cho, K., Wagner, R. M., & Parks, J. E. (2010). Emission characteristics of a diesel engine operating with in-cylinder gasoline and diesel fuel blending. *SAE International Journal of Fuels and Lubricants*, *3*(2), 946-955.

Ranzi, E., Gaffuri, P., Faravelli, T., & Dagaut, P. (1995). A wide-range modeling study of n-heptane oxidation. *Combustion and Flame*, *103*(1-2), 91-106.

Reitz, R. D., & Duraisamy, G. (2015). Review of high efficiency and clean reactivity controlled compression ignition (RCCI) combustion in internal combustion engines. *Progress in Energy and Combustion Science*, *46*, 12-71.

[Record #169 is using a reference type undefined in this output style.]

Ribaucour, M., Minetti, R., Sochet, L., Curran, H., Pitz, W., & Westbrook, C. (2000). Ignition of isomers of pentane: an experimental and kinetic modeling study. *Proceedings of the Combustion Institute*, *28*(2), 1671-1678.

Rodriguez, A., Frottier, O., Herbinet, O., Fournet, R., Bounaceur, R., Fittschen, C., & Battin-Leclerc, F. (2015). Experimental and modeling investigation of the low-temperature oxidation of dimethyl ether. *The Journal of Physical Chemistry A*, *119*(28), 7905-7923.

Saisirirat, P., Foucher, F., Chanchaona, S., & Mounaïm-Rousselle, C. (2010). Spectroscopic measurements of low-temperature heat release for homogeneous combustion compression ignition (HCCI) n-heptane/alcohol mixture combustion. *Energy & Fuels*, *24*(10), 5404-5409.

Saisirirat, P., Togbé, C., Chanchaona, S., Foucher, F., Mounaïm-Rousselle, C., & Dagaut, P. (2011). Auto-ignition and combustion characteristics in HCCI and JSR using 1-butanol/n-heptane and ethanol/n-heptane blends. *Proceedings of the Combustion Institute*, *33*(2), 3007-3014.

Saleh, R., Cheng, Z., & Atwi, K. (2018). The brown–black continuum of light-absorbing combustion aerosols. *Environmental Science & Technology Letters*, *5*(8), 508-513.

Saxena, S., & Bedoya, I. D. (2013). Fundamental phenomena affecting low temperature combustion and HCCI engines, high load limits and strategies for extending these limits. *Progress in Energy and Combustion Science*, *39*(5), 457-488.

Sellnau, M., Foster, M., Moore, W., Sinnamon, J., Hoyer, K., & Klemm, W. (2016). Second generation GDCI multi-cylinder engine for high fuel efficiency and US tier 3 emissions. *SAE International Journal of Engines*, *9*(2), 1002-1020.

Sellnau, M., Moore, W., Sinnamon, J., Hoyer, K., Foster, M., & Husted, H. (2015). GDCI multi-cylinder engine for high fuel efficiency and low emissions. *Sae international journal of engines*, *8*(2), 775-790.

Shibata, G., Oyama, K., Urushihara, T., & Nakano, T. (2005). *Correlation of low temperature heat release with fuel composition and HCCI engine combustion* (0148-7191).

Shibata, G., & Urushihara, T. (2007). Auto-ignition characteristics of hydrocarbons and development of HCCI fuel index. *SAE Transactions*, 304-323.

Silke, E. J., Pitz, W. J., Westbrook, C. K., Sjöberg, M., & Dec, J. E. (2009). Understanding the chemical effects of increased boost pressure under HCCI conditions. *SAE International Journal of Fuels and Lubricants*, *1*(1), 12-25.

Singh, E., Shankar, V. S. B., Tripathi, R., Pitsch, H., & Sarathy, S. M. (2018). 2-Methylfuran: A bio-derived octane booster for spark-ignition engines. *Fuel*, *225*, 349-357.

Soloiu, V., Moncada, J. D., Gaubert, R., Muiños, M., Harp, S., Ilie, M., Zdanowicz, A., & Molina, G. (2018). LTC (low-temperature combustion) analysis of PCCI (premixed charge compression ignition) with n-butanol and cotton seed biodiesel versus combustion and emissions characteristics of their binary mixtures. *Renewable Energy*, *123*, 323-333.

Splitter, D., Hanson, R., Kokjohn, S., & Reitz, R. D. (2011). *Reactivity controlled compression ignition (RCCI) heavy-duty engine operation at mid-and high-loads with conventional and alternative fuels* (0148-7191).

Stanglmaier, R. H., & Roberts, C. E. (1999). Homogeneous charge compression ignition (HCCI): benefits, compromises, and future engine applications. *SAE Transactions*, 2138-2145.

Storey, J. M., Curran, S. J., Lewis, S. A., Barone, T. L., Dempsey, A. B., Moses-DeBusk, M., Hanson, R. M., Prikhodko, V. Y., & Northrop, W. F. (2017). Evolution and current understanding of physicochemical characterization of particulate matter from reactivity controlled compression ignition combustion on a multicylinder light-duty engine. *International Journal of Engine Research*, *18*(5-6), 505-519.

Tanaka, S., Ayala, F., Keck, J. C., & Heywood, J. B. (2003). Two-stage ignition in HCCI combustion and HCCI control by fuels and additives. *Combustion and Flame*, *132*(1-2), 219-239.

Thring, R. H. (1989). *Homogeneous-charge compression-ignition (HCCI) engines* (0148-7191).

Wang, H. (2011). Formation of nascent soot and other condensed-phase materials in flames. *Proceedings of the Combustion Institute*, *33*(1), 41-67.

Waqas, M. U., Masurier, J.-B., Sarathy, M., & Johansson, B. (2018). *Blending octane number of toluene with gasoline-like and PRF fuels in HCCI combustion mode* (0148-7191).

Westbrook, C. K. (2000). Chemical kinetics of hydrocarbon ignition in practical combustion systems. *Proceedings of the Combustion Institute*, *28*(2), 1563-1577.

Yao, M., Zheng, Z., & Liu, H. (2009). Progress and recent trends in homogeneous charge compression ignition (HCCI) engines. *Progress in Energy and Combustion Science*, *35*(5), 398-437.

Yuan, H., Yang, Y., Brear, M. J., Foong, T. M., & Anderson, J. E. (2017). Optimal octane number correlations for mixtures of toluene reference fuels (TRFs) and ethanol. *Fuel*, *188*, 408-417.

Zhao, F., Asmus, T. N., Assanis, D. N., Dec, J. E., Eng, J. A., & Najt, P. M. (2003). *Homogeneous charge compression ignition (HCCI) engines*.

# CHAPTER 2

# TWO-STAGE AEROSOL FORMATION IN LOW-TEMPERATURE COMBUSTION [1]

[1] El Hajj, O., Atwi, K., Cheng, Z, Koritzke, A., Christianson, M., Dewey, N., Rotavera, B., Saleh, R. (2021). Two-stage aerosol formation in low-temperature combustion. Fuel, 304, 121322.
Reprinted here with permission of the publisher

**Abstract**

Advanced low-temperature combustion (LTC) has emerged as a promising strategy for reducing pollutant formation in internal combustion engines. However, there is a lack of understanding of how the chemistry governing the differences in ignition behavior between low-temperature and conventional combustion affects emission rates and physicochemical properties of particulate matter (aerosols). To provide insight on this question, we conducted combustion experiments using toluene and *n*-heptane in an atmospheric-pressure reactor controlled at constant equivalence ratio ($\phi$ = 2.3) and $O_2/N_2$ = 0.06, and at temperatures varied in a stepwise fashion between 250 °C and 1035 °C. The selection of these two fuels was based on the following: toluene is an aromatic compound with high sooting propensity while *n*-heptane, a linear alkane, has a comparatively lower sooting propensity but exhibits clear two-stage ignition that involves negative temperature coefficient (NTC) behavior governed by a sequence of peroxy-radical-mediated chemistry that is not present in toluene combustion. We performed real-time measurements of aerosol size distributions, volatility, and light-absorption properties. We also performed offline molecular-size characterization. Aerosols emitted from both fuels were comprised of light-absorbing organics that are categorized as brown carbon. At the highest combustion temperature (1035 °C), the aerosol emissions from toluene combustion were a factor of 20 larger than *n*-heptane. The aerosol emissions from toluene combustion had more abundance of large molecular-size species, were less volatile, and were more light-absorbing than *n*-heptane. For both fuels, aerosol emission factors exhibited a steep drop with decreasing temperatures. However, there was a resurgence in aerosol emissions at lower temperatures with a peak at 290 °C for *n*-heptane combustion that was not observed for toluene. This is consistent

with chemical kinetics simulations conducted at the experimental conditions, where fuel consumption rates show prominent NTC behavior for *n*-heptane, but not for toluene.

## 2.1. Introduction

Advanced compression-ignition (ACI) is a next-generation strategy in internal combustion engines that aims to achieve high efficiency while maintaining low levels of pollution emissions (Dec, 2009; Dec & Hwang, 2009; Moses-DeBusk et al., 2019). Several ACI technologies have been proposed, including homogeneous charge compression-ignition (HCCI), premixed charge compression ignition (PCCI) (Epping et al., 2002; Stanglmaier & Roberts, 1999; Thring, 1989; Zhao et al., 2003), and reactivity controlled compression-ignition (RCCI) (Reitz & Duraisamy, 2015; Splitter et al., 2011), as well as hybrid concepts that combine different ACI strategies (Kang et al., 2019; Ortiz-Soto et al., 2019). All these approaches rely on low-temperature combustion (LTC) to reduce pollutant emissions by avoiding the NOx-soot tradeoff that occurs at the combustion conditions typical for conventional diesel combustion (CDC) (Agarwal et al., 2017; Han, 2013). The widely accepted model (Kitamura et al., 2003) is that NOx forms at high temperatures ($T > 1900$ °C) and fuel-lean conditions (equivalence ratio, $\phi < 1$) while soot forms at relatively lower temperatures ($T \approx 1100$ °C – 1700 °C) and fuel-rich conditions ($\phi > 2$). CDC systems involve inhomogeneous combustion conditions with respect to fuel/air mixing and temperature. As a result, conditions in those systems span both the soot- and NOx-formation regions. Any alterations to engine operation within the CDC environment would push the conditions further into one of these two regions, hence the NOx-soot tradeoff (Dec, 2009). On the other hand, the premixing and ignition delay employed in LTC engines allow for a more homogeneous fuel-lean combustion at temperatures substantially lower than CDC, thus avoiding both soot and NOx formation regions. Given the strong dependence of NOx formation on combustion temperature, its near-elimination in LTC is certain. However, the elimination of soot formation in LTC is not as straightforward.

The terminology concerning aerosols, or particulate matter, in combustion emissions can be confusing. Therefore, it is important to explain the terminology that we adopt in this paper. In combustion engines literature, and to a certain extent in atmospheric science literature, the term "soot" is used to represent aerosol combustion emissions that are comprised of solid aggregates of elemental carbon (EC). EC is also often used synonymously with black carbon (BC) in the atmospheric science literature due to its black appearance (strong light absorption in the visible spectrum) (Bond & Bergstrom, 2006). However, depending on the combustion conditions, a significant fraction of aerosol combustion emissions can be organic and is referred to as organic aerosol (OA) or organic carbon (OC) (i.e. when only accounting for the carbon content of the organic molecules). In fact, OA can form through the same soot-formation route as EC, which involves growth and aggregation of polycyclic aromatic hydrocarbons (PAHs) (Michelsen, 2017; Wang, 2011) but under conditions that are not conducive for the completion of the soot-formation process. To emphasize this connection, Michelsen (Michelsen, 2017) refers to this OA as "incipient soot" and the solid aggregates, mostly EC aerosols as "mature soot." In this paper, we adopt the Michelsen terminology, and hereafter, we add (mature) before "soot" when referencing previous studies to emphasize that what those studies refer to as "soot" is indeed "mature soot." We have shown that incipient soot comprises a major fraction of atmospheric brown carbon (BrC) (Saleh et al., 2018). BrC, or light-absorbing OA, is less absorptive than BC in the visible spectrum and exhibits absorption more skewed toward the short wavelengths, which gives it its brown color (Andreae & Gelencsér, 2006; Laskin et al., 2015). BC, mostly comprised of elemental carbon, has relatively constrained light-absorption properties while BrC is comprised of a multitude of organic species with light-absorption efficiencies that vary over several orders of magnitude (Bond et al., 2013; Saleh, 2020). BrC plays an important role

alongside BC in absorbing solar radiation and climate forcing (Bond et al., 2013; Saleh, 2020). For completeness, we note that OA in combustion-engine emissions also includes organic species other than incipient soot (e.g. from lubricating oil (Worton et al., 2014)), and altogether, OA emissions from combustion are referred to as primary organic aerosol (POA). For readers not familiar with aerosol terminology, we summarize the key definitions discussed in this paragraph in Table 2.1.

**Table 2.1.** Summary of definitions of key terms related to combustion aerosols

| Term | Definition |
|---|---|
| Mature soot (Michelsen, 2017) | - Solid aggregates of mostly elemental carbon emitted from incomplete combustion.<br>- Often referred to as just "soot" in both combustion and atmospheric science literature. |
| Incipient soot (Michelsen, 2017) | - Organic aerosol emitted from incomplete combustion that form through the same soot-formation route as mature soot but under conditions (e.g. low temperature) not conducive for the completion of the soot-formation process.<br>- Is categorized as POA.<br>- Can be light-absorbing and thus categorized as brown carbon (BrC) |
| Black carbon (BC) (Bond & Bergstrom, 2006) | - Comprised mostly of elemental carbon, it is defined operationally based on its black appearance (strong light absorption in the visible spectrum).<br>- Its definition largely overlaps with that of mature soot. |
| Brown carbon (BrC) (Andreae & Gelencsér, 2006) | - Light-absorbing organic aerosol (OA).<br>- Defined operationally based on its light-absorption properties that exhibit strong wavelength dependence in the visible spectrum (increased absorption toward short wavelengths), thus giving it a brown appearance. |

Previous studies have reported substantial decrease of (mature) soot production in engines (Hanson et al., 2010; Kumar & Saravanan, 2016; Lee et al., 2003; Reitz & Duraisamy, 2015; Sellnau et al., 2016; Sellnau et al., 2015; Soloiu et al., 2018) and constant-volume combustion chambers (Fattah et al., 2018; Liu et al., 2012) operated in LTC mode versus CDC mode. However, these reports are based on optical techniques that are tailored for measuring CDC

aerosol emissions, which are dominated by mature soot. The most common method is the filter smoke number (FSN) obtained from reflectance measurements of particles collected on a filter (Ciatti et al., 2013; Sellnau et al., 2016; Sellnau et al., 2015; Storey et al., 2017). Other techniques include the commercially available Opacimeter (Kumar & Saravanan, 2016) and Micro Soot Sensor (An et al., 2018; Soloiu et al., 2018), as well as other light-extinction techniques (e.g. forward illumination light extinction) (Liu et al., 2012). All these techniques exploit the strong light-absorptive nature of mature soot and convert the observed light absorption into particle mass based on either calibration against or assumed light-absorption properties of mature soot (or BC). Because LTC emissions are dominated by OC , which is significantly less absorptive than EC (Moses-DeBusk et al., 2019), these techniques would severely underestimate the mass loadings of aerosols emitted under LTC conditions (Storey et al., 2017).

Realizing that the aerosol emissions in LTC are dominated by OA, several studies have applied aerosol characterization techniques that do not rely on light absorption and are therefore not specific for mature soot. Northrop et al. (Northrop et al., 2011) showed that even though the production of EC (i.e. mature soot) was largely reduced in LTC of biodiesel, the emissions contained considerable amounts of OA that were characterized using electrical mobility measurements. Lucachick et al. (Lucachick et al., 2016) reported that the aerosol emissions in LTC (PCCI and RCCI) contained substantially less (mature) soot than CDC and were dominated by semi-volatile OA, as shown by volatility tandem differential mobility analysis. Storey et al. (Storey et al., 2017) reported that while the FSN method predicted negligible aerosol emissions from an engine operated in RCCI mode compared to CDC mode, gravimetric analysis showed that the mass loadings of aerosol emissions from the two modes were of the same order of

magnitude. Moses-DeBusk et al. (Moses-DeBusk et al., 2019) reported that the aerosol emissions from an engine operated at HCCI conditions were dominated by OA, as obtained using an OC-EC analyzer. Consequently, the aerosol mass emission rate measured using a Micro Soot Sensor was an order of magnitude smaller than that measured using the OC-EC analyzer, emphasizing the inadequacy of instruments tailored to detect mature soot at quantifying LTC aerosol emissions.

The studies summarized above demonstrate that LTC suppresses (mature) soot production but it can potentially lead to significant OA production. However, while the framework for the chemistry governing autoignition at LTC conditions is well understood as a degenerate chain-branching mechanism (Zádor et al., 2011), the dependence of aerosol emission rates and their physicochemical properties on combustion temperature within LTC conditions is not. In this study, we performed controlled-combustion experiments at temperatures relevant for LTC conditions (≤ 1035 °C) and quantified the aerosol emissions and characterized their molecular sizes, volatility, and light-absorption properties. The experiments involved two structurally different fuels (toluene and *n*-heptane) in order to investigate the effect of differences in fuel reactivity on the emitted aerosols.

## 2.2. Materials and methods

### 2.2.1. Approach

The suppression of mature soot (EC) and elevated levels OA in LTC compared to CDC can be understood within the context of the soot-formation process in combustion. The initial steps of the process involve the formation of small aromatic species, which then aggregate to form polycyclic aromatic hydrocarbons (PAHs) (Wang, 2011). Aided by radical chain reactions, PAHs and other available hydrocarbons cluster to form condensable organic particles (Johansson

et al., 2018), or incipient soot (Michelsen, 2017). These organic particles then undergo progressive dehydrogenation and aggregation to eventually form the EC aggregates that comprise mature soot (Michelsen, 2017). While the combustion conditions in CDC promote the generation of mature soot, it is plausible that the low temperatures in LTC are not conducive for the completion of the soot-formation process (i.e. complete soot maturation), thus leading to the production of organic incipient soot. We have previously shown that incipient soot (or BrC) exhibits wide variability in physicochemical properties (molecular sizes, volatility, and light-absorption properties) (Cheng, Atwi, Hajj, et al., 2020; Cheng et al., 2019; Cheng, Atwi, Yu, et al., 2020; Saleh et al., 2018) depending on combustion conditions. Here, we isolate the effect of temperature.

We performed controlled-combustion experiments at constant pressure (1 atm), equivalence ratio ($\phi$ = 2.3), and oxygen-to-nitrogen ratio ($O_2/N_2$ = 0.06), and varied the temperature between 250 °C and 1035 °C. This temperature range covers the lower end of in-cylinder temperatures encountered in LTC conditions, which are typically between 700 °C and 1700 °C (Dec, 2009). It also encompasses exhaust temperatures, which range from 120 °C to 400 °C (Shahbakhti et al., 2010; Williams et al., 2009), where unburned fuel can continue to react. These low temperatures are also representative of "cold start" conditions in conventional engines, during which the majority of aerosol emissions take place over a typical driving cycle (Gordon et al., 2014). We investigated the effect of molecular structure by performing the experiments with two structurally different fuels that have been previously utilized in LTC studies: *n*-heptane (Ju et al., 2011; Machrafi, 2008) and toluene (Christensen & Johansson, 1998; Contino et al., 2011; Hellier et al., 2013; Ju et al., 2011; Lu et al., 2011; Ryan & Matheaus, 2003; Zhong et al., 2005).

In each experiment, we performed online measurements to characterize the emission factors, size distributions, volatility, and light-absorption properties of the emitted aerosols. We also collected filters for offline chemical characterization using laser desorption ionization mass spectrometry (LDI-MS). The experimental setup is shown in Figure 1 and the associated measurements are described in detail in the subsequent subsections. To complement the experiments, species profiles of *n*-heptane, toluene, and several intermediates were simulated using the chemical kinetics mechanism of Mehl et al. (Mehl et al., 2011).

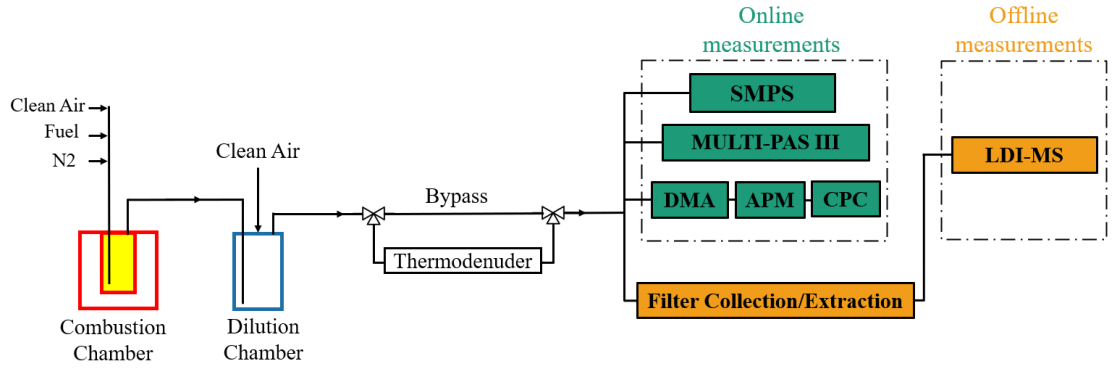


Figure 2.1. Schematic of the experimental setup

### 2.2.2. Combustion system

The combustion experiments were performed using a custom-built controlled-combustion system (Atwi et al.; Cheng, Atwi, Hajj, et al., 2020; Cheng et al., 2019; Saleh et al., 2018). It consists of a custom-made cylindrical quartz chamber (~0.24 L) enclosed in a heater (Thermcraft). The combustion reaction is temperature-initiated. A PID controller (OMEGA, CNi3244) controls the wattage of the heater to achieve a set combustion temperature measured at the center of the combustion chamber using a high-temperature K-type thermocouple. In this study, we controlled the temperature in the combustion chamber to set values between 250 °C and 1035 °C. Fuel is introduced into the combustion chamber in vapor form by flowing a stream of clean dried air,

controlled using a mass flow controller (DAKOTA, 6AGC1AL55-09AB), into a bubbler containing the fuel. We have previously performed mass transfer calculations and confirmed that the residence time of a bubble rising in the bubbler is greater than the time required to saturate it with fuel (Cheng et al., 2019). Therefore, the flowrate of the fuel exiting the bubbler can be calculated from knowledge of the fuel saturation pressure and the air flowrate. We controlled the equivalence ratio ($\phi$ = 2.3) and $O_2/N_2$ = 0.06 by mixing the fuel-saturated air stream with a controlled stream of clean air and a controlled stream of $N_2$. The values of the flowrates are given in Table S1 in Appendix A.

**2.2.3. Online measurements**

We measured the electrical-mobility size distributions of the emitted aerosols at each combustion temperature using a scanning mobility particle sizer (SMPS, TSI 3882) in the range of 10-500 nm. The SMPS uses an electrostatic classifier (TSI, Model 3082), a long differential mobility analyzer (DMA, TSI, Model 3081A00), and an advanced aerosol neutralizer (TSI, Model 3088) along with a condensation particle counter (CPC, TSI, Model 3772). We also integrated the SMPS size distributions in conjunction with particle effective densities to obtain total aerosol mass concentrations ($C_{\text{aerosol}}$). The particle effective densities were obtained using the tandem differential mobility analyzer – aerosol particle sizer (tandem DMA-APM) technique (McMurry et al., 2002). Particles were classified based on their electrical-mobility diameter ($d_{\text{m}}$) using the DMA (TSI, Model 3081A00) and their mass ($m_{\text{p}}$) was measured using the APM (Kanomax, Model 3601). The effective density was then calculated as:

$$\rho_{\text{eff}} = {m_{\text{p}}}/{v_{\text{p}}} \; ; \; v_p = {\pi \, d_{\text{m}}^3}/{6} \qquad (1)$$

We obtained $\rho_{\text{eff}}$ = 1.3 ±0.1 g/cm$^3$ for emissions from both fuels, which is consistent with values typically reported for OA (Cheng et al., 2019; Cross et al., 2007; Schmid et al., 2009).

We calculated the aerosol emission factors per unit mass fuel as:

$$\mathrm{EF} = {C_{\mathrm{aerosol}}}/{C_{\mathrm{fuel}}} \quad (2)$$

Where $C_{\mathrm{fuel}}$ is the mass concentration of the fuel entering the combustion chamber, calculated as:

$$C_{\mathrm{fuel}} = M_{\mathrm{fuel}} * {Q_{\mathrm{fuel}}}/{Q_{\mathrm{total}}} \quad (3)$$

Where $Q_{\mathrm{fuel}}$ is the fuel flowrate into the combustion chamber, $Q_{\mathrm{total}}$ is the total flowrate (fuel + air + $N_2$) (Figure 1), and $M_{\mathrm{fuel}}$ is the molar mass of the fuel.

We measured the absorption coefficients ($b_{\mathrm{abs}}$, $\mathrm{Mm}^{-1}$) at three wavelengths ($\lambda$ = 422, 532, and 782 nm) using a photoacoustic spectrophotometer (MULTI-PAS III) (Fischer & Smith, 2018). For aerosols, $b_{\mathrm{abs}}$ is an extensive property that represents the total light absorption cross-section of the particles per unit volume of air, and should not be confused with the absorption coefficient used in UV-vis spectroscopy, which has the same inverse length dimensions but represents absorbance per unit path length and is an intensive property. Normalizing $b_{\mathrm{abs}}$ by the total mass concentration of the particles ($C_{\mathrm{aerosol}}$) yields the mass absorption cross-section (MAC, $\mathrm{m}^2/\mathrm{g}$):

$$\mathrm{MAC}(\lambda) = \frac{b_{\mathrm{abs}}(\lambda)}{C_{\mathrm{aerosol}}} \quad (4)$$

MAC exhibits an inverse power-law dependence on $\lambda$ with the exponent of the power-law known as the absorption Ångström exponent (AAE). MAC and AAE, are not true intensive properties as they depend on particle size and morphology, but they can be conveniently calculated from light-absorption and particle concentration measurements and are thus often used as effective light-absorption properties.

We also retrieved the fundamental light-absorption property of the aerosols, namely the imaginary part of the refractive index ($k$) using optical closure (Atwi et al., 2021; Cheng, Atwi, Hajj, et al., 2020; Saleh et al., 2018). We performed optical calculations based on Mie theory

(Bohren & Huffman, 2008) with the aerosol size distributions obtained from SMPS measurements as model inputs and $k(\lambda)$ as a free parameter. We retrieved $k$ values from matching the calculated absorption coefficients ($b_{abs,Mie}(\lambda)$) to $b_{abs}(\lambda)$ measured using the MULTI-PAS III. Similar to MAC, $k$ also exhibits an inverse power-law dependence on $\lambda$ with an exponent $w$ (Saleh, 2020). In the small particle limit ($d << \lambda$), AAE $\approx w + 1$ (Saleh, 2020).

For select combustion-chamber temperatures, we sampled the emitted aerosols through a thermodenuder to characterize their volatility. The thermodenuder is a stainless-steel tube (L = 100 cm, ID = 2.5 cm) wrapped with heating wire that is controlled using a PID controller (OMEGA, CNi3244) to maintain a set temperature measured at the centerline of the flow using a K-type thermocouple. In this study, we applied 3 thermodenuder temperatures (50 °C, 100 °C, and 150 °C) and obtained the aerosol mass fraction remaining (MFR) at each temperature as:

$$\mathrm{MFR} = C_{\mathrm{aerosol,TD}}/C_{\mathrm{aerosol,bypass}} \quad (5)$$

Where $C_{aerosol,bypass}$ is the original aerosol mass concentration and $C_{aerosol,TD}$ is the mass concentration after heating in the TD (see Figure 2.1). Plots of MFR versus TD temperature, or thermograms, can be used to compare the volatility of different aerosol samples, where a steeper thermogram indicates higher volatility. We note that MFR is not a fundamental property as it depends on the initial aerosol mass concentration (i.e. $C_{aerosol,bypass}$) (Saleh et al., 2011). Therefore, using thermograms to compare the volatility of different aerosol population requires that $C_{aerosol,bypass}$ is the same. In this study, we ensured that $C_{aerosol,bypass}$ was consistent (350 $\mu g/m^3$) across different experiments by applying controlled dilution to the emissions downstream of the combustion chamber (Figure 2.1).

### 2.2.4. Offline chemical analysis

For select combustion-chamber temperatures, we collected aerosol samples for offline analysis using laser desorption ionization mass spectrometry (LDI-MS). Aerosol samples were collected on 47 mm Teflon filters (0.2 μm pore size, Whatman) at a flowrate of 10 LPM. The targeted mass loading on the filters was typically 300 μg in order to avoid filter clogging which occurs at ~350 μg. The filters were then immersed in 10 ml dichloromethane (DCM) and sonicated for 40 minutes to extract the aerosol samples. We spotted 10 μl of the extracted solution on an LDI-MS plate and let the DCM evaporate leaving the sample for analysis using a Bruker Autoflex TOF mass spectrometer operated in reflectron mode. The instrument uses a 337 nm Nitrogen laser in positive mode. The ion source was set to 19 kV and the reflector voltage to 20 kV. The spectrum for each sample was obtained as an average from 200 laser shots.

The advantage of LDI-MS is that it is soft-ionizing and thus allows for the detection of the large molecules, including polycyclic aromatic hydrocarbons (PAHS) and their derivatives, that make up the organic incipient soot particles (Apicella et al., 2007; Atwi et al., 2021; Faccinetto et al., 2011; Faccinetto et al., 2015; Saleh et al., 2018). We note that LDI-MS measurements are semi-quantitative due to differences in desorption and ionization efficiencies between different molecules that largely depend on the operating conditions (Apicella et al., 2010). However, one can make qualitative comparisons between mass spectra of samples obtained under the same LDI-MS operating conditions.

## 2.3. Results

### 2.3.1. Emission factors and size distributions

Figure 2.2a depicts emission factors (EFs) of the aerosol emitted from the combustion of toluene and *n*-heptane as a function of combustion-chamber temperature. At the highest temperature

(1035 °C), the EFs of toluene were approximately 800 mg/kg-fuel, a factor of 20 larger than that of *n*-heptane (approximately 40 mg/kg-fuel), demonstrating a strong dependence of aerosol formation on fuel molecular structure. These findings indicate that, as expected, above 800 °C toluene has a larger propensity for forming large organic molecules (including PAHs and their derivatives) that have low enough volatilities to condense and form incipient soot particles, as further discussed in Section 3.3.

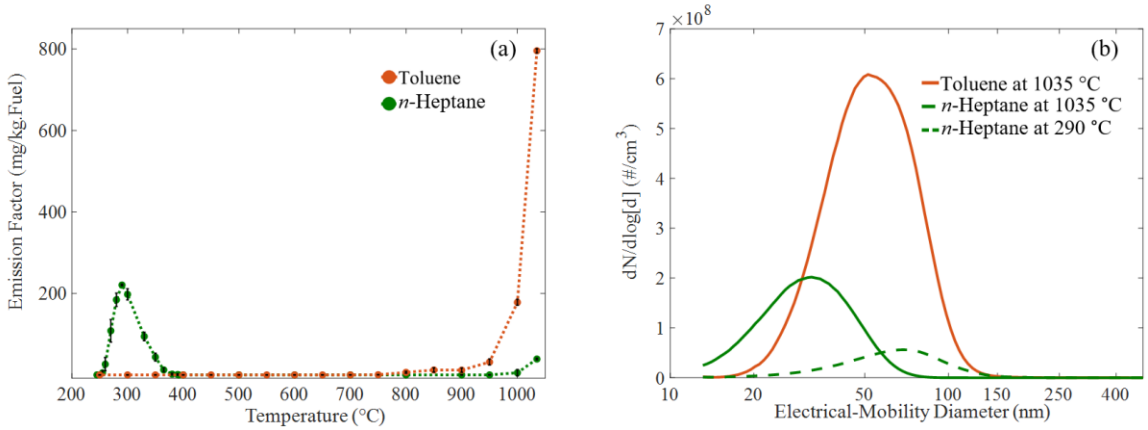


**Figure 2.2.** (a) Emission Factors of aerosols from toluene and n-heptane combustion as a function of combustion-chamber temperature. The error bars represent standard deviation from three experiments. (b) Number distributions of aerosols from the combustion of toluene at 1035 °C, *n*-heptane at 1035 °C, and *n*-heptane at 290 °C, the peak temperature in the NTC region where aerosols were observed.

For both fuels, EFs exhibited a strong temperature dependence. Toluene EFs dropped by a factor of 25 as the combustion-chamber temperature decreased from 1035 °C to 950 °C, and the aerosol emissions completely disappeared at temperatures below 750 °C. Similarly, aerosol emissions from *n*-heptane combustion disappeared at temperatures below 950 °C. However, at low temperatures (< 350 °C), *n*-heptane combustion exhibited a sharp resurgence in aerosol emissions that was not observed with toluene, with EF peak of approximately 200 mg/kg-fuel at 290 °C. This rather striking two-stage aerosol formation directly reflects low-temperature ignition behavior, which is a trait of *n*-alkanes and is driven by the formation and reaction of

peroxy radicals (ROO) that lead to several classes of intermediates, including cyclic ether isomers and alkene isomers, as further discussed in Section 3.2. Such reactions are not relevant in the oxidation of toluene largely due to the inability to form ROO because of the stability of the aromatic structure that creates high C–H bond energy (~112 kcal/mol) on phenylic sites, which resist H-abstraction at lower temperatures.

The strong dependence of aerosol EFs on fuel molecular structure and combustion temperature highlights the potential importance of combustion conditions and types of fuel blends in dictating aerosol formation in engines. The results in Figure 2.2a suggest that relatively small differences in in-cylinder temperature profiles can lead to large differences in aerosol emissions. Furthermore, our results suggest that different fuel blends might have significantly different aerosol EF profiles.

Figure 2.2b shows number size distributions of the aerosol particles emitted from toluene combustion at combustion-chamber temperature of 1035 °C and from *n*-heptane combustion at combustion-chamber temperatures of 1035 °C and 290 °C. We note the emissions were diluted by clean air prior to measurement (Figure 2.1). Therefore, the size distributions in Figure 2.2b were obtained by scaling the SMPS measurements by the dilution factor in each experiment (66 for toluene and 16 for *n*-heptane). The aerosol particles in all experiments were mostly ultrafine (< 100 nm), which is consistent with aerosol size distributions measured in LTC engine emissions (Lucachick et al., 2016; Moses-DeBusk et al., 2019) and indicates that the particles are dominated by OA (incipient soot) with negligible contribution from BC (mature soot) (Saleh et al., 2018).

### 2.3.2. Chemical kinetics modeling of species profiles

Species profiles of *n*-heptane and toluene were simulated at the conditions of the experiments using the perfectly stirred reactor module in the ChemKin-Pro 19.2 program with the reaction mechanism of Mehl et al. (Mehl et al., 2011). Table 2 shows the initial conditions used in the simulations. It is important to note that this mechanism was developed to predict ignition delay times, not soot formation, the chemical mechanisms for which differ substantially. Additional work is required to produce mechanisms capable of describing ignition chemistry simultaneously with soot formation (Akridis & Rigopoulos, 2017; Appel et al., 2000; Josephson et al., 2018; Mueller et al., 2009; Yen et al., 2018). As shown in Figure 2.3a, the depletion profile for *n*-heptane exhibits clear NTC behavior starting near ~325 °C, which is due to a shift in the balance of reactions derived from ROO from chain-branching to chain-propagating and chain-inhibiting. The simulations also show the depletion of *n*-heptane beginning at the lower end of the temperature range. In contrast, toluene mole fractions remain unchanged until ~600 °C, above which significant depletion is evident in the mole fraction predictions over a relatively narrow temperature range. Moreover, no NTC behavior is observed, which is consistent with the diminished importance of ROO chemistry in toluene combustion.

**Table 2.2.** Initial mole fractions for reactants of each species and reactor conditions used in chemical kinetics simulations.

| | toluene combustion | *n*-heptane combustion |
|---|---|---|
| Mole Fraction (fuel) | 0.014 | 0.012 |
| Mole Fraction ($O_2$) | 0.056 | 0.053 |
| Mole Fraction ($N_2$) | 0.930 | 0.935 |
| Residence Time (min.) | 0.310 | 0.300 |
| Temperature (°C) | 200 – 1100 | |

Intermediates produced from peroxy radicals are major species in the NTC region. To examine the temperature dependence of partially oxidized species, mole fractions were also simulated for

two classes of intermediates: cyclic ethers and isomers of heptene. The latter class includes 1-heptene, 2-heptene, 3-heptene, and 4-heptene, while the former comprises a total of ten cyclic ether isomers, including 2-methyl-5-ethyl tetrahydrofuran and 2-pentyloxirane.

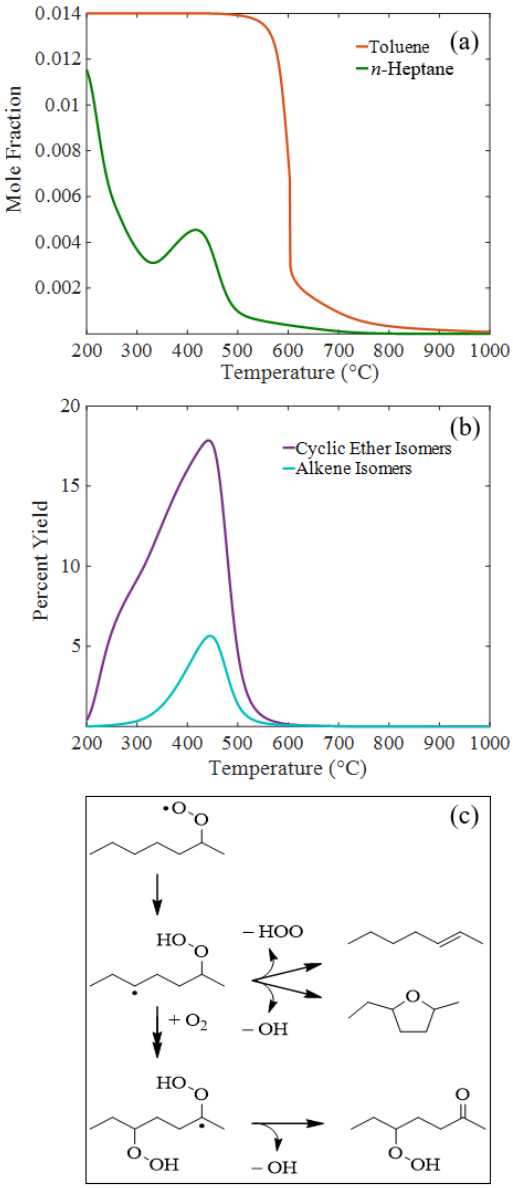


**Figure 2.3.** (a) ChemKin simulations of mole fractions of toluene and *n*-heptane conducted at 1 atm as a function of temperature. (b) Percent yields of cyclic ethers and conjugate alkenes derived from reactions of *n*-heptane-derived ROO radicals. (c) Reaction scheme of 2-heptylperoxy forming 2-heptene and 2-methyl-5-ethyltetrahydrofuran via QOOH decomposition and hept-2-one-5-hydroperoxy via second-$O_2$-addition. Combined, the yield through cyclic ether and alkene channels accounts for significant consumption of *n*-heptane in the region where organic aerosol is observed (cf. Figure 2.2a).

Based on the mole fraction results, percent yield calculations were conducted (Figure 2.3b) to quantify the extent to which the formation of the ROO-derived intermediates overlap with the temperature region where aerosol formation is observed (cf. Figure 2.2a). In the present context, the percent yield is a measure of the total amount of intermediates produced from ROO-mediated pathways, such as in Figure 2.3c, relative to the initial concentration of *n*-heptane (12000 ppm). As noted previously, the chemical kinetics mechanism used for the simulations excludes soot formation chemistry, which is a likely reason for the temperature dependence of the simulations differing from the experiments. However, as evident in Figure 2.3b, the two classes of intermediates are formed in abundance in the region where aerosols are produced in the experiments, which could explain the difference between the emissions trends in *n*-heptane versus toluene. More specifically, considering that ROO chemistry occurs in the combustion of *n*-heptane, and not toluene, it is plausible that the species produced in the NTC region where aerosols are observed experimentally are involved in the formation pathways of the aerosols. Notably, the 13 species included in the mole fraction profiles in Figure 2.3b (10 cyclic ethers and 3 heptene isomers) comprise only ~1% of the total number of reactions in the mechanism of Mehl et al. (Mehl et al., 2011) (1389 species), yet account for ~20% of the gas-phase product formation in the NTC region of *n*-heptane. Moreover, cyclic ethers may provide what effectively serves as the first ring required for particle formation in low-temperature combustion, similar to that required for the HACA mechanism (Wang, 2011) for high-temperature combustion, which is initiated via propargyl + propargyl, propargyl + allyl, among other reactions to provide the first ring. The pathways that may unfold after the initial (cyclic ether) ring are unclear. However, as cyclic ethers become oxidized and increasingly unsaturated, low-temperature particle formation may follow a HACA-type mechanism with one or more oxygen atoms embedded in polycyclic

structures, the presence which may alter aerosol reactivity, physical properties, and optical properties.

### 2.3.3. Volatility and molecular sizes

Figure 2.4 shows the aerosol mass fraction remaining (MFR) at different thermodenuder temperatures, or thermograms. At a combustion-chamber temperature of 1035 °C, the thermogram of *n*-heptane-combustion aerosol is steeper than that of toluene-combustion aerosol, indicating that the *n*-heptane-combustion aerosol is more volatile. At the largest thermodenuder temperature (150 °C), MFR of toluene-combustion aerosol was 0.17 compared to 0.06 for *n*-heptane-combustion aerosol. The aerosol produced in the low-temperature region from *n*-heptane-combustion (290 °C; Figure 2.2a) evaporated completely (i.e. MFR = 0) at thermodenuder temperature of 100 °C, indicating that it was significantly more volatile than the aerosol produced by the same fuel at 1035 °C. These results suggest a strong dependence of aerosol volatility on fuel type and combustion temperature.

Differences in aerosol volatility have implications to the atmospheric concentrations and lifecycle of the aerosol species. Specifically, even for the same emission rate, a relatively low-volatility aerosol would have higher atmospheric particle concentrations than a relatively high-volatility aerosol because it is more resistant to evaporation upon dilution in the atmosphere (Donahue et al., 2006). On the other hand, the amounts of semi-volatile organic compounds (SVOCs) that partition into the gas phase upon dilution in the atmosphere would be higher for the high-volatility aerosol. SVOCs are efficient secondary organic aerosol (SOA) precursors (Zhao et al., 2017). Thus, the high-volatility aerosol emissions can potentially lead to higher levels of SOA than the low-volatility aerosol emissions.

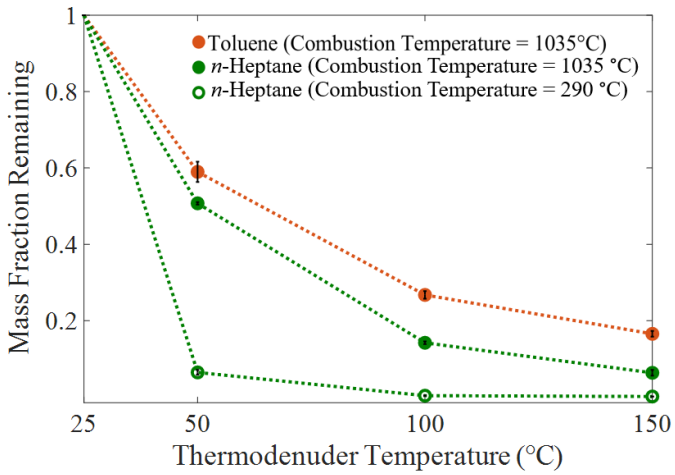


**Figure 2.4.** Thermograms showing mass fraction remaining (MFR) of toluene and *n*-heptane combustion aerosols at different thermodenuder temperatures.

Mass spectra obtained from LDI-MS measurements for the aerosol emitted from toluene and *n*-heptane combustion at combustion-chamber temperature of 1035 °C are shown in Figure 2.5a for m/z < 700 and Figure 2.5b for 1500 < m/z < 2100. Molecules emitted from both fuels exhibited similar signatures, with spacings of 12 and 24 atomic mass units that are characteristic of organic molecules in incipient soot undergoing growth by the hydrogen-abstraction acetylene-addition (HACA) mechanism (Wang, 2011). Similar signatures have been previously observed in LDI-MS measurements of incipient soot (Atwi et al., 2021; Faccinetto et al., 2011; Saleh et al., 2018). The peak intensities for m/z < 700 are of similar magnitude for the emissions from both fuels. However, toluene-combustion aerosols had higher intensities in the large-molecular-size range (Figure 2.5b), indicating that toluene-combustion aerosols had more abundance of large-molecular-size species than aerosols emitted from *n*-heptane combustion. This is in-line with the finding that toluene-combustion aerosols were less volatile than the *n*-heptane-combustion aerosols (Figure 2.4) because for species with similar general molecular structure (e.g. the incipient soot produced in these experiments), volatility decreases with increasing molecular size (Donahue et al., 2011). We note that due to differences in ionization and desorption efficiencies

of different molecules, the comparison shown in Figure 2.5 is qualitative. Specifically, we expect the ionization and desorption, thus signal intensity (Cristadoro et al., 2007), to decrease with increasing molecular size. Therefore, we expect that in reality, the difference in abundance of molecules on the large-end of the spectra to be more prominent than depicted in Figure 2.5b. The aerosol emissions from *n*-heptane combustion in the low-temperature region did not exhibit any discernible LDI-MS mass spectra. The LDI-MS technique requires that the sample absorbs the 337 nm laser significantly enough in order for it to desorb. As discussed in Section 3.4, the aerosol emissions from *n*-heptane combustion at low temperatures exhibited weak absorption in the visible spectrum, thus it is likely they were not absorptive enough to be detected by LDI-MS. Based on their high volatility (Figure 2.4), we expect these aerosols to be comprised of species with smaller molecular size than those emitted in the high-temperature region.

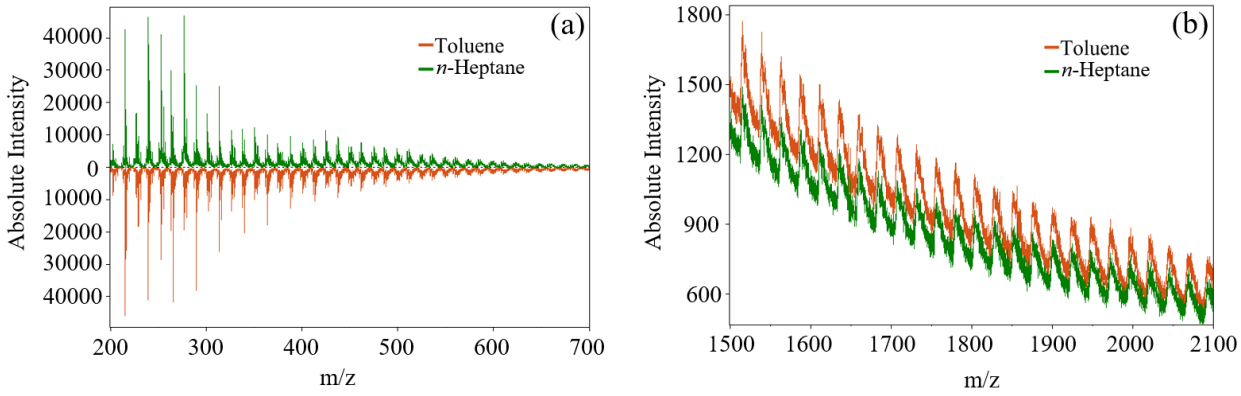


**Figure 2.5.** LDI-MS spectra of aerosol emitted from toluene and *n*-heptane combustion at 1035 °C.

### 2.3.4. Light-absorption properties

The light-absorption properties of the aerosol emitted from the combustion of toluene (at combustion-chamber temperature of 1035 °C) and *n*-heptane (at combustion-chamber temperature of 1035 °C and 290 °C) are depicted in Figure 2.6. Figure 2.6a shows the imaginary part of the refractive indices at 422 nm, 532 nm, and 782 nm ($k_{422}$, $k_{532}$, and $k_{782}$, respectively)

retrieved from optical closure and Figure 2.6b shows the mass absorption cross-sections ($MAC_{422}$, $MAC_{532}$, and $MAC_{782}$) obtained from normalizing the measured absorption coefficients by the mass concentration (Section 2.3). At combustion-chamber temperature of 1035 °C, aerosols from both toluene and *n*-heptane combustion exhibit significant absorption in the visible spectrum and are categorized as brown carbon (BrC). The toluene-combustion aerosol is more absorptive (has larger *k* and MAC) than the *n*-heptane-combustion aerosol, which is visually manifested as darker samples when collected on Teflon filters (Figure 2.6c). However, *k* and MAC of *n*-heptane-combustion aerosol have a stronger wavelength dependence ($w = 7.6$ and AAE = 8.7) than toluene-combustion aerosol ($w = 4.1$ and AAE = 5.6). This inverse relation between *k* and *w* (MAC and AAE) is consistent with previous reports showing that more absorptive BrC is characterized with flatter absorption spectra (Cheng et al., 2019; McClure et al., 2020; Saleh, 2020; Saleh et al., 2018; Saleh et al., 2014).

We note that these findings, in conjunction with the differences in molecular sizes (Figure 2.5) and volatility (Figure 2.4), are consistent with the brown-black continuum hypothesis that we have previously introduced to describe the light-absorbing carbonaceous aerosols, including BrC and BC, generated via the soot-formation route in combustion (Saleh et al., 2018). As the soot-formation process progresses toward full maturation (BC formation), it produces incipient soot (or BrC) comprised of increasingly larger organic molecules that are less volatile and more light-absorbing (larger *k* and smaller *w*). Our results indicate that toluene-combustion BrC is further ahead in the soot-formation process than *n*-heptane-combustion BrC (closer to the BC-formation threshold) and is therefore darker, less volatile, and exhibits molecular size distributions skewed toward larger sizes than *n*-heptane-combustion BrC.

For *n*-heptane combustion at 290 °C, the emitted aerosol exhibited measurable absorption only at 422 nm (Figure 2.6a and2. 6b) and was thus barely visible when collected on a Teflon filter (Figure 2.6c).

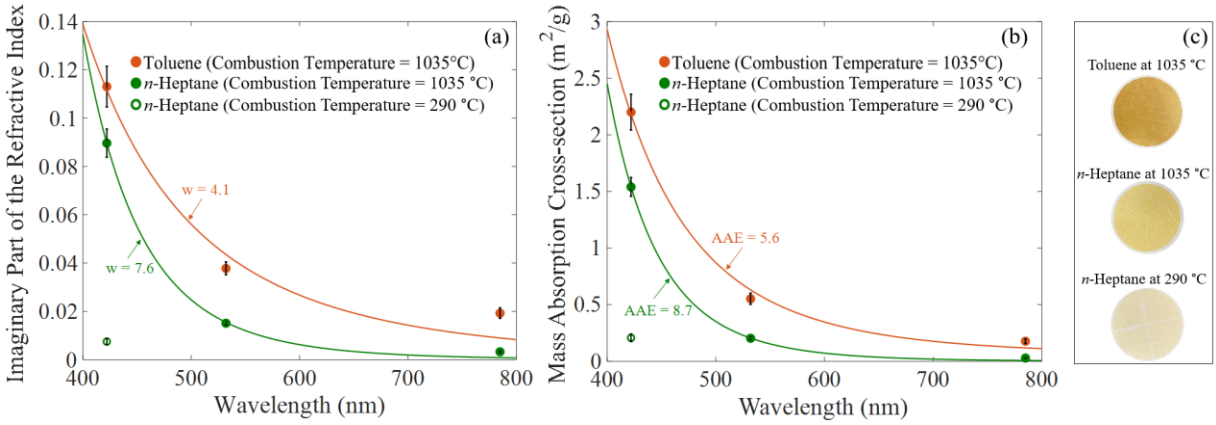


**Figure 2.6.** Light-absorption properties of aerosols emitted from toluene and *n*-heptane combustion. (a) Imaginary part of the refractive index (*k*) at different wavelengths. (b) Mass absorption cross section (MAC) at different wavelengths. Solid lines are power-law fits and the exponents are *w* and AAE, which represent the wavelength depends of *k* and MAC, respectively. The aerosol emitted from *n*-heptane combustion at 290 °C did not exhibit measurable absorption at 532 nm and 782 nm, thus light-absorption properties are only reported at 422 nm (open green circles in panels (a) and (b)). (c) Pictures of filter samples that visually illustrate the differences in optical properties of the aerosol emissions.

The BrC (incipient soot) emissions at the low-temperature combustion conditions in this study are significantly less absorptive than the BC (mature soot) emitted at typical CDC or laboratory flame conditions. Mature soot has $MAC_{532} \approx 8$ g/m$^2$ and relatively flat wavelength dependence with AAE ≈ 1 (Bond & Bergstrom, 2006). An important implication of this difference in light-absorption properties is that incipient soot produced at low-temperature combustion conditions would not be accurately quantified using techniques that rely on optical measurements tailored for mature soot, e.g. filter smoke number (FSN) or microsoot sensor (MSS) (Ciatti et al., 2013; Sellnau et al., 2016; Sellnau et al., 2015; Storey et al., 2017). The MSS is a photoacoustic

instrument that converts absorption measurements at 880 nm to soot mass concentrations based on calibration against combustion soot with high EC content (i.e. mature soot) (Durdina et al., 2016). Therefore, embedded in the reported MSS mass concentrations is an assumption that the measured aerosol has the same $MAC_{880}$ as mature soot ($\approx 5$ g/m$^2$). The aerosol emitted from toluene and *n*-heptane combustion at 1035 °C had $MAC_{880}$ of 0.03 g/m$^2$ and 0.0025 g/m$^2$, respectively, a factor of 152 and 1963 smaller than $MAC_{880}$ of EC. Therefore, their mass concentrations would be underestimated by the same factors if measured using a MSS. Such large underestimation in mass concentrations of aerosol emissions from engines operated at LTC conditions has been previously reported for FSN (Storey et al., 2017) and MSS (Moses-DeBusk et al., 2019). Our findings provide support for these reports and further indicate that optical absorption instruments are not suitable for quantifying LTC aerosol emissions even if they are calibrated with aerosol emissions at LTC conditions. Unlike mature soot which has relatively uniform light-absorption properties (Bond et al., 2013) regardless of emission source (conventional diesel combustion, laboratory diffusion flames, etc.), the light-absorption properties of incipient soot produced at LTC conditions can vary over several orders of magnitude depending on combustion conditions (Figure 2.6), making it impossible to produce a calibration standard.

## 2.4. Conclusions

Using an atmospheric-pressure reactor controlled at a constant equivalence ratio and $O_2/N_2$, we investigated the effect of combustion temperature on the formation and physicochemical properties of aerosols emitted from the combustion of toluene at *n*-heptane at temperatures between 200 °C and 1035 °C. Consistent with fuel reactivity versus temperature profiles predicted by ignition chemistry simulations, aerosol emission factors from toluene combustion

exhibited steep decrease with decreasing combustion temperature, while the emission rates from *n*-heptane combustion exhibited steep decrease with decreasing temperatures followed by resurgence that peaked at 290 °C. The physicochemical properties of the aerosols varied with both fuel type and combustion temperature. At 1035 °C, toluene combustion produced aerosols with molecular size distributions skewed to larger sizes compared to aerosols emitted from *n*-heptane. The toluene-combustion aerosols were also less volatile and more light-absorbing (darker), though both toluene-combustion and *n*-heptane-combustion aerosols are categorized as brown carbon (BrC). For *n*-heptane combustion, the aerosols emitted at 290 °C were significantly less light-absorbing and more volatile than those emitted at 1035 °C. The findings reported here provide the first evidence for the strong dependence of aerosol formation at low-temperature combustion conditions on ignition chemistry, particularly the two-stage aerosol formation in *n*-heptane combustion that reflects its two-stage ignition chemistry behavior. They also highlight the importance of further investigating the parameter space (fuel type and combustion conditions) associated with aerosol emissions at LTC conditions in order to identify regions within this space that can potentially minimize the emissions.

**Acknowledgments**

We thank the University of Georgia Proteomics and Mass Spectrometry Core Facility for performing the LDI-MS analysis. Financial support was provided by the National Science Foundation, Division of Atmospheric and Geospace Sciences (AGS-1748080) and the University of Georgia Interdisciplinary Seed Grant Initiative.

## References


Agarwal, A. K., Singh, A. P., & Maurya, R. K. (2017). Evolution, challenges and path forward for low temperature combustion engines. *Progress in Energy and Combustion Science*, *61*, 1-56.

Akridis, P., & Rigopoulos, S. (2017). Modelling of soot formation in laminar diffusion flames using a comprehensive CFD-PBE model with detailed gas-phase chemistry. *Combustion Theory and Modelling*, *21*(1), 35-48.

An, Y., Jaasim, M., Raman, V., Im, H. G., & Johansson, B. (2018). In-cylinder combustion and soot evolution in the transition from conventional compression ignition (CI) mode to partially premixed combustion (PPC) mode. *Energy & Fuels*, *32*(2), 2306-2320.

Andreae, M., & Gelencsér, A. (2006). Black carbon or brown carbon? The nature of light-absorbing carbonaceous aerosols.

Apicella, B., Alfè, M., Amoresano, A., Galano, E., & Ciajolo, A. (2010). Advantages and limitations of laser desorption/ionization mass spectrometric techniques in the chemical characterization of complex carbonaceous materials. *International Journal of Mass Spectrometry*, *295*(1-2), 98-102.

Apicella, B., Carpentieri, A., Alfè, M., Barbella, R., Tregrossi, A., Pucci, P., & Ciajolo, A. (2007). Mass spectrometric analysis of large PAH in a fuel-rich ethylene flame. *Proceedings of the Combustion Institute*, *31*(1), 547-553.

Appel, J., Bockhorn, H., & Frenklach, M. (2000). Kinetic modeling of soot formation with detailed chemistry and physics: laminar premixed flames of C2 hydrocarbons. *Combustion and flame*, *121*(1-2), 122-136.

Atwi, K., Mondal, A., Pant, J., Cheng, Z., El Hajj, O., Ijeli, I., Handa, H., & Saleh, R. Physicochemical properties and cytotoxicity of brown carbon produced under different combustion conditions. *Atmospheric Environment*, *244*, 117881.

Atwi, K., Mondal, A., Pant, J., Cheng, Z., El Hajj, O., Ijeli, I., Handa, H., & Saleh, R. (2021). Physicochemical properties and cytotoxicity of brown carbon produced under different combustion conditions. *Atmospheric Environment*, *244*, 117881.

Bohren, C. F., & Huffman, D. R. (2008). *Absorption and scattering of light by small particles*. John Wiley & Sons.

Bond, T. C., & Bergstrom, R. W. (2006). Light absorption by carbonaceous particles: An investigative review. *Aerosol science and technology*, *40*(1), 27-67.

Bond, T. C., Doherty, S. J., Fahey, D. W., Forster, P. M., Berntsen, T., DeAngelo, B. J., Flanner, M. G., Ghan, S., Kärcher, B., & Koch, D. (2013). Bounding the role of black carbon in the climate system: A scientific assessment. *Journal of Geophysical Research: Atmospheres*, *118*(11), 5380-5552.

Cheng, Z., Atwi, K., Hajj, O. E., Ijeli, I., Fischer, D. A., Smith, G., & Saleh, R. (2020). Discrepancies between brown carbon light-absorption properties retrieved from online and offline measurements. *Aerosol Science and Technology*, 1-12.

Cheng, Z., Atwi, K., Onyima, T., & Saleh, R. (2019). Investigating the dependence of light-absorption properties of combustion carbonaceous aerosols on combustion conditions. *Aerosol Science and Technology*, *53*(4), 419-434.

Cheng, Z., Atwi, K. M., Yu, Z., Avery, A., Fortner, E. C., Williams, L., Majluf, F., Krechmer, J. E., Lambe, A. T., & Saleh, R. (2020). Evolution of the light-absorption properties of combustion brown carbon aerosols following reaction with nitrate radicals. *Aerosol*

*Science and Technology*, *54*(7), 849-863. https://doi.org/10.1080/02786826.2020.1726867
Christensen, M., & Johansson, B. (1998). Influence of mixture quality on homogeneous charge compression ignition. *SAE Transactions*, 951-963.
Ciatti, S., Johnson, M., Adhikary, B. D., Reitz, R. D., & Knock, A. (2013). *Efficiency and emissions performance of multizone stratified compression ignition using different octane fuels* (0148-7191).
Contino, F., Foucher, F., Mounaïm-Rousselle, C., & Jeanmart, H. (2011). Combustion characteristics of tricomponent fuel blends of ethyl acetate, ethyl propionate, and ethyl butyrate in homogeneous charge compression ignition (HCCI). *Energy & Fuels*, *25*(4), 1497-1503.
Cristadoro, A., Räder, H. J., & Müllen, K. (2007). Clustering of polycyclic aromatic hydrocarbons in matrix-assisted laser desorption/ionization and laser desorption mass spectrometry. *Rapid Communications in Mass Spectrometry: An International Journal Devoted to the Rapid Dissemination of Up-to-the-Minute Research in Mass Spectrometry*, *21*(16), 2621-2628.
Cross, E. S., Slowik, J. G., Davidovits, P., Allan, J. D., Worsnop, D. R., Jayne, J. T., Lewis, D. K., Canagaratna, M., & Onasch, T. B. (2007). Laboratory and ambient particle density determinations using light scattering in conjunction with aerosol mass spectrometry. *Aerosol Science and Technology*, *41*(4), 343-359.
Dec, J. E. (2009). Advanced compression-ignition engines—understanding the in-cylinder processes. *Proceedings of the Combustion Institute*, *32*(2), 2727-2742.
Dec, J. E., & Hwang, W. (2009). Characterizing the development of thermal stratification in an HCCI engine using planar-imaging thermometry. *SAE International Journal of Engines*, *2*(1), 421-438.
Donahue, N. M., Epstein, S., Pandis, S. N., & Robinson, A. L. (2011). A two-dimensional volatility basis set: 1. organic-aerosol mixing thermodynamics. *Atmospheric Chemistry and Physics*, *11*(7), 3303-3318.
Donahue, N. M., Robinson, A., Stanier, C., & Pandis, S. (2006). Coupled partitioning, dilution, and chemical aging of semivolatile organics. *Environmental science & technology*, *40*(8), 2635-2643.
Durdina, L., Lobo, P., Trueblood, M. B., Black, E. A., Achterberg, S., Hagen, D. E., Brem, B. T., & Wang, J. (2016). Response of real-time black carbon mass instruments to mini-CAST soot. *Aerosol Science and Technology*, *50*(9), 906-918.
Epping, K., Aceves, S., Bechtold, R., & Dec, J. E. (2002). *The potential of HCCI combustion for high efficiency and low emissions* (0148-7191).
Faccinetto, A., Desgroux, P., Ziskind, M., Therssen, E., & Focsa, C. (2011). High-sensitivity detection of polycyclic aromatic hydrocarbons adsorbed onto soot particles using laser desorption/laser ionization/time-of-flight mass spectrometry: An approach to studying the soot inception process in low-pressure flames. *Combustion and Flame*, *158*(2), 227-239.
Faccinetto, A., Focsa, C., Desgroux, P., & Ziskind, M. (2015). Progress toward the quantitative analysis of PAHs adsorbed on soot by laser desorption/laser ionization/time-of-flight mass spectrometry. *Environmental science & technology*, *49*(17), 10510-10520.
Fattah, I. R., Ming, C., Chan, Q., Wehrfritz, A., Pham, P., Yang, W., Kook, S., Medwell, P., Yeoh, G., & Hawkes, E. (2018). Spray and combustion investigation of post injections

under low-temperature combustion conditions with biodiesel. *Energy & Fuels*, *32*(8), 8727-8742.
Fischer, D. A., & Smith, G. D. (2018). A portable, four-wavelength, single-cell photoacoustic spectrometer for ambient aerosol absorption. *Aerosol Science and Technology*, *52*(4), 393-406.
Gordon, T., Presto, A., May, A., Nguyen, N., Lipsky, E., Donahue, N., Gutierrez, A., Zhang, M., Maddox, C., & Rieger, P. (2014). Secondary organic aerosol formation exceeds primary particulate matter emissions for light-duty gasoline vehicles. *Atmospheric Chemistry and Physics*, *14*(9), 4661-4678.
Han, M. (2013). The effects of synthetically designed diesel fuel properties–cetane number, aromatic content, distillation temperature, on low-temperature diesel combustion. *Fuel*, *109*, 512-519.
Hanson, R. M., Kokjohn, S. L., Splitter, D. A., & Reitz, R. D. (2010). An experimental investigation of fuel reactivity controlled PCCI combustion in a heavy-duty engine. *SAE international journal of engines*, *3*(1), 700-716.
Hellier, P., Ladommatos, N., Allan, R., & Rogerson, J. (2013). Combustion and emissions characteristics of toluene/n-heptane and 1-octene/n-octane binary mixtures in a direct injection compression ignition engine. *Combustion and Flame*, *160*(10), 2141-2158.
Johansson, K., Head-Gordon, M., Schrader, P., Wilson, K., & Michelsen, H. (2018). Resonance-stabilized hydrocarbon-radical chain reactions may explain soot inception and growth. *Science*, *361*(6406), 997-1000.
Josephson, A. J., Linn, R. R., & Lignell, D. O. (2018). Modeling soot formation from solid complex fuels. *Combustion and Flame*, *196*, 265-283.
Ju, Y., Sun, W., Burke, M. P., Gou, X., & Chen, Z. (2011). Multi-timescale modeling of ignition and flame regimes of n-heptane-air mixtures near spark assisted homogeneous charge compression ignition conditions. *Proceedings of the Combustion Institute*, *33*(1), 1245-1251.
Kang, D., Shah, A., Rockstroh, T., & Goldsborough, S. (2019). *Utilizing static autoignition measurements to estimate intake air condition requirements for compression ignition in a multi-mode engine-Application of Chemical Kinetic Modeling* (0148-7191).
Kitamura, T., Ito, T., Kitamura, Y., Ueda, M., Senda, J., & Fujimoto, H. (2003). Soot kinetic modeling and empirical validation on smokeless diesel combustion with oxygenated fuels. *SAE Transactions*, 945-963.
Kumar, B. R., & Saravanan, S. (2016). Effects of iso-butanol/diesel and n-pentanol/diesel blends on performance and emissions of a DI diesel engine under premixed LTC (low temperature combustion) mode. *Fuel*, *170*, 49-59.
Laskin, A., Laskin, J., & Nizkorodov, S. A. (2015). Chemistry of Atmospheric Brown Carbon. *Chemical Reviews*, *115*(10), 4335-4382. https://doi.org/10.1021/cr5006167
Lee, C. S., Lee, K. H., & Kim, D. S. (2003). Experimental and numerical study on the combustion characteristics of partially premixed charge compression ignition engine with dual fuel☆. *Fuel*, *82*(5), 553-560.
Liu, H., Bi, X., Huo, M., Lee, C.-f. F., & Yao, M. (2012). Soot emissions of various oxygenated biofuels in conventional diesel combustion and low-temperature combustion conditions. *Energy & Fuels*, *26*(3), 1900-1911.

Lu, X., Han, D., & Huang, Z. (2011). Fuel design and management for the control of advanced compression-ignition combustion modes. *Progress in Energy and Combustion Science*, *37*(6), 741-783.

Lucachick, G., Curran, S., Storey, J., Prikhodko, V., & Northrop, W. F. (2016). Volatility characterization of nanoparticles from single and dual-fuel low temperature combustion in compression ignition engines. *Aerosol Science and Technology*, *50*(5), 436-447.

Machrafi, H. (2008). Experimental validation of a kinetic multi-component mechanism in a wide HCCI engine operating range for mixtures of n-heptane, iso-octane and toluene: Influence of EGR parameters. *Energy conversion and management*, *49*(11), 2956-2965.

McClure, C. D., Lim, C. Y., Hagan, D. H., Kroll, J. H., & Cappa, C. D. (2020). Biomass-burning-derived particles from a wide variety of fuels–Part 1: Properties of primary particles. *Atmospheric Chemistry and Physics*, *20*(3), 1531-1547.

McMurry, P. H., Wang, X., Park, K., & Ehara, K. (2002). The relationship between mass and mobility for atmospheric particles: A new technique for measuring particle density. *Aerosol Science & Technology*, *36*(2), 227-238.

Mehl, M., Pitz, W. J., Westbrook, C. K., & Curran, H. J. (2011). Kinetic modeling of gasoline surrogate components and mixtures under engine conditions. *Proceedings of the Combustion Institute*, *33*(1), 193-200.

Michelsen, H. (2017). Probing soot formation, chemical and physical evolution, and oxidation: A review of in situ diagnostic techniques and needs. *Proceedings of the Combustion Institute*, *36*(1), 717-735.

Moses-DeBusk, M., Curran, S. J., Lewis, S. A., Connatser, R. M., & Storey, J. M. (2019). Impacts of Air-Fuel Stratification in ACI Combustion on Particulate Matter and Gaseous Emissions. *Emission Control Science and Technology*, *5*(3), 225-237.

Mueller, M., Blanquart, G., & Pitsch, H. (2009). Hybrid method of moments for modeling soot formation and growth. *Combustion and Flame*, *156*(6), 1143-1155.

Northrop, W. F., Madathil, P. V., Bohac, S. V., & Assanis, D. N. (2011). Condensational growth of particulate matter from partially premixed low temperature combustion of biodiesel in a compression ignition engine. *Aerosol Science and Technology*, *45*(1), 26-36.

Ortiz-Soto, E. A., Lavoie, G. A., Wooldridge, M. S., & Assanis, D. N. (2019). Thermodynamic efficiency assessment of gasoline spark ignition and compression ignition operating strategies using a new multi-mode combustion model for engine system simulations. *International Journal of Engine Research*, *20*(3), 304-326.

Reitz, R. D., & Duraisamy, G. (2015). Review of high efficiency and clean reactivity controlled compression ignition (RCCI) combustion in internal combustion engines. *Progress in Energy and Combustion Science*, *46*, 12-71.

Ryan, T. W., & Matheaus, A. C. (2003). Fuel Requirements for HCCI Engine Operation. *SAE Transactions*, *112*, 1143-1152. www.jstor.org/stable/44742337

Saleh, R. (2020). From Measurements to Models: Toward Accurate Representation of Brown Carbon in Climate Calculations. *Current Pollution Reports*, *6*(2), 90-104. https://doi.org/10.1007/s40726-020-00139-3

Saleh, R., Cheng, Z., & Atwi, K. (2018). The brown–black continuum of light-absorbing combustion aerosols. *Environmental Science & Technology Letters*, *5*(8), 508-513.

Saleh, R., Robinson, E. S., Tkacik, D. S., Ahern, A. T., Liu, S., Aiken, A. C., Sullivan, R. C., Presto, A. A., Dubey, M. K., & Yokelson, R. J. (2014). Brownness of organics in

aerosols from biomass burning linked to their black carbon content. *Nature Geoscience*, *7*(9), 647-650.
Saleh, R., Shihadeh, A., & Khlystov, A. (2011). On transport phenomena and equilibration time scales in thermodenuders. *Atmospheric Measurement Techniques*, *4*(3), 571-581.
Schmid, O., Chand, D., Karg, E., Guyon, P., Frank, G. P., Swietlicki, E., & Andreae, M. O. (2009). Derivation of the density and refractive index of organic matter and elemental carbon from closure between physical and chemical aerosol properties. *Environmental science & technology*, *43*(4), 1166-1172.
Sellnau, M., Foster, M., Moore, W., Sinnamon, J., Hoyer, K., & Klemm, W. (2016). Second generation GDCI multi-cylinder engine for high fuel efficiency and US tier 3 emissions. *SAE International Journal of Engines*, *9*(2), 1002-1020.
Sellnau, M., Moore, W., Sinnamon, J., Hoyer, K., Foster, M., & Husted, H. (2015). GDCI multi-cylinder engine for high fuel efficiency and low emissions. *Sae international journal of engines*, *8*(2), 775-790.
Shahbakhti, M., Ghazimirsaied, A., & Koch, C. R. (2010). Experimental study of exhaust temperature variation in a homogeneous charge compression ignition engine. *Proceedings of the Institution of Mechanical Engineers, Part D: Journal of Automobile Engineering*, *224*(9), 1177-1197. https://doi.org/10.1243/09544070jauto1473
Soloiu, V., Moncada, J. D., Gaubert, R., Muiños, M., Harp, S., Ilie, M., Zdanowicz, A., & Molina, G. (2018). LTC (low-temperature combustion) analysis of PCCI (premixed charge compression ignition) with n-butanol and cotton seed biodiesel versus combustion and emissions characteristics of their binary mixtures. *Renewable Energy*, *123*, 323-333.
Splitter, D., Hanson, R., Kokjohn, S., & Reitz, R. D. (2011). *Reactivity controlled compression ignition (RCCI) heavy-duty engine operation at mid-and high-loads with conventional and alternative fuels* (0148-7191).
Stanglmaier, R. H., & Roberts, C. E. (1999). Homogeneous charge compression ignition (HCCI): benefits, compromises, and future engine applications. *SAE Transactions*, 2138-2145.
Storey, J. M., Curran, S. J., Lewis, S. A., Barone, T. L., Dempsey, A. B., Moses-DeBusk, M., Hanson, R. M., Prikhodko, V. Y., & Northrop, W. F. (2017). Evolution and current understanding of physicochemical characterization of particulate matter from reactivity controlled compression ignition combustion on a multicylinder light-duty engine. *International Journal of Engine Research*, *18*(5-6), 505-519.
Thring, R. H. (1989). *Homogeneous-charge compression-ignition (HCCI) engines* (0148-7191).
Wang, H. (2011). Formation of nascent soot and other condensed-phase materials in flames. *Proceedings of the Combustion institute*, *33*(1), 41-67.
Williams, S., Hu, L., Nakazono, T., Ohtsubo, H., & Uchida, M. (2009). Oxidation catalysts for natural gas engine operating under HCCI or SI conditions. *SAE International Journal of Fuels and Lubricants*, *1*(1), 326-337.
Worton, D. R., Isaacman, G., Gentner, D. R., Dallmann, T. R., Chan, A. W., Ruehl, C., Kirchstetter, T. W., Wilson, K. R., Harley, R. A., & Goldstein, A. H. (2014). Lubricating oil dominates primary organic aerosol emissions from motor vehicles. *Environmental science & technology*, *48*(7), 3698-3706.
Yen, M., Magi, V., & Abraham, J. (2018). Modeling Soot Formation in Turbulent Jet Flames at Atmospheric and High-Pressure Conditions. *Energy & Fuels*, *32*(8), 8857-8867.

Zádor, J., Taatjes, C. A., & Fernandes, R. X. (2011). Kinetics of elementary reactions in low-temperature autoignition chemistry. *Progress in Energy and Combustion Science*, *37*(4), 371-421.

Zhao, F., Asmus, T. N., Assanis, D. N., Dec, J. E., Eng, J. A., & Najt, P. M. (2003). *Homogeneous charge compression ignition (HCCI) engines*.

Zhao, Y., Saleh, R., Saliba, G., Presto, A. A., Gordon, T. D., Drozd, G. T., Goldstein, A. H., Donahue, N. M., & Robinson, A. L. (2017). Reducing secondary organic aerosol formation from gasoline vehicle exhaust. *Proceedings of the National Academy of Sciences*, *114*(27), 6984-6989.

Zhong, S., Wyszynski, M., Megaritis, A., & Yap, D. (2005). *H. Xu,"Experimental Investigation into HCCI Combustion Using Gasoline and Diesel Blended Fuels,"SAE technical paper*.

# CHAPTER 3

# ALKYLPEROXY RADICALS ARE RESPONSIBLE FOR THE FORMATION OF OXYGENATED PRIMARY ORGANIC AEROSOL [2]

[2] El Hajj, O., Hartness, S.W., Gregory, W.V., Park, Y., Glenn, C.K., Anosike, A., Webb, A.R., Dewey, N.S., Doner, A.C., Cheng, Z., Jatana, G., Moses-Debusk, M., China, S., Rotavera, B., Saleh, R. Submitted to *Science Advances*

**Abstract**

Organic aerosol (OA) is an air pollutant ubiquitous in urban atmospheres. Urban OA is usually apportioned into primary OA (POA), mostly emitted by mobile sources, and secondary OA (SOA), which forms in the atmosphere due to oxidation of gas-phase precursors from anthropogenic and biogenic sources. By performing coordinated measurements in the particle phase and the gas phase, we show that alkylperoxy radical chemistry that is responsible for low-temperature ignition also leads to the formation of oxygenated POA (OxyPOA). OxyPOA is distinct from POA emitted during high-temperature ignition and is chemically similar to SOA. We present evidence for the prevalence of OxyPOA in emissions of a spark-ignition engine and a next-generation advanced compression-ignition engine, highlighting the importance of OxyPOA for understanding urban air pollution.

### 3.1. Introduction

Atmospheric aerosols exhibit profound impacts on air quality and the climate. Commonly referred to as particulate matter (PM) in the public-health community, aerosols are associated with various health effects and inflict the highest social cost among air pollutants (Dockery et al., 1993; Pervin et al., 2008). Unlike greenhouse gases, which perturb the atmospheric radiative balance via a straightforward mechanism (the greenhouse gas effect), aerosols exhibit complex direct and indirect interactions with atmospheric radiation, rendering them the largest contributor to uncertainty in climate calculations (Pörtner et al., 2022). Organic aerosol (OA) constitutes the majority of submicron aerosol mass in both urban and rural atmospheres (Jimenez et al., 2009). A large fraction of OA forms via diverse gas-phase chemical reaction pathways that produce molecules with low volatilities, favoring particle formation via condensation. Such reactions occur during combustion (Johansson et al., 2018) leading to the formation of primary organic aerosol (POA), as well as in the atmosphere (Taatjes et al., 2013; Welz et al., 2012) leading to the formation of secondary organic aerosol (SOA). Though OA mass concentrations in the atmosphere can be quantified with relatively high confidence, detailed speciation of OA is challenging. In response, atmospheric chemists have devised creative techniques that allow grouping OA into different categories and linking these categories to sources (Jimenez et al., 2009). The most prevalent categorization framework is based on factor analysis applied to aerosol mass spectrometer (AMS) measurements (Ulbrich et al., 2009; Zhang et al., 2007). Under this framework, hydrocarbon-like OA (HOA) represents OA with low oxygen content (O/C < 0.1), while oxygenated OA (OOA) represents OA with high oxygen content (0.25 < O/C < 1). The current consensus is that OOA is predominantly composed of SOA, while urban POA, emitted from the combustion of hydrocarbon fuels (e.g. vehicle emissions), is HOA (Jimenez et al., 2009).

Here we show that hydrocarbon combustion can emit what we refer to as oxygenated POA (OxyPOA), which retains chemical properties similar to those of SOA. We present results from laboratory experiments that link OxyPOA formation to low-temperature combustion chemistry (Hansen et al., 2021; Rotavera & Taatjes, 2021; Savee et al., 2015). We also provide evidence of OxyPOA in emissions from spark-ignition and next-generation advanced compression-ignition engines, illustrating the relevance of elucidating OxyPOA formation to understanding OA pollution in current and future urban atmospheres.

## 3.2. Materials and methods

### 3.2.1. *n*-Pentane and *n*-heptane controlled combustion experiments

The setup used to generate first-stage and second-stage primary organic aerosol (POA) from the controlled combustion of *n*-pentane and *n*-heptane is shown in Figure 3.1 and is described in detail in previous studies (Atwi et al., 2021; Cheng, Atwi, Hajj, et al., 2020; Cheng et al., 2019; Cheng, Atwi, Yu, et al., 2020; El Hajj et al., 2021; Saleh et al., 2018). Briefly, fuel oxidation was temperature-initiated in a 0.24 L custom-built cylindrical quartz chamber enclosed in an insulated heater (Thermcraft Inc., NC, USA). Temperature was controlled to within 1 K using a PID controller (OMEGA, CNi3244) utilizing a high-temperature K-type thermocouple located at the center of the chamber. Fuel was introduced via a bubbler system using a mass flow controller (DAKOTA, 6AGC1AL55-09AB) to direct a stream of ultra-high purity $N_2$ (NI UHP300, Airgas) into a bubbler containing the fuel. The bubbler dimensions were designed to ensure that the $N_2$ stream was fully saturated with the fuel vapor at the exit of the bubbler, as verified by mass transfer calculations confirming that the residence time of a bubble rising in the bubbler is greater than the time required to saturate it with the fuel vapor (Cheng et al., 2019). This allowed us to calculate the flowrate of the fuel entering the combustion chamber based on the fuel

saturation pressure and $N_2$ flowrate. The fuel-saturated $N_2$ stream was then mixed with a controlled stream of clean dry air and $N_2$ to maintain an equivalence ratio ($\phi$) of 2.3 and $O_2/N_2$ of 0.06.

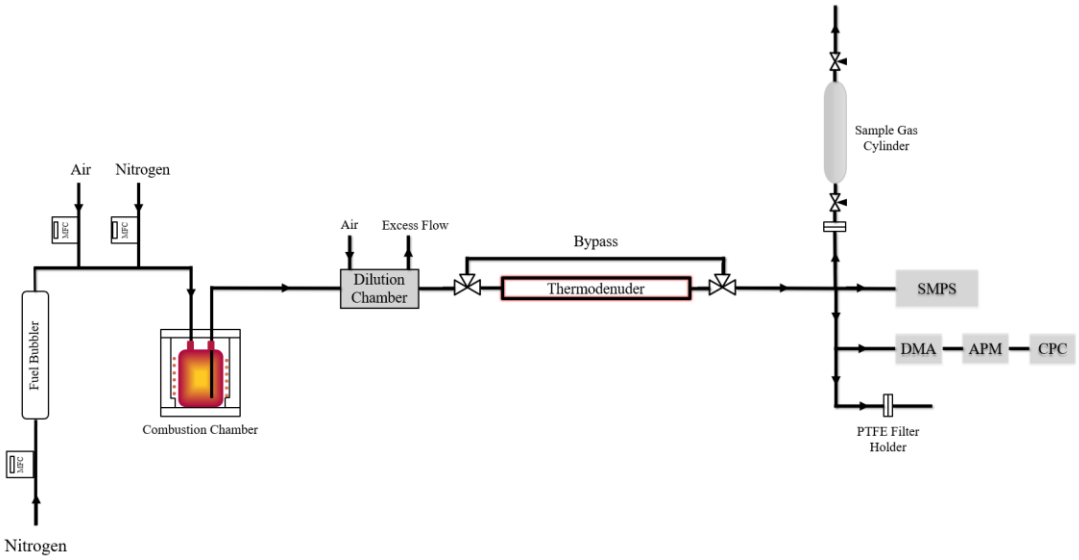


**Figure 3.1.** Schematic of the experimental setup for the controlled combustion of *n*-pentane and *n*-heptane.

The total flowrate into the combustion chamber was 0.75 SLPM, resulting in average residence time of approximately 19 seconds. The combustion emissions were then diluted in a 4 L glass dilution chamber with 12 SLPM of clean dry air prior to POA sampling. To observe first-stage and second-stage POA formation, the temperature of the combustion chamber was varied between 500 K and 1300 K and the size distributions of the POA emissions were continuously monitored at 90-second time resolution using a scanning mobility particle sizer (SMPS, TSI model 3088). The size distributions were integrated using a particle effective density of 1.3 $g/cm^3$, estimated using tandem differential mobility analyzer – aerosol particle mass analyzer (tandem DMA-APM) technique (El Hajj et al., 2021; McMurry et al., 2002), to obtain temperature-dependent POA mass concentration profiles. As shown in Figure 3.2, both *n*-

pentane and *n*-heptane exhibited two-stage aerosol formation. The first-stage POA peak emission was at 583 K and 563 K for *n*-pentane and *n*-heptane, respectively.

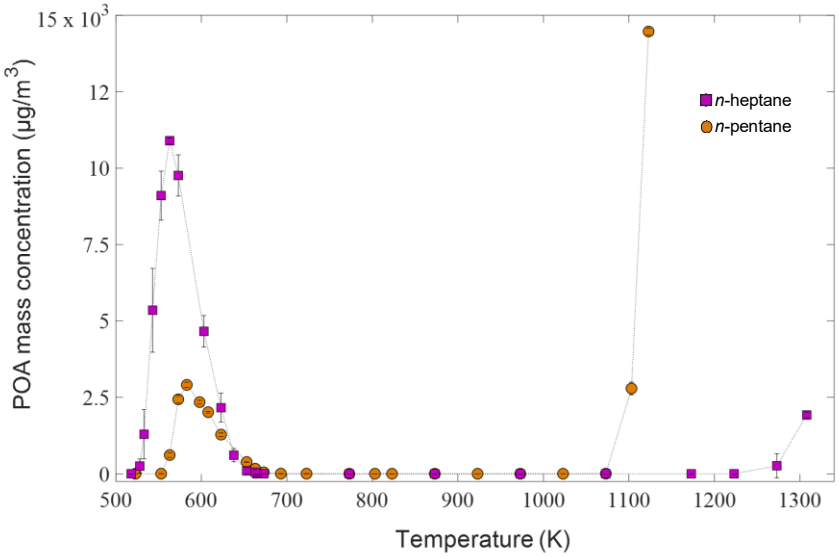


**Figure 3.2.** Mass concentrations (adjusted for dilution) of POA emissions from *n*-pentane and *n*-heptane combustion as a function of combustion temperature showing the first-stage POA (OxyPOA) and second-stage POA formation profiles. Error bars represent standard deviations from 5 SMPS scans.

We collected POA samples on 47 mm polytetrafluoroethylene (PTFE) filters (0.2 µm pore size, Whatman) for the chemical analyses described below. The collection flowrate was 5 SLPM and the targeted mass loading was 300 µg in order to avoid filter clogging which occurs at ~350 µg. Filters were stored at -15° C pending analysis. First-stage POA samples were collected at combustion temperature of 583 K and 563 K for *n*-pentane and *n*-heptane, respectively. Second-stage POA samples were collected at combustion temperature of 1123 K and 1308 K for *n*-pentane and *n*-heptane, respectively.

We also collected samples from *n*-pentane combustion for gas-phase chemical analysis (described below) using a 1-gallon (3.8 L) stainless steel double ended sample cylinder (304L-HDF4-1GAL, Swagelok) fitted with ¼ inch needle valves on both ends (Figure 3.1). The

combustion emissions were sampled directly into the cylinder from the combustion chamber (without dilution) at a flowrate of 0.5 SLPM, and the valves at the inlet and outlet of the cylinder were closed once steady state conditions were achieved. The POA was removed from the emissions using a PTFE filter prior to entering the cylinder. In order to compare the temperature-dependent concentration profiles of gas-phase species emitted during first-stage combustion to that of first-stage POA, we collected gas-phase samples at five temperature points: 543 K, 563 K, 598 K, 658 K, and 743 K. The second-stage gas-phase samples were collected at 1143 K.

### 3.2.2. Cold-start spark-ignition engine experiments

A single cylinder version of a GM LNF 2.0L direct-injected (DI) spark-ignited (SI) 4-cylinder engine was used for these experiments, wherein 3 of the cylinders were disabled by grinding off the cam lobes to prevent valve actuation as well as by drilling holes in the pistons to prevent compression. More details of the engine setup, instrumentation, and cold-start operation are available in previous studies on this engine (Jatana et al., 2021, 2023). Briefly, the firing cylinder was maintained in stock configuration, wherein the compression ratio, combustion chamber geometry, fuel injector, cam lobe profiles, and cam phasing capabilities were all stock. The engine was fueled with a 9-component surrogate fuel blend known as PACE20 that was designed by the Partnership to Advance Combustion Engines (PACE) consortium to closely mimic the fuel properties such as boiling range and octane rating, as well as engine emissions parameters such as sooting propensity of a market-representative 87 anti-knock index (AKI) E10 fuel while eliminating fuel composition uncertainties from chemical-kinetics modeling. The fuel composition and properties are detailed elsewhere (Jatana et al., 2023). Cold-start operation was simulated by operating the engine at 1300 RPM and 2 bar net indicated mean effective pressure (NIMEP) stoichiometric operation while the engine out coolant and oil temperature were

controlled to 20°C. For this study, spark timing was used as the engine control parameter to study engine emissions under normal and cold-start conditions. For the data presented in this study, the spark timing was fixed at 25 degrees after-top-dead-center-firing (dATDCf) and the exhaust gas was sampled 35mm downstream of the exhaust port.

### 3.2.3. Compression-ignition engine experiments

The conventional diesel combustion (CDC) and a premixed charge compression ignition (PCCI) samples were collected from the exhaust of a single-cylinder medium-duty diesel engine. A complete description of the engine and mode operation has been previously described (Curran et al., 2021). Briefly, a 6.7 L Cummins 6-cylinder ISB engine was modified to single cylinder operation by deactivating 5 cylinders and run for these samples on certified ultra-low-sulfur diesel no. USLD #2 fuel. The same engine was operated in both the CDC and PCCI modes to collect filters samples of aerosol emissions. A similar dilution tunnel set-up as that described for the cold-start experiments was used to collect aerosol samples on PTFE filters. Both samples were collected at 1200 rpm but the PCCI samples was at low load (1.8 bar) and the CDC sample was at high load (3.2 bar).

### 3.2.4. POA chemical analysis using laser desorption ionization mass spectrometry

LDI-MS is efficient at detecting incipient soot and has been extensively employed to study soot formation from various combustion sources (Apicella et al., 2007; Faccinetto et al., 2011; Faccinetto et al., 2015). We extracted the POA filter samples by sonicating in 2 ml of dichloromethane (DCM) for 40 minutes. The solutions were then concentrated to 1 ml by evaporation using a gentle stream of ultra-high purity N2. The solutions were then spotted onto a stainless-steel grid for LDI-MS analysis in 250 µL batches, allowing the DCM to evaporate after each batch. Based on our experience (Atwi et al.; El Hajj et al., 2021; Saleh et al., 2018) and in

concordance with previous studies (Apicella et al., 2007; Apicella et al., 2022; Michela et al., 2008; Russo et al., 2013), we chose DCM as a solvent for LDI-MS analysis due to its efficacy at extracting large-molecular-size polycyclic aromatic hydrocarbons (PAHs) that constitute incipient soot. LDI-MS analysis was performed on a Bruker Autoflex III in reflectron mode using AutoXecute. The instrument uses a 337 nm Nitrogen laser in positive mode. The ion source was set to 19 kV and the reflector voltage to 20 kV. Random walk with the raster was set to 2 shots per spot with a total of 100 laser shots. The laser was set to 100% intensity and the acquisition was set to 1000-1500 m/z to maximize the signal of the large-molecular-size PAHs.

**3.2.5. POA chemical analysis using electrospray ionization mass spectrometry**

ESI-MS is efficient at detecting relatively polar molecules (Bateman et al., 2012; Lin et al., 2016; Lin et al., 2018) and has been previously employed to perform chemical analysis on various types of organic aerosol (OA) samples, including biomass-burning OA (Bateman et al., 2010; Budisulistiorini et al., 2017; Lin et al., 2018), secondary OA (SOA) (Bateman et al., 2008; Kenseth et al., 2020; R. Zhao et al., 2018), and urban OA (Kitanovski et al., 2012; Teich et al., 2017). For Fourier-transform ion cyclotron resonance mass spectrometry (ESI-FTIRC-MS) analysis, the POA filters were extracted using the same procedure described above for LDI-MS analysis, but using acetonitrile as a solvent because of its efficacy at extracting polar compounds (Bateman et al., 2008; Cheng et al., 2016; Liu et al., 2013). An extraction blank with a clean PTFE filter was also prepared following the same steps and was used for background correction. Analysis was performed on a Bruker SolariX 12T FTICR mass spectrometer (Bruker Daltonik, GmbH, Bremen, Germany) in negative ion mode. Mass spectra were collected between 75-1000 m/z with 2M data points length and a 0.4194 second transient. Time of flight was set at 0.8 ms. Samples were infused at a rate of 2.0 μL/min. The capillary voltage was set to 4500 V with a -

800 V end plate offset. The nebulizer gas was set to 0.5 bar, and the dry gas was set to 4.0 L/min with a dry temperature of 200° C. Ion accumulation time was 0.005 seconds. Calibration was performed with sodium trifluoroacetate (Sigma-Aldrich) (0.1 mg/mL in 50:50 methanol:water). Spectra were collected in triplicate by doing three injections of 10 μL of sample. Prior to introducing samples to the instrument, methanol and extraction blanks were acquired.

For data analysis, 48 scans per injection per sample were averaged using Bruker Compass Data Analysis software (Version 5.3). Background subtraction was performed using Xpose mode with a retention time window of 0.0083s and a ratio of 5 in order to minimize noise signals and signals that were detected in the extraction blanks. MFAssignR (Schum et al., 2020), an open source R package, was used to analyze the data according to component molecular formulae. Assignments were internally recalibrated, and subjected to the following restrictions: CxHyOz, $0.3 \leq H/C \leq 3$, $0 \leq O/C \leq 2.5$, and a maximum allowable error $\leq 1$ ppm. The final peak list that represents each sample is composed of molecular formulae that are common across the three injections. The number of molecular assignments was 1014 for *n*-pentane first-stage POA, 1525 for *n*-heptane first-stage POA, 206 for the cold-start spark-ignition engine POA, and 185 for the PCCI engine POA. The *n*-pentane second-stage POA and CDC POA had no signal.

### 3.2.6. POA chemical analysis using nanospray desorption electrospray ionization mass spectrometry

In addition to ESI-FTIRC-MS, the *n*-heptane first-stage POA was also analyzed at the Pacific Northwest National Laboratory (PNNL) Environmental Molecular Sciences Laboratory (EMSL) using nanospray desorption electrospray ionization (nano-DESI) high resolution mass spectrometry. The design of the nano-DESI high resolution mass spectrometry (HRMS) interface has been previously described in (Vandergrift, Kew, et al., 2022; Vandergrift, Shawon, et al.,

2022). Briefly, a 7/3 v/v acetonitrile/water solvent mixture (Optima LC-MS grade; Fisher Chemical, Hampton USA) was flowed at 0.5 µL/min through a capillary assembly formed by two fused silica capillaries aligned at ~90° (Polymicro Technologies, Phoenix, USA; primary capillary: 150 µm O.D., 50 µm I.D.; secondary capillary: 150 µm O.D., 20 µm I.D. with etched terminus (Kelly et al., 2006)). This junction was brought sufficiently close to the PTFE filter samples such that a liquid junction formed and scanned along the XY plane at 35 µm/s, allowing for continuous and direct sampling from the filters. -3.5 kV was applied via the solvent syringe needle, and the nano-DESI capillary assembly was positioned ~1 mm from the inlet of a high-resolution LTQ Velos Orbitrap mass spectrometer (Thermo Scientific, Waltham). The MS inlet was maintained at 275°C. All samples were analyzed in negative ion mode via MS1 (m/z 100 – 1000) with an automatic gain control (AGC) target of 5 x 105, maximum ion injection time of 500 ms, and mass resolution of 100k at m/z 400.

For data analysis, 100 scans were averaged per sample within Xcalibur (Thermo Scientific) and exported as a .csv peak list (5 decimal points per m/z). MFAssignR was used for component molecular formulae assignment. For features with S/N > 6, assignments were internally recalibrated, and subjected to the following restrictions: CxHyOz; $0.3 \leq H/C \leq 3$; $O/C \leq 2.5$; $-20 \leq DBE\text{-}O \leq 25$ (DBE-O: double bond equivalents minus oxygen count). Datasets were blank subtracted such that molecular formulae detected in both a solvent blank and sample list were removed from the final sample list if they were present in the sample at 3x or lower the level found in the blank. Final datasets were manually inspected/cleaned for outlier assignments (Vandergrift, Shawon, et al., 2022). The final peak list used in the interpretations for each sample is composed of only molecular formulae commonly detected across each of three replicates. The number of molecular assignments was 1895 for *n*-heptane first-stage POA.

### 3.2.7. Experimental methods for gas-phase speciation measurements using electron-impact mass spectrometry and vacuum ultraviolet absorption spectroscopy

Using a filtration system to remove particles, gas-phase samples were collected for offline analysis from the controlled combustion of *n*-pentane. In order to compare the temperature-dependent concentration profiles of gas-phase species emitted during first-stage combustion to that of first-stage POA, we collected gas-phase samples at five temperature points: 543 K, 563 K, 598 K, 658 K, and 743 K. The second-stage samples were collected at 1143 K. Gas-phase samples were compressed in an inert-coated chamber and then introduced into a valving system connected to a gas chromatograph (GC), which collects 500 μL of the sample. The 500-μL volume was then introduced via the GC to three different detectors. First, the sample was directed through a 5Å molecular-sieve which separates CO, $CO_2$, $H_2$, $O_2$, and $CH_4$, for analysis via a thermal conductivity detector (TCD) using Ar as reference gas. The filtered sample was then split into two volumes of 250 μL which are injected sequentially onto two identical PONA columns of 100 m length, 250 μm inner diameter, and 0.50 μm film thickness. The two columns follow the same temperature programming which begins with holding at 40 °C for 5 minutes, increasing to 110 °C at 5 °C/min, holding at 110 °C for 5 minutes, increasing to 280 °C at 5 °C/min, and holding at 280 °C for 5 minutes.

One PONA column leads to a 70-eV electron-impact mass-spectrophotometer (EI-MS), while the other leads to a vacuum-ultraviolet (VUV) absorption cell which is held at 50 °C and 795 ± 2 torr. Species quantification was achieved through fitting of measured absorption spectra to reference spectra at photon energies with high signal-to-noise ratios lying within the full-scale range of 5.17 – 9.92 eV. Example fitting ranges are shown in Figures S3.3-S3.11 (Appendix B) with the shaded region of the VUV spectra. Prior to quantification, reference spectra were

created from injection of reference gas samples, typically at 1000 ppm, and were also included in Figures S3.3-S3.11. VUV spectra without shaded regions are solely used for identification.

### 3.2.8. Gas-particle partitioning perturbation experiments

In order to assess the effect of oligomer dissociation on the evaporation behavior of first-stage POA (or oxygenated POA – OxyPOA), we subjected the OxyPOA emissions from *n*-pentane combustion to two perturbations: (i) dilution with clean air at room temperature, and (ii) heating in a thermodenuder at temperatures ranging between 303 K and 363 K. Both dilution and heating perturb the gas-particle equilibrium partitioning and force the particles to evaporate in order to reestablish equilibrium. If the particle phase contains oligomers, the perturbation induces not only physical evaporation (i.e. partitioning of molecules from the particle phase to the gas phase), but also oligomer dissociation (Trump & Donahue, 2014). The reason is that monomers evaporate more readily than the oligomers due to their smaller molecular size, thus higher volatility. This perturbs the monomer-oligomer equilibrium in the particle phase, leading to oligomer dissociation to reestablish equilibrium. Quantifying the equilibrium composition of monomers and oligomers is not straightforward. However, the dissociation rate constant is known to increase significantly more than the association rate constant with increase in temperature (Trump & Donahue, 2014). In other words, the monomer-oligomer equilibrium composition shifts toward higher fraction of monomers as temperature increases, making the aerosol more volatile because monomers are more volatile than oligomers. Consequently, the effect of oligomer dissociation would be more prominent if the aerosol is heated in a thermodenuder compared to dilution at room temperature. Here, we probe this temperature-dependent oligomer dissociation effect by comparing the apparent volatility of the OxyPOA, namely saturation concentration ($C_{sat}$), needed to explain the extent of evaporation in the dilution

versus thermodenuder perturbations. If higher $C_{sat}$ values are required to reproduce the observed evaporation in the thermodenuder measurements compared to dilution, this would be evidence that the OxyPOA contains oligomers.

In both the dilution and thermodenuder experiments, the combustion chamber temperature was set to 583 K, corresponding to the peak OxyPOA emissions (Fig. 3.2). The thermodenuder experiments involved diluting the combustion emissions (0.75 SLPM) with 12 SLPM of clean air and then alternating between measuring the baseline aerosol mass concentration at room temperature ($C_{OA,0}$) by sampling through the bypass and measuring the aerosol mass concentration ($C_{OA}$) at 303 K, 323 K, 343 K, and 363 K by sampling through the thermodenuder (Fig. 3.1). The thermodenuder consisted of a stainless-steel tube wrapped with heating tape and insulation. The temperature was controlled using a PID controller (OMEGA, CNi3244). The thermodenuder has a volume of 0.5 L (diameter = 2.54 cm, length = 1 m) and the aerosol flow was 1 SLPM, yielding an average residence time of 30 seconds. In the dilution experiments, we first obtained a baseline aerosol mass concentration ($C_{OA,0}$) by mixing the combustion emissions (0.75 SLPM) with 3 SLPM of clean air in the dilution chamber (Fig. 3.1). We then applied three dilution factors (DFs) of approximately 5, 8, and 10, and measured the aerosol mass concentration ($C_{OA}$) at each DF. The aerosol emissions in the dilution experiment were also sampled through the thermodenuder, but without heating, to allow for ample time for evaporation.

We performed gas-particle equilibrium calculations (Donahue et al., 2006) to interpret the observed OxyPOA evaporation at the dilution and thermodenuder experimental conditions. We first calculated the reference saturation concentration at 300 K ($C_{sat,ref}$) of the each of the

assigned molecules (see above for molecular assignments) based on the parameterization of Li *et al.* (Li et al., 2016):

$$\log_{10}(C_{\mathrm{sat,ref}}) = (n_{\mathrm{C}}^{0} - n_{\mathrm{C}})\, b_{\mathrm{C}} - n_{\mathrm{O}}\, b_{\mathrm{O}} - 2\,\frac{n_{\mathrm{C}}\, n_{\mathrm{O}}}{n_{\mathrm{C}} + n_{\mathrm{O}}}\, b_{\mathrm{CO}} \qquad (6)$$

Where, $n_{\mathrm{C}}$ is the number of carbon atoms, $n_{\mathrm{O}}$ is the number of oxygen atoms, $n_{\mathrm{C}}^{0} = 22.6$, $b_{\mathrm{C}} = 0.4481$, $b_{\mathrm{O}} = 1.656$, and $b_{\mathrm{CO}} = -0.779$.

The molecules were then grouped into five volatility bins that correspond to:

(1) Intermediate-volatility organic compounds (IVOCs): $C_{\mathrm{sat,ref}}$ > 300 μg/m$^3$.

(2) Semi-volatile organic compounds (SVOCs): 0.3 μg/m$^3$ < $C_{\mathrm{sat,ref}}$ > 300 μg/m$^3$.

(3) Low-volatility organic compounds (LVOCs): 3 x 10$^{-4}$ μg/m$^3$ < $C_{\mathrm{sat,ref}}$ > 0.3 μg/m$^3$.

(4) Extremely low volatility organic compounds (ELVOCs): 3 x 10$^{-9}$ μg/m$^3$ < $C_{\mathrm{sat,ref}}$ > 3 x 10$^{-4}$ μg/m$^3$.

(5) Ultra-low volatility organic compounds (ULVOCs): $C_{\mathrm{sat,ref}}$ < 3 x 10$^{-9}$ μg/m$^3$

We then assigned $C_{\mathrm{sat,ref}}$ value for each bin, calculated as the average $C_{\mathrm{sat,ref}}$ of the components in the bin. We calculated $C_{\mathrm{sat}}$ values at different temperatures ($C_{\mathrm{sat}}$(T)) using the Clausius-Clapeyron relation:

$$C_{\mathrm{sat}}(T) = C_{\mathrm{sat,ref}}\,\frac{T_{\mathrm{ref}}}{T}\,\exp\left(\frac{-\Delta H}{R}\left(\frac{1}{T} - \frac{1}{T_{\mathrm{ref}}}\right)\right) \qquad (7)$$

Where, $T_{\mathrm{ref}}$ is the reference temperature (300 K), $R$ is the universal gas constant, and $\Delta H$ is the enthalpy of vaporization, estimated using the parameterization of Epstein *et al.* (Epstein et al., 2010):

$$\Delta H\ [\mathrm{kJ/mol}] = -11\log_{10}(C_{\mathrm{sat,ref}}) + 129 \qquad (8)$$

We then employed an iterative solution to calculate $C_{\mathrm{OA}}$ at each experimental condition (for both dilution and thermodenuder experiments) following Donahue *et al*. (Donahue et al., 2006):

$$z_i = \left(1 + \frac{C_{sat,i}}{C_{OA}}\right)^{-1};\ C_{OA} = \sum_i C_i\ z_i \quad (9)$$

Where, the subscript 'i' refers to a specific volatility bin, *z* is the portioning coefficient between the particle phase and the gas phase, and C is the total concentration in both phases.

The equilibrium-partitioning $C_{OA}$ values calculated using the volatility distribution obtained from molecular assignments correspond to the black lines in Fig. 4A and 4C in the main text. We also obtained a volatility distribution that yields equilibrium-partitioning $C_{OA}$ values that fit the thermodenuder measurements by adjusting the mass fractions in the volatility bins. These equilibrium-partitioning $C_{OA}$ values correspond to the brown lines in Fig. 4A and 4C in the main text.

### 3.3. Results and discussion

#### 3.3.1. Difference in POA emitted from first-stage and second-stage ignition

Figure 3.3 shows results from chemical analysis of POA emitted from the controlled combustion of *n*-pentane and *n*-heptane. We distinguish between 'first-stage POA,' which formed at relatively low temperatures (550 K – 650 K) where reactions of peroxy radicals ($RO_2$) dominate, and 'second-stage POA,' which formed at relatively high temperatures (> 1100 K) (Fig. 3.2). Traditionally, only second-stage POA has been thought to constitute POA emissions from the combustion of hydrocarbon fuels, whereas first-stage POA was only recently discovered (El Hajj et al., 2021). Therefore, it is imperative to set the appropriate context for the results. Second-stage POA forms at relatively high temperatures (> 1000 K) and is equivalent to 'incipient soot' in combustion science terminology (Michelsen, 2017). It is comprised of polycyclic aromatic hydrocarbons (PAHs) and aliphatic species (Johansson et al., 2018) and therefore falls strictly under HOA (Jimenez et al., 2009). With further increase in temperature, the organic molecules that comprise second-stage POA transform into mature soot (Michelsen, 2017), which is largely

equivalent to black carbon (BC) in atmospheric science terminology (Bond et al., 2013). BC is a strong light-absorber and a leading contributor to climate warming (Bond et al., 2013). Second-stage POA can also be light-absorbing and is categorized as brown carbon (BrC) (Saleh et al., 2018). For these reasons, the formation and physicochemical properties of second-stage POA have been extensively studied by both combustion scientists and atmospheric scientists (El Hajj et al., 2021; Faccinetto et al., 2015; Johansson et al., 2018; Saleh et al., 2018).

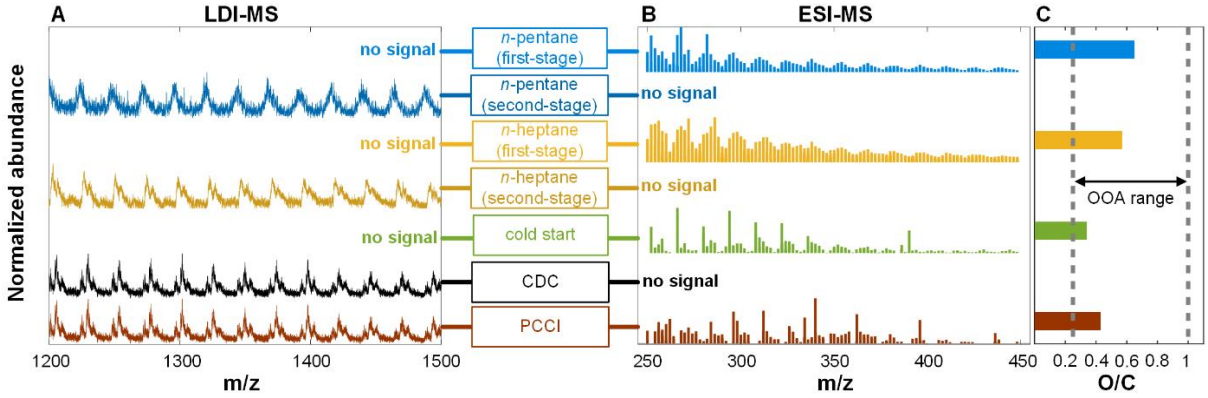


**Figure 3.3.** Mass spectrometry analysis of POA emissions from controlled combustion of n-pentane and n-heptane, a spark-ignition engine operated at simulated cold-start conditions, and a compression-ignition engine operated at steady-state conditions using either conventional diesel combustion (CDC) strategy or an advanced compression-ignition (ACI) strategy (premixed charge compression ignition – PCCI). The temperature of the n-pentane and n-heptane combustion was controlled to emit either first-stage POA (550 K – 650 K) or second-stage POA (1100 K – 1300 K) (see supplementary materials). (A) Mass spectra obtained using LDI-MS. (B) Mass spectra obtained using ESI-MS. (C) Average O/C of the molecules detected by ESI-MS. The n-heptane first-stage POA was also analyzed using high resolution nanospray desorption electrospray ionization (nano-DESI) mass spectrometry, which yielded mass spectra and average O/C (0.57) consistent with ESI-MS (fig. S3.11).

Some hydrocarbon fuels, including *n*-pentane and *n*-heptane, exhibit two-stage ignition behavior (Ju, 2021; H. Zhao et al., 2018), with first-stage ignition occurring at relatively low temperatures (550 K – 750 K). Discovery of first-stage ignition in the mid-twentieth century was motivated by efforts to understand the cause of engine knock in spark-ignition engines (Westbrook et al., 2018; Wheeler et al., 1948). Furthermore, the importance of first-stage ignition in advanced

compression-ignition (ACI) engines that rely on low-temperature combustion (LTC) remains an impetus for unveiling chemical kinetics of $RO_2$. As part of a complex degenerate chain-branching mechanism, $RO_2$ isomerization to (carbon-centered) QOOH radicals and subsequent reactions are the focal points for understanding chain-branching reactions in combustion (Rotavera & Taatjes, 2021; Zádor et al., 2011). However, while the dynamics of two-stage ignition chemistry is known to rely on QOOH-mediated reactions below 1000 K, the concomitant production of organic molecules with volatilities low enough to condense and form OA (i.e. first-stage POA) has only recently been reported (El Hajj et al., 2021). The second-stage POA generated in our experiments was detected by laser desorption ionization mass spectrometry (LDI-MS) and exhibited major peaks separated by 24 u, which are characteristic signatures of PAHs (Michela et al., 2008) (Fig. 3.3). Being non-polar, the second-stage POA molecules were not efficiently ionized by electrospray ionization (ESI) and were thus not detected by ultra-high resolution ESI mass spectrometry (ESI-MS). Conversely, the first-stage POA was transparent to LDI-MS but was detected by ESI-MS, indicating that the first-stage POA did not include PAHs and was comprised of polar compounds that were efficiently ionized by ESI. The first-stage POA had an average O/C of 0.65 and 0.56 for *n*-pentane and *n*-heptane, respectively, and thus falls under OOA, a category previously reserved for SOA (Canagaratna et al., 2015; Jimenez et al., 2009; Mahrt et al., 2021). Furthermore, ESI-MS spectra show repetitive clusters of peaks separated by 14 u, which is indicative of oligomer formation (Kalberer et al., 2004), another feature usually associated with SOA (Hall IV & Johnston, 2012; Maben & Ziemann, 2023; Tolocka et al., 2004) and is further explored in the subsequent section.

These results demonstrate a marked difference in chemical characteristics between first-stage POA and traditional hydrocarbon-combustion POA (i.e., second-stage POA), which necessitates

distinction between the two. To facilitate use within the context of atmospheric chemistry, we introduce the term 'oxygenated POA' (OxyPOA) to refer to first-stage POA. OxyPOA communicates the most distinct aspect of first-stage POA, namely high O/C, and maintains the same general terminological character used to describe organic aerosol in atmospheric chemistry literature (POA, SOA, HOA, OOA, etc.). We note that OxyPOA is different from oxidized POA (OPOA), a term used to refer to aged POA that has undergone heterogeneous oxidation in the atmosphere (Budisulistiorini et al., 2021; Shrivastava et al., 2008). We also note that even though first-stage POA, or OxyPOA, is essentially organic particulate combustion emissions, it does not form through the high-temperature soot-formation route (Frenklach & Wang, 1991) and therefore should not be subsumed under the term 'incipient soot' (Michelsen, 2017).

### 3.3.2. Formation pathways of OxyPOA

Collisionally stabilized alkylperoxy radicals ($RO_2$) traverse unimolecular reactions on potential energy surfaces that include isomerization to carbon-centered QOOH radicals and concerted elimination of $HO_2$. The former type of reaction is central to chain-branching and can also produce cyclic ether species, as in Fig. 3.4, in which 2-pentyl undergoes reaction with $O_2$ to ultimately form 2-methyltetrahydrofuran, which is one of several isomers formed during *n*-pentane oxidation (Bugler et al., 2017). Similar to alkyl radicals, cyclic ethers also undergo complex reactions with $O_2$ (Christianson et al., 2021; Doner et al., 2021; Doner et al., 2022). In addition to unimolecular reactions, however, $RO_2$ radicals can undergo bimolecular reactions including with other $RO_2$ radicals (Koritzke et al., 2023). Fig. 3.4 depicts, as an example, a set of reactions of 2-methyltetrahydrofuran that produce highly oxidized, multi-functional intermediates in sequential steps mediated by organic hydroperoxides (ROOH), which result in species of decreased volatility that can partition to the particle phase and contribute to OxyPOA formation.

2-Methyltetrahydrofuran ($C_5H_{10}O$) and 2-methyltetrahydrofuran-3-one ($C_5H_8O_2$) were detected in the gas phase emissions of first-stage *n*-pentane combustion. Both species had temperature-dependent concentration profiles that exhibited similar trends to that of OxyPOA (fig. S3.10), signifying their role as OxyPOA precursors. As illustrated in Fig. 3.4, 2-methyltetrahydrofuran-3-one can undergo two additional oxygen-addition steps leading to the formation of $C_5H_6O_3$ molecules (2-methylfuran-3,4(2*H*,5*H*)-dione and 3-oxotetrahydrofuran-2-carbaldehyde), and ultimately $C_4H_4O_4$ molecules (5-methylfuran-2,3,4(5*H*)-trione and 3,4-dioxotetrahydrofuran-2-carbaldehyde). The intermediate $C_5H_6O_3$ molecules were not detected in the gas phase, which is ascribed to their existence at concentrations below the detection limit of our gas-phase instruments. Furthermore, their volatility is appreciably high such that partitioning to the particle phase is precluded (fig. S3.12). The $C_4H_4O_4$ molecules, however, have volatilities low enough to partition to the particle phase. The *n*-pentane OxyPOA species detected by ESI-MS included a peak at m/z 128.011 that reflects a molecular formula $C_5H_4O_4$, which coincided with 5-methylfuran-2,3,4(5*H*)-trione and 3,4-dioxotetrahydrofuran-2-carbaldehyde in Fig. 3.4.

Other pathways to multi-functional species include the formation of dicarbonyls via oxidation of the tertiary radical of *syn*-2,4-dimethyloxetane, another cyclic ether derived from *n*-pentane (Doner et al., 2022). Fig. S3.13 illustrates the formation of 2,4-pentanedione ($C_5H_8O_2$) (detected in the gas phase of first-stage *n*-pentane combustion), which undergoes further oxidation to form 2,3,4-trioxopentanal and 2,4-dioxopentanedial. Both species have molecular formula $C_5H_4O_4$, which coincided with the m/z 128.011 peak detected in the particle phase.

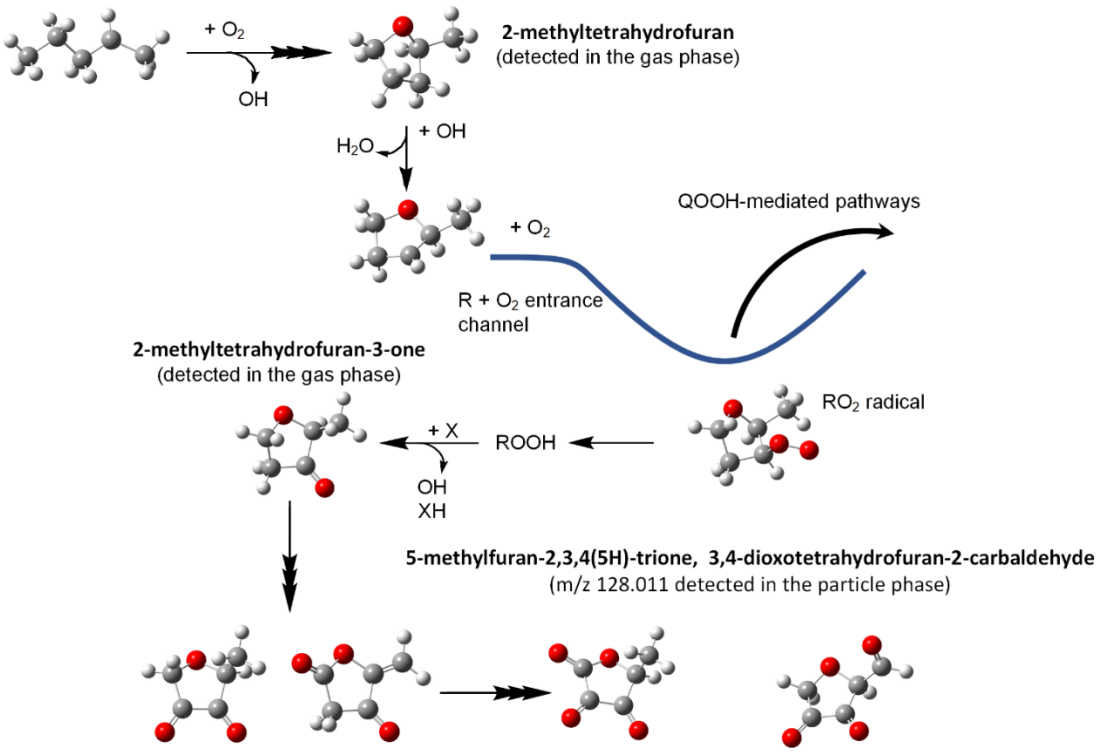


**Figure 3.4.** Pathway for OxyPOA formation from gas-phase precursors produced during first-stage combustion of *n*-pentane. Oxidation of 2-pentyl produces 2-methyltetrahydrofuran, a cyclic ether, via a QOOH-mediated reaction. Subsequent H-abstraction and $O_2$-addition produces cyclic ether peroxy radicals ($RO_2$), such as 2-methyl-tetrahydrofuranyl-3-peroxy, which can undergo additional QOOH-mediated reactions or act as a hydrogen abstractor to produce ROOH. Abstraction of tertiary hydrogen from ROOH and barrierless O–O scission of the resultant carbon-centered radical, carbonyl-substituted species are produced coincident with OH in a chain-propagating step (Koritzke et al., 2023). Subsequent oxidation of species such as 2-methyl-tetrahydrofuran-3-one yields condensable species that form OxyPOA. The $RO_2$ well-depth, shown arbitrarily submerged, is typically 35 kcal/mol exothermic relative to the R + $O_2$ entrance channel.

Supported by species detected in the gas phase and particle phase of the *n*-pentane first-stage combustion emissions, the schemes in Fig. 3.4 and fig. S3.13 provide viable pathways for OxyPOA formation from gas-phase precursors. However, this alone cannot explain the large molecular sizes observed in the mass spectra of OxyPOA species (Fig. 3.3 and fig. S3.11). Limited by the scarcity of small hydrocarbon radicals at LTC conditions, such as vinyl and propargyl, it is unlikely for gas-phase reactions to produce species with carbon numbers larger than that of the parent hydrocarbon. We hypothesize that the critical final step in OxyPOA formation is molecular growth

by oligomerization. Formation of oligomers not only renders the molecules in the particle phase less volatile, but also provides a condensation sink for more monomers to condense and oligomerize, thus creating a feedback mechanism that promotes condensational particle growth. We provide two levels of evidence for the prevalence of oligomers in OxyPOA: (i) patterns in the ESI-MS spectra, and (ii) response to perturbation in gas-particle equilibrium partitioning.

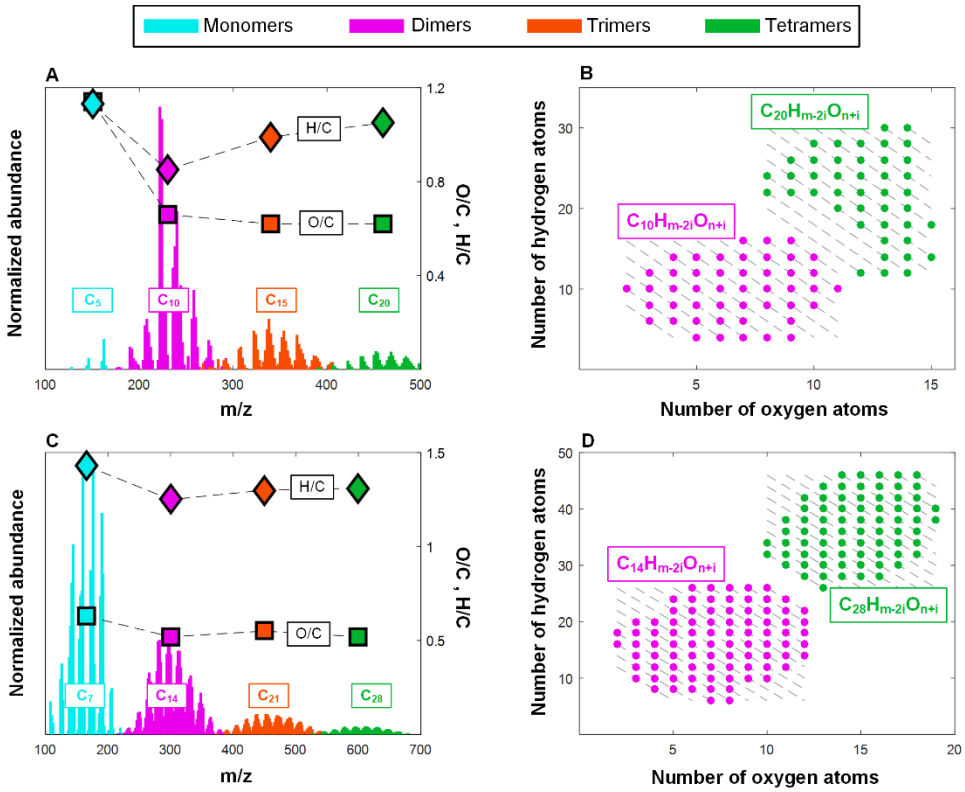


**Figure 3.5.** Evidence for oligomer formation from ESI-MS analysis. (**A** and **C**) ESI-MS spectra of OxyPOA in *n*-pentane and *n*-heptane combustion that isolate $C_5$ monomers (*n*-pentane, **A**) and $C_7$ monomers (*n*-heptane, **C**) and oligomers with carbon numbers that are multiples of 5 and 7, respectively. Also shown are the average H/C and O/C of the monomers and the oligomers. (**B** and **D**) Number of hydrogen atoms versus number of oxygen atoms of the dimers and tetramers. (**B**) All the dimers and tetramers in the *n*-pentane OxyPOA belong to families with the general formula $C_{10}H_{m-2i}O_{n+i}$ and $C_{20}H_{m-2i}O_{n+i}$ (dashed gray lines), respectively. (**D**) All the dimers and tetramers in the *n*-heptane OxyPOA belong to families with the general formula $C_{14}H_{m-2i}O_{n+i}$ and $C_{28}H_{m-2i}O_{n+i}$ (dashed gray lines), respectively. Results consistent with those in panels **C** and **D** for *n*-heptane were obtained using nano-DESI mass spectrometry (fig. S3.11).

Mass spectra of oligomers previously observed in SOA are characterized by broad groupings, with each grouping comprised of clusters of equidistant peaks (Tolocka et al., 2004). Due to the high

diversity of monomer combinations, the broad groupings are not apparent in the OxyPOA ESI-MS spectra (Fig. 3.3) but can be observed by isolating monomers with a certain carbon number. Representative results are shown in Fig. 3.5 for $C_5$ (*n*-pentane) and $C_7$ (*n*-heptane) monomers and oligomers with carbon numbers that are multiples of 5 and 7, respectively. These monomers form via first-stage functionalization pathways over which the hydrocarbon backbone remains intact during oxidation, resulting in $C_5$ (for *n*-pentane combustion) and $C_7$ (for *n*-heptane combustion) molecules with diverse functionality, including carbonyls and cyclic ethers, which are common among alkane oxidation (Belhadj et al., 2021; Hartness et al., 2022). Isolating molecules with carbon numbers $C_{5c}$ and $C_{7c}$ (c = 1, 2, 3, 4) in the ESI-MS spectra of the *n*-pentane OxyPOA (Fig. 3.5A) and *n*-heptane OxyPOA (Fig. 3.5C) reveals oligomer signatures similar to those previously reported for SOA (Tolocka et al., 2004). Oligomer formation is further evidenced by the relatively small change in H/C and O/C with increasing carbon number, which is consistent with growth by monomer association. One exception is noted for the O/C of the $C_5$ monomers in *n*-pentane OxyPOA being significantly larger than the oligomers. This can be explained as follows: because of the small carbon number, only the highly functionalized $C_5$ monomers with high O/C have volatilities low enough (Donahue et al., 2011) to partition to the particle phase, resulting in the O/C of the $C_5$ monomers in the OxyPOA sample being skewed high.

The broad groupings of $C_{5c}$ and $C_{7c}$ oligomers exhibit sequences of smaller clusters separated by 14 u. This suggests dominant formation pathways of monomers that include sequential steps with the net result of abstracting two hydrogen atoms and adding one oxygen atom (Fig. 3.4). Various combinations of these $C_5$ and $C_7$ monomers lead to the formation of oligomers with general formulae $C_{5c}H_{m-2i}O_{n+i}$ and $C_{7c}H_{m-2i}O_{n+i}$ (i = 1, 2, 3,…).

This is illustrated in Fig. 3.5B and Fig. 3.5D, which show that all the dimers and tetramers belong to, respectively, $C_{5c}H_{m-2i}O_{n+i}$ and $C_{7c}H_{m-2i}O_{n+i}$ families (c = 2,4). The various combinations of monomers (with varying carbon numbers) that form through similar hydrogen-abstraction and oxygen-addition pathways manifest as tightly packed oligomer structures separated by 14 u (Fig. 3.3).

To further confirm the role of oligomerization in OxyPOA formation, we examined the response of *n*-pentane OxyPOA to either dilution with clean air or heating in a thermodenuder. In the absence of oligomers, the extent of evaporation in response to both perturbations would be dictated by internally consistent thermodynamic properties (volatility distribution) of the aerosol components. The presence of oligomers, however, leads to an evaporation response that is limited by the rate of oligomer dissociation, which increases significantly with increasing temperature (Trump & Donahue, 2014). This would manifest as an apparent thermodynamic inconsistency in the aerosol response to the two perturbations: the aerosol would appear more volatile in the thermodenuder perturbation compared to dilution.

The dilution perturbation led to minimal evaporation (Fig. 3.6C), in agreement with equilibrium partitioning calculations using volatility distribution estimated from ESI-MS molecular assignments (Li et al., 2016). This indicates that the estimated volatility distribution, while not meant to be exact, predicted reasonably well the fraction of species that measurably partitioned to the gas phase in response to dilution (intermediate-volatility and semi-volatile compounds). However, equilibrium partitioning calculations using the same volatility distribution severely underestimated the extent of evaporation in the thermodenuder (Fig. 3.6A). Reproducing the OxyPOA response to the thermodenuder perturbation required substantially shifting the volatility distribution toward higher-volatility components, which would overestimate the extent of

evaporation in response to dilution. As we argue above, this seeming thermodynamic inconsistency indicates a prominent role of oligomer dissociation (Trump & Donahue, 2014).

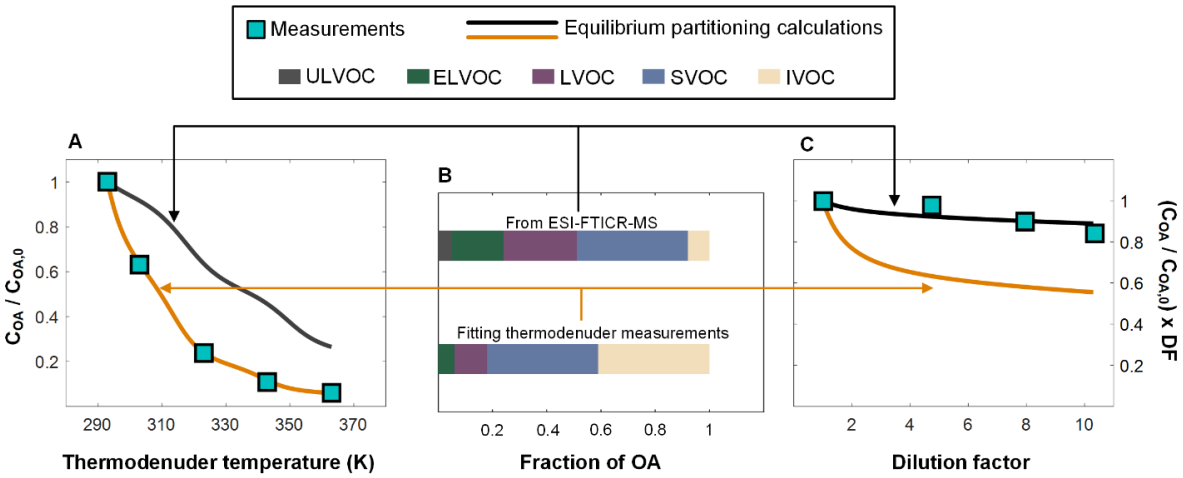


**Figure 3.6.** Evidence for presence of oligomers in OxyPOA from comparing evaporation measurements of *n*-pentane OxyPOA to equilibrium partitioning calculations. (**A**) Thermodenuder measurements showing the aerosol mass concentration at each temperature ($C_{OA}$) relative to the aerosol mass concentration at the reference temperature ($C_{OA,0}$). Also shown are equilibrium partitioning calculations using volatility distribution obtained from ESI-MS molecular assignments (black line). The brown line corresponds to equilibrium partitioning calculations using a volatility distribution adjusted to reproduce the measurements. (**B**) Volatility distributions obtained from ESI-MS molecular assignments (top bar) and adjusted to reproduce the thermodenuder measurements (bottom bar). The aerosol components are apportioned into intermediate-volatility (IVOC), semi-volatile (SVOC), low-volatility (LVOC), extremely low-volatility (ELVOC), and ultra-low-volatility (ULVOC) organic compounds. (**C**) Dilution measurements showing $C_{OA}$ at a certain dilution factor (DF) relative to no dilution ($C_{OA,0}$). Dilution leads to a decrease in $C_{OA}$ because of dilution itself as well as evaporation. To isolate the effect of evaporation, the y-axis is scaled by DF, such that the case of no evaporation would show as a horizontal line with a value of 1. Also shown are equilibrium partitioning calculations using volatility distribution obtained from ESI-MS molecular assignments (black line) and volatility distribution adjusted to reproduce the thermodenuder measurements (brown line).

### 3.4. Conclusions

We performed LDI-MS and ESI-MS analysis on POA samples collected from the emissions of a spark-ignition (gasoline) engine operated at a simulated cold-start condition and a compression-ignition (diesel) engine operated at steady state conditions using either conventional diesel

combustion (CDC) strategy or an ACI strategy (premixed charge compression ignition – PCCI). As shown in Fig. 3.3, the cold-start POA was transparent to LDI-MS but was detected by ESI-MS and exhibited repetitive peaks separated by 14 u with an average O/C within the OOA range. These results indicate that the POA from the simulated cold-start emissions was dominated by OxyPOA. The majority of POA emissions from on-road gasoline vehicles occur during cold-start conditions (Gentner et al., 2017), which are especially important in urban settings where a large share of driving consists of short trips at cold engine conditions (Reiter & Kockelman, 2016). Therefore, we expect OxyPOA to be ubiquitous in urban atmospheres.

These results help solve a long-standing mystery associated with air-quality models persistently predicting lower POA/SOA in urban atmospheres compared to observations (Akherati et al., 2019; Cappa et al., 2016; Docherty et al., 2008; Reiter & Kockelman, 2016; Tsimpidi et al., 2010). This discrepancy has been attributed to either missing (unquantified) SOA precursors or underestimation of SOA yields in emissions of mobile sources (Ensberg et al., 2014; Gentner et al., 2017). We provide an alternative explanation. Ambient measurements equate POA from mobile sources to HOA and SOA to OOA. However, our results suggest that the majority of urban POA emitted from gasoline vehicles (during cold-start) is OxyPOA, which would be counted as OOA and misattributed to SOA in ambient measurements.

Both CDC and PCCI emitted POA with typical soot-formation signatures identified by LDI-MS, signifying the presence of second-stage POA (Fig. 3.3). ESI-MS detected species in the PCCI POA but not the CDC POA. Similar to the cold-start POA, the PCCI POA species measured by ESI-MS had O/C within the OOA range and the spectra exhibited repetitive peaks, albeit not as prominent as the cold-start POA possibly due to the lower signal. These results suggest that the lower global in-cylinder temperatures in PCCI compared to CDC (Agarwal et al., 2017) resulted

in a portion of the emissions experiencing temperature histories (550 K – 750 K) conducive to the formation of first-stage POA (OxyPOA). Previous studies have reported significant increase in emissions of POA relative to mature soot for various ACI strategies (Lucachick et al., 2016; Moses-DeBusk et al., 2019). Our results indicate that a fraction of this POA is OxyPOA, which would lead to a relative increase in OOA in future urban atmospheres if these next-generation ACI strategies are widely adopted. Understanding the emission profiles of these ACI strategies aids in the development of clean, sustainable transportation energy technologies (Kohse-Höinghaus, 2023).

**Acknowledgments**

The CDC and PCCI samples were collected as part of the Co-Optimization of Fuels & Engines (Co-Optima) project sponsored by the U.S. DOE Office of Energy Efficiency and Renewable Energy, Office of Bioenergy Technologies, and Office of Vehicle Technologies. The cold-start samples were collected as part of the Partnership to Advance Combustion Engines Consortium sponsored by the U.S. DOE Office of Vehicle Technologies. We thank Kevin Stork, Mike Weismiller and Gurpreet Singh for support of this work, and Shean Huff and Scott Sluder for operating the diesel engine. We thank the University of Georgia Proteomics and Mass Spectrometry Core Facility for performing the LDI-MS and ESI-MS analyses.

**Funding**

National Science Foundation, Combustion and Fire Systems Program within the Division of Chemical, Bioengineering, Environmental, and Transport Systems under award CBET-2125064 (R.S., B.R.).

Gas-Phase Chemical Physics program within the Division of Chemical Sciences, Geosciences and Biosciences, Office of Basic Energy Sciences (BES), U.S. Department of Energy under award DE-SC0021337 (B.R.).

U.S. DOE Office of Science User Facility sponsored by the Biological and Environmental Research program under Contract No. DE-AC05-76RL01830 (G.W.V., Z.C., S.C.).

National Institutes of Health award S10OD025118.

## References


Agarwal, A. K., Singh, A. P., & Maurya, R. K. (2017). Evolution, challenges and path forward for low temperature combustion engines. *Progress in Energy and Combustion Science*, *61*, 1-56.

Akherati, A., Cappa, C. D., Kleeman, M. J., Docherty, K. S., Jimenez, J. L., Griffith, S. M., Dusanter, S., Stevens, P. S., & Jathar, S. H. (2019). Simulating secondary organic aerosol in a regional air quality model using the statistical oxidation model–Part 3: Assessing the influence of semi-volatile and intermediate-volatility organic compounds and NO x. *Atmospheric Chemistry and Physics*, *19*(7), 4561-4594.

Apicella, B., Carpentieri, A., Alfè, M., Barbella, R., Tregrossi, A., Pucci, P., & Ciajolo, A. (2007). Mass spectrometric analysis of large PAH in a fuel-rich ethylene flame. *Proceedings of the Combustion Institute*, *31*(1), 547-553.

Apicella, B., Russo, C., Carpentieri, A., Tregrossi, A., & Ciajolo, A. (2022). PAHs and fullerenes as structural and compositional motifs tracing and distinguishing organic carbon from soot. *Fuel*, *309*, 122356.

Atwi, K., Mondal, A., Pant, J., Cheng, Z., El Hajj, O., Ijeli, I., Handa, H., & Saleh, R. Physicochemical properties and cytotoxicity of brown carbon produced under different combustion conditions. *Atmospheric Environment*, *244*, 117881.

Atwi, K., Mondal, A., Pant, J., Cheng, Z., El Hajj, O., Ijeli, I., Handa, H., & Saleh, R. (2021). Physicochemical properties and cytotoxicity of brown carbon produced under different combustion conditions. *Atmospheric Environment*, *244*, 117881.

Bateman, A. P., Laskin, J., Laskin, A., & Nizkorodov, S. A. (2012). Applications of high-resolution electrospray ionization mass spectrometry to measurements of average oxygen to carbon ratios in secondary organic aerosols. *Environmental science & technology*, *46*(15), 8315-8324.

Bateman, A. P., Nizkorodov, S. A., Laskin, J., & Laskin, A. (2010). High-resolution electrospray ionization mass spectrometry analysis of water-soluble organic aerosols collected with a particle into liquid sampler. *Analytical Chemistry*, *82*(19), 8010-8016.

Bateman, A. P., Walser, M. L., Desyaterik, Y., Laskin, J., Laskin, A., & Nizkorodov, S. A. (2008). The effect of solvent on the analysis of secondary organic aerosol using electrospray ionization mass spectrometry. *Environmental science & technology*, *42*(19), 7341-7346.

Belhadj, N., Lailliau, M., Benoit, R., & Dagaut, P. (2021). Experimental and kinetic modeling study of n-hexane oxidation. Detection of complex low-temperature products using high-resolution mass spectrometry. *Combustion and Flame*, *233*, 111581.

Bond, T. C., Doherty, S. J., Fahey, D. W., Forster, P. M., Berntsen, T., DeAngelo, B. J., Flanner, M. G., Ghan, S., Kärcher, B., & Koch, D. (2013). Bounding the role of black carbon in the climate system: A scientific assessment. *Journal of Geophysical Research: Atmospheres*, *118*(11), 5380-5552.

Budisulistiorini, S. H., Chen, J., Itoh, M., & Kuwata, M. (2021). Can Online Aerosol Mass Spectrometry Analysis Classify Secondary Organic Aerosol (SOA) and Oxidized Primary Organic Aerosol (OPOA)? A Case Study of Laboratory and Field Studies of Indonesian Biomass Burning. *ACS Earth and Space Chemistry*, *5*(12), 3511-3522.

Budisulistiorini, S. H., Riva, M., Williams, M., Chen, J., Itoh, M., Surratt, J. D., & Kuwata, M. (2017). Light-absorbing brown carbon aerosol constituents from combustion of Indonesian peat and biomass. *Environmental science & technology*, *51*(8), 4415-4423.

Bugler, J., Rodriguez, A., Herbinet, O., Battin-Leclerc, F., Togbé, C., Dayma, G., Dagaut, P., & Curran, H. J. (2017). An experimental and modelling study of n-pentane oxidation in two jet-stirred reactors: The importance of pressure-dependent kinetics and new reaction pathways. *Proceedings of the Combustion Institute*, *36*(1), 441-448.

Canagaratna, M., Jimenez, J., Kroll, J., Chen, Q., Kessler, S., Massoli, P., Hildebrandt Ruiz, L., Fortner, E., Williams, L., & Wilson, K. (2015). Elemental ratio measurements of organic compounds using aerosol mass spectrometry: characterization, improved calibration, and implications. *Atmospheric Chemistry and Physics*, *15*(1), 253-272.

Cappa, C. D., Jathar, S. H., Kleeman, M. J., Docherty, K. S., Jimenez, J. L., Seinfeld, J. H., & Wexler, A. S. (2016). Simulating secondary organic aerosol in a regional air quality model using the statistical oxidation model–Part 2: Assessing the influence of vapor wall losses. *Atmospheric Chemistry and Physics*, *16*(5), 3041-3059.

Cheng, Y., He, K.-b., Du, Z.-y., Engling, G., Liu, J.-m., Ma, Y.-l., Zheng, M., & Weber, R. J. (2016). The characteristics of brown carbon aerosol during winter in Beijing. *Atmospheric Environment*, *127*, 355-364.

Cheng, Z., Atwi, K., Hajj, O. E., Ijeli, I., Fischer, D. A., Smith, G., & Saleh, R. (2020). Discrepancies between brown carbon light-absorption properties retrieved from online and offline measurements. *Aerosol Science and Technology*, 1-12.

Cheng, Z., Atwi, K., Onyima, T., & Saleh, R. (2019). Investigating the dependence of light-absorption properties of combustion carbonaceous aerosols on combustion conditions. *Aerosol Science and Technology*, *53*(4), 419-434.

Cheng, Z., Atwi, K. M., Yu, Z., Avery, A., Fortner, E. C., Williams, L., Majluf, F., Krechmer, J. E., Lambe, A. T., & Saleh, R. (2020). Evolution of the light-absorption properties of combustion brown carbon aerosols following reaction with nitrate radicals. *Aerosol Science and Technology*, *54*(7), 849-863. https://doi.org/10.1080/02786826.2020.1726867

Christianson, M. G., Doner, A. C., Davis, M. M., Koritzke, A. L., Turney, J. M., Schaefer III, H. F., Sheps, L., Osborn, D. L., Taatjes, C. A., & Rotavera, B. (2021). Reaction mechanisms of a cyclic ether intermediate: Ethyloxirane. *International Journal of Chemical Kinetics*, *53*(1), 43-59.

Curran, S., Szybist, J., Kaul, B., Easter, J., & Sluder, S. (2021). Fuel Stratification Effects on Gasoline Compression Ignition with a Regular-Grade Gasoline on a Single-Cylinder Medium-Duty Diesel Engine at Low Load. *SAE Technical Paper Series*, *2021*(01).

Docherty, K. S., Stone, E. A., Ulbrich, I. M., DeCarlo, P. F., Snyder, D. C., Schauer, J. J., Peltier, R. E., Weber, R. J., Murphy, S. M., & Seinfeld, J. H. (2008). Apportionment of primary and secondary organic aerosols in Southern California during the 2005 Study of Organic Aerosols in Riverside (SOAR-1). *Environmental science & technology*, *42*(20), 7655-7662.

Dockery, D. W., Pope, C. A., Xu, X., Spengler, J. D., Ware, J. H., Fay, M. E., Ferris Jr, B. G., & Speizer, F. E. (1993). An association between air pollution and mortality in six US cities. *New England journal of medicine*, *329*(24), 1753-1759.

Donahue, N. M., Epstein, S., Pandis, S. N., & Robinson, A. L. (2011). A two-dimensional volatility basis set: 1. organic-aerosol mixing thermodynamics. *Atmospheric Chemistry and Physics*, *11*(7), 3303-3318.

Donahue, N. M., Robinson, A., Stanier, C., & Pandis, S. (2006). Coupled partitioning, dilution, and chemical aging of semivolatile organics. *Environmental science & technology*, *40*(8), 2635-2643.

Doner, A. C., Davis, M. M., Koritzke, A. L., Christianson, M. G., Turney, J. M., Schaefer III, H. F., Sheps, L., Osborn, D. L., Taatjes, C. A., & Rotavera, B. (2021). Isomer-dependent reaction mechanisms of cyclic ether intermediates: cis-2, 3-dimethyloxirane and trans-2, 3-dimethyloxirane. *International Journal of Chemical Kinetics*, *53*(1), 127-145.

Doner, A. C., Zádor, J., & Rotavera, B. (2022). Stereoisomer-dependent unimolecular kinetics of 2, 4-dimethyloxetanyl peroxy radicals. *Faraday Discussions*, *238*, 295-319.

El Hajj, O., Atwi, K., Cheng, Z., Koritzke, A., Christianson, M., Dewey, N., Rotavera, B., & Saleh, R. (2021). Two-stage aerosol formation in low-temperature combustion. *Fuel*, *304*, 121322.

Ensberg, J., Hayes, P., Jimenez, J., Gilman, J., Kuster, W., De Gouw, J., Holloway, J., Gordon, T., Jathar, S., & Robinson, A. (2014). Emission factor ratios, SOA mass yields, and the impact of vehicular emissions on SOA formation. *Atmospheric Chemistry and Physics*, *14*(5), 2383-2397.

Epstein, S. A., Riipinen, I., & Donahue, N. M. (2010). A semiempirical correlation between enthalpy of vaporization and saturation concentration for organic aerosol. *Environmental science & technology*, *44*(2), 743-748.

Faccinetto, A., Desgroux, P., Ziskind, M., Therssen, E., & Focsa, C. (2011). High-sensitivity detection of polycyclic aromatic hydrocarbons adsorbed onto soot particles using laser desorption/laser ionization/time-of-flight mass spectrometry: An approach to studying the soot inception process in low-pressure flames. *Combustion and Flame*, *158*(2), 227-239.

Faccinetto, A., Focsa, C., Desgroux, P., & Ziskind, M. (2015). Progress toward the quantitative analysis of PAHs adsorbed on soot by laser desorption/laser ionization/time-of-flight mass spectrometry. *Environmental science & technology*, *49*(17), 10510-10520.

Frenklach, M., & Wang, H. (1991). Detailed modeling of soot particle nucleation and growth. Symposium (International) on Combustion,

Gentner, D. R., Jathar, S. H., Gordon, T. D., Bahreini, R., Day, D. A., El Haddad, I., Hayes, P. L., Pieber, S. M., Platt, S. M., & de Gouw, J. (2017). Review of urban secondary organic aerosol formation from gasoline and diesel motor vehicle emissions. *Environmental science & technology*, *51*(3), 1074-1093.

Hall IV, W. A., & Johnston, M. V. (2012). Oligomer formation pathways in secondary organic aerosol from MS and MS/MS measurements with high mass accuracy and resolving power. *Journal of the American Society for Mass Spectrometry*, *23*(6), 1097-1108.

Hansen, A. S., Bhagde, T., Moore III, K. B., Moberg, D. R., Jasper, A. W., Georgievskii, Y., Vansco, M. F., Klippenstein, S. J., & Lester, M. I. (2021). Watching a hydroperoxyalkyl radical (• QOOH) dissociate. *science*, *373*(6555), 679-682.

Hartness, S. W., Dewey, N. S., Christianson, M. G., Koritzke, A. L., Doner, A. C., Webb, A. R., & Rotavera, B. (2022). Probing O2 dependence of hydroperoxy-butyl reactions via isomer-resolved speciation. *Proceedings of the Combustion Institute*.

Jatana, G. S., Chuahy, F. D. F., & Szybist, J. (2021). The effect of spark-plug heat dispersal range and exhaust valve opening timing on cold-start emissions and cycle-to-cycle

variability. *SAE International Journal of Advances and Current Practices in Mobility*, *4*(2021-01-1180), 462-471.
Jatana, G. S., Chuahy, F. D. F., & Szybist, J. (2023). *Effect of Split-Injection Strategies on Engine Performance and Emissions under Cold-Start Operation* (0148-7191).
Jimenez, J. L., Canagaratna, M., Donahue, N., Prevot, A., Zhang, Q., Kroll, J. H., DeCarlo, P. F., Allan, J. D., Coe, H., & Ng, N. (2009). Evolution of organic aerosols in the atmosphere. *science*, *326*(5959), 1525-1529.
Johansson, K., Head-Gordon, M., Schrader, P., Wilson, K., & Michelsen, H. (2018). Resonance-stabilized hydrocarbon-radical chain reactions may explain soot inception and growth. *science*, *361*(6406), 997-1000.
Ju, Y. (2021). Understanding cool flames and warm flames. *Proceedings of the Combustion Institute*, *38*(1), 83-119.
Kalberer, M., Paulsen, D., Sax, M., Steinbacher, M., Dommen, J., Prévôt, A. S., Fisseha, R., Weingartner, E., Frankevich, V., & Zenobi, R. (2004). Identification of polymers as major components of atmospheric organic aerosols. *science*, *303*(5664), 1659-1662.
Kelly, R. T., Page, J. S., Luo, Q., Moore, R. J., Orton, D. J., Tang, K., & Smith, R. D. (2006). Chemically etched open tubular and monolithic emitters for nanoelectrospray ionization mass spectrometry. *Analytical Chemistry*, *78*(22), 7796-7801.
Kenseth, C. M., Hafeman, N. J., Huang, Y., Dalleska, N. F., Stoltz, B. M., & Seinfeld, J. H. (2020). Synthesis of carboxylic acid and dimer ester surrogates to constrain the abundance and distribution of molecular products in α-pinene and β-pinene secondary organic aerosol. *Environmental science & technology*, *54*(20), 12829-12839.
Kitanovski, Z., Grgić, I., Vermeylen, R., Claeys, M., & Maenhaut, W. (2012). Liquid chromatography tandem mass spectrometry method for characterization of monoaromatic nitro-compounds in atmospheric particulate matter. *Journal of Chromatography A*, *1268*, 35-43.
Kohse-Höinghaus, K. (2023). Combustion, Chemistry, and Carbon Neutrality. *Chemical Reviews*.
Koritzke, A. L., Dewey, N. S., Christianson, M. G., Hartness, S., Doner, A. C., Webb, A. R., & Rotavera, B. (2023). Probing O2-dependence of tetrahydrofuranyl reactions via isomer-resolved speciation. *Combustion and Flame*, 112640.
Li, Y., Pöschl, U., & Shiraiwa, M. (2016). Molecular corridors and parameterizations of volatility in the chemical evolution of organic aerosols. *Atmospheric Chemistry and Physics*, *16*(5), 3327-3344.
Lin, P., Aiona, P. K., Li, Y., Shiraiwa, M., Laskin, J., Nizkorodov, S. A., & Laskin, A. (2016). Molecular characterization of brown carbon in biomass burning aerosol particles. *Environmental science & technology*, *50*(21), 11815-11824.
Lin, P., Fleming, L. T., Nizkorodov, S. A., Laskin, J., & Laskin, A. (2018). Comprehensive molecular characterization of atmospheric brown carbon by high resolution mass spectrometry with electrospray and atmospheric pressure photoionization. *Analytical Chemistry*, *90*(21), 12493-12502.
Liu, J., Bergin, M., Guo, H., King, L., Kotra, N., Edgerton, E., & Weber, R. (2013). Size-resolved measurements of brown carbon in water and methanol extracts and estimates of their contribution to ambient fine-particle light absorption. *Atmospheric Chemistry and Physics*, *13*(24), 12389-12404.

Lucachick, G., Curran, S., Storey, J., Prikhodko, V., & Northrop, W. F. (2016). Volatility characterization of nanoparticles from single and dual-fuel low temperature combustion in compression ignition engines. *Aerosol Science and Technology*, *50*(5), 436-447.

Maben, H. K., & Ziemann, P. J. (2023). Kinetics of oligomer-forming reactions involving the major functional groups present in atmospheric secondary organic aerosol particles. *Environmental Science: Processes & Impacts*.

Mahrt, F., Newman, E., Huang, Y., Ammann, M., & Bertram, A. K. (2021). Phase Behavior of Hydrocarbon-like Primary Organic Aerosol and Secondary Organic Aerosol Proxies Based on Their Elemental Oxygen-to-Carbon Ratio. *Environmental science & technology*, *55*(18), 12202-12214.

McMurry, P. H., Wang, X., Park, K., & Ehara, K. (2002). The relationship between mass and mobility for atmospheric particles: A new technique for measuring particle density. *Aerosol Science & Technology*, *36*(2), 227-238.

Michela, A., Barbara, A., Antonio, T., & Anna, C. (2008). Identification of large polycyclic aromatic hydrocarbons in carbon particulates formed in a fuel-rich premixed ethylene flame. *Carbon*, *46*(15), 2059-2066.

Michelsen, H. (2017). Probing soot formation, chemical and physical evolution, and oxidation: A review of in situ diagnostic techniques and needs. *Proceedings of the Combustion Institute*, *36*(1), 717-735.

Moses-DeBusk, M., Curran, S. J., Lewis, S. A., Connatser, R. M., & Storey, J. M. (2019). Impacts of Air-Fuel Stratification in ACI Combustion on Particulate Matter and Gaseous Emissions. *Emission Control Science and Technology*, *5*(3), 225-237.

Pervin, T., Gerdtham, U.-G., & Lyttkens, C. H. (2008). Societal costs of air pollution-related health hazards: A review of methods and results. *Cost Effectiveness and Resource Allocation*, *6*(1), 1-22.

Pörtner, H.-O., Roberts, D. C., Poloczanska, E., Mintenbeck, K., Tignor, M., Alegría, A., Craig, M., Langsdorf, S., Löschke, S., & Möller, V. (2022). IPCC, 2022: Summary for policymakers.

Reiter, M. S., & Kockelman, K. M. (2016). The problem of cold starts: A closer look at mobile source emissions levels. *Transportation Research Part D: Transport and Environment*, *43*, 123-132.

Rotavera, B., & Taatjes, C. A. (2021). Influence of functional groups on low-temperature combustion chemistry of biofuels. *Progress in Energy and Combustion Science*, *86*, 100925.

Russo, C., Stanzione, F., Ciajolo, A., & Tregrossi, A. (2013). Study on the contribution of different molecular weight species to the absorption UV–Visible spectra of flame-formed carbon species. *Proceedings of the Combustion Institute*, *34*(2), 3661-3668.

Saleh, R., Cheng, Z., & Atwi, K. (2018). The brown–black continuum of light-absorbing combustion aerosols. *Environmental Science & Technology Letters*, *5*(8), 508-513.

Savee, J. D., Papajak, E., Rotavera, B., Huang, H., Eskola, A. J., Welz, O., Sheps, L., Taatjes, C. A., Zádor, J., & Osborn, D. L. (2015). Direct observation and kinetics of a hydroperoxyalkyl radical (QOOH). *science*, *347*(6222), 643-646.

Schum, S. K., Brown, L. E., & Mazzoleni, L. R. (2020). MFAssignR: Molecular formula assignment software for ultrahigh resolution mass spectrometry analysis of environmental complex mixtures. *Environmental Research*, *191*, 110114.

Shrivastava, M. K., Lane, T. E., Donahue, N. M., Pandis, S. N., & Robinson, A. L. (2008). Effects of gas particle partitioning and aging of primary emissions on urban and regional organic aerosol concentrations. *Journal of Geophysical Research: Atmospheres*, *113*(D18).

Taatjes, C. A., Welz, O., Eskola, A. J., Savee, J. D., Scheer, A. M., Shallcross, D. E., Rotavera, B., Lee, E. P., Dyke, J. M., & Mok, D. K. (2013). Direct measurements of conformer-dependent reactivity of the Criegee intermediate CH3CHOO. *science*, *340*(6129), 177-180.

Teich, M., van Pinxteren, D., Wang, M., Kecorius, S., Wang, Z., Müller, T., Močnik, G., & Herrmann, H. (2017). Contributions of nitrated aromatic compounds to the light absorption of water-soluble and particulate brown carbon in different atmospheric environments in Germany and China. *Atmospheric Chemistry and Physics*, *17*(3), 1653-1672.

Tolocka, M. P., Jang, M., Ginter, J. M., Cox, F. J., Kamens, R. M., & Johnston, M. V. (2004). Formation of oligomers in secondary organic aerosol. *Environmental science & technology*, *38*(5), 1428-1434.

Trump, E., & Donahue, N. (2014). Oligomer formation within secondary organic aerosols: equilibrium and dynamic considerations. *Atmospheric Chemistry and Physics*, *14*(7), 3691-3701.

Tsimpidi, A., Karydis, V., Zavala, M., Lei, W., Molina, L., Ulbrich, I., Jimenez, J., & Pandis, S. N. (2010). Evaluation of the volatility basis-set approach for the simulation of organic aerosol formation in the Mexico City metropolitan area. *Atmospheric Chemistry and Physics*, *10*(2), 525-546.

Ulbrich, I., Canagaratna, M., Zhang, Q., Worsnop, D., & Jimenez, J. (2009). Interpretation of organic components from Positive Matrix Factorization of aerosol mass spectrometric data. *Atmospheric Chemistry and Physics*, *9*(9), 2891-2918.

Vandergrift, G. W., Kew, W., Lukowski, J. K., Bhattacharjee, A., Liyu, A. V., Shank, E. A., Paša-Tolić, L., Prabhakaran, V., & Anderton, C. R. (2022). Imaging and direct sampling capabilities of nanospray desorption electrospray ionization with absorption-mode 21 Tesla Fourier transform ion cyclotron resonance mass spectrometry. *Analytical Chemistry*, *94*(8), 3629-3636.

Vandergrift, G. W., Shawon, A. S. M., Dexheimer, D. N., Zawadowicz, M. A., Mei, F., & China, S. (2022). Molecular Characterization of Organosulfate-Dominated Aerosols over Agricultural Fields from the Southern Great Plains by High-Resolution Mass Spectrometry. *ACS Earth and Space Chemistry*, *6*(7), 1733-1741.

Welz, O., Savee, J. D., Osborn, D. L., Vasu, S. S., Percival, C. J., Shallcross, D. E., & Taatjes, C. A. (2012). Direct kinetic measurements of Criegee intermediate (CH2OO) formed by reaction of CH2I with O2. *science*, *335*(6065), 204-207.

Westbrook, C. K., Mehl, M., Pitz, W. J., Kukkadapu, G., Wagnon, S., & Zhang, K. (2018). Multi-fuel surrogate chemical kinetic mechanisms for real world applications. *Physical Chemistry Chemical Physics*, *20*(16), 10588-10606.

Wheeler, R. W., Downs, D., & Walsh, A. D. (1948). 'Knock' in Internal Combustion Engines. *Nature*, *162*(4127), 893-894. https://doi.org/10.1038/162893a0

Zádor, J., Taatjes, C. A., & Fernandes, R. X. (2011). Kinetics of elementary reactions in low-temperature autoignition chemistry. *Progress in Energy and Combustion Science*, *37*(4), 371-421.

Zhang, Q., Jimenez, J. L., Canagaratna, M., Allan, J. D., Coe, H., Ulbrich, I., Alfarra, M., Takami, A., Middlebrook, A., & Sun, Y. (2007). Ubiquity and dominance of oxygenated species in organic aerosols in anthropogenically-influenced Northern Hemisphere midlatitudes. *Geophysical research letters*, *34*(13).

Zhao, H., Wu, L., Patrick, C., Zhang, Z., Rezgui, Y., Yang, X., Wysocki, G., & Ju, Y. (2018). Studies of low temperature oxidation of n-pentane with nitric oxide addition in a jet stirred reactor. *Combustion and Flame*, *197*, 78-87.

Zhao, R., Kenseth, C. M., Huang, Y., Dalleska, N. F., & Seinfeld, J. H. (2018). Iodometry-assisted liquid chromatography electrospray ionization mass spectrometry for analysis of organic peroxides: An application to atmospheric secondary organic aerosol. *Environmental science & technology*, *52*(4), 2108-2117.

# CHAPTER 4

# EFFECTS OF FUEL ADDITIVES ON FIRST-STAGE ORGANIC AEROSOL [3]

[3] El Hajj, O., Glenn, C.K., Saleh, R. To be submitted to *Energy and Fuels*

**Abstract**

The use of fuel additives is a simple and effective strategy to extend the narrow operating range of advanced compression ignition (ACI) engines that rely on low temperature combustion (LTC) to increase thermal efficiency and reduce pollutant formation. Additives provide better control over combustion phasing by inhibiting radicals during LTHR which delay autoignition and increasing the octane number. In previous chapters, we provided evidence on the formation of first-stage OA from a two-stage ignition fuel formed during the LTHR that involves a sequence of peroxy-radical-mediated chemistry. To investigate the impact of these additives on first-stage OA formation, we carried out controlled-combustion experiments that covered LTC ranges using three binary fuel mixtures. Each mixture utilizes *n*-heptane as the primary fuel and is combined with one of three additives, each known for their unique octane boosting capabilities: ethanol, toluene, and DMF. Toluene was the least effective in curbing first-stage OA formation, while ethanol and DMF demonstrated more significant reductions, with DMF outperforming ethanol. These findings underscore that additives with a higher inhibitory potency and synergistic effects on RON were markedly more successful in mitigating first-stage OA formation compared to additives displaying antagonistic properties.

## 4.1 Introduction

Advanced compression-ignition (ACI) engines utilizing low-temperature combustion (LTC) have emerged as promising next-generation internal combustion engine solutions that combine characteristics of both spark-ignition (SI) and compression-ignition (CI) engines. These engines are designed to meet stringent emissions standards by significantly reduced NOx and particulate matter (PM) emissions while maintaining high thermal efficiency (Dec & Hwang, 2009; Dec et al., 2006; Epping et al., 2002; Reitz & Duraisamy, 2015; Splitter et al., 2011; Stanglmaier & Roberts, 1999; Zhao et al., 2003). However, one major obstacle impeding its development is the auto-ignition timing and combustion phasing that constrict its operating range at high engine loads (Maurya et al., 2018). Auto-ignition timing is critical in ACI engines and is governed primarily by low temperature (< 800 K) chemical kinetics in which fuel molecular structure have the biggest impact. Certain fuels exhibit two-stage ignition due to $RO_2$ chain branching reactions, mainly the isomerization reaction of $RO_2$, that are highly sensitive to fuel structure and C-H bond strength (Curran et al., 1998; Dagaut et al., 1998; Machrafi, 2008; Ribaucour et al., 2000; Westbrook, 2000). These two-stage ignition fuels exhibit heat release during their first stage ignition known as low temperature heat release (LTHR) that can cause a temperature rise which is a critical feature in shortening ignition delay timing during the second stage ignition (Westbrook, 2000).

Due to the inherent dependence of ACI engines on autoignition, diesel-like fuels are preferred due to their lower autoignition resistivity. *n*-Heptane is a straight-chain paraffin with a research octane number (RON) of 0, a cetane number of 56, and a two-stage ignition behavior (Chevalier et al., 1990; Ranzi et al., 1995), that is often used as a diesel surrogate. Yet, using *n*-heptane exclusively can pose operational limitations in ACI. Owing to its strong first-stage LTHR

behavior, *n*-heptane has a tendency for premature ignition, resulting in over-advanced combustion phasing. Consequently, this can induce excessive engine knock, particularly at elevated fuel-to-air equivalence ratios. Fuel additives are suggested as a simple and effective way to widen the operational range of ACI engines by improving control over ignition timing. These additives can aid in optimizing ignition timing and reducing the magnitude of LTHR by inhibiting OH radicals formed during chain branching reactions that occur at LTC conditions of dual-stage ignition fuels. Shibata *et al.* (Shibata et al., 2005) defined this effect as the "LTHR inhibitor effect." Several studies experimented with primary reference fuels (PRF) which are binary blends of *n*-heptane and iso-octane that have different auto-ignition behavior (Gauthier et al., 2004; Griffiths et al., 2002; Hanson et al., 2010; Machrafi, 2008; Machrafi et al., 2008; Tanaka, Ayala, & Keck, 2003; Tanaka, Ayala, Keck, et al., 2003). Iso-octane is a gasoline-like branched-chain paraffin with high resistance to auto-ignition and single-stage ignition behavior. Commonly used additives include ethanol (Hashimoto, 2007; Herrmann et al., 2014; Lü et al., 2006; Saisirirat et al., 2010; Saisirirat et al., 2011) , methanol (Lü et al., 2007) , *n*-butanol (Saisirirat et al., 2010; Saisirirat et al., 2011), and toluene (Böğrek et al., 2021; Chen et al., 2022; Lee et al., 2019; Machrafi et al., 2008; Shibata & Urushihara, 2007; Waqas et al., 2018). Additionally, some biofuels such as dimethyl ether (DME) (Burke et al., 2015; Herrmann et al., 2014; Rodriguez et al., 2015) and furan derivatives, including 2-methylfuran (2-MF) (Alexandrino, 2020; Singh et al., 2018) and 2,5-dimethylfuran (DMF) (Alexandrino, 2020; Chen et al., 2013; Fioroni et al., 2022; Liu et al., 2013), have shown promising results and have been proposed as potential blending agents for their octane boosting abilities and physicochemical properties.

Saisirirat *et al.* (Saisirirat et al., 2011) studied ignition delays of ethanol/*n*-heptane and butanol/*n*-heptane blends and reported that ethanol is more effective in suppressing OH compared to butanol.

Lü *et al.* (Lü et al., 2007) compared the inhibition effects of different additives, including methanol, ethanol, and iso-propanol. Methanol was the most effective inhibitor; However, ethanol was a better additive in terms of operating ranges, thermal efficiency, and emissions. Mehl *et al.* (Mehl et al., 2011) observed a similar effect of toluene on the first-stage ignition of *n*-heptane in a binary toluene/*n*-heptane mixture, where toluene acted as a radical scavenger that suppressed the reactivity of *n*-heptane during LTHR while maintaining the two-stage ignition behavior. This is attributed to two factors: the readily abstractable H-atoms on the methyl group of toluene that serve as a radical scavenger and the formation of the resonantly stabilized benzyl radical at LTC that favor termination reactions (Emdee et al., 1992; Mehl et al., 2011). Similarly, Singh *et al.* (Singh et al., 2018) showed how 2-MF has a superior suppression ability of LTHR compared to ethanol as an octane booster and noticed a non-linear trend between increasing the blendstock volume (i.e., 2-MF and ethanol) in a PRF mixture and LTHR suppression, where at 20% volumetric blend, 2-MF completely suppressed LTHR, while ethanol still showed some LTHR. Singh explained that this non-linearity is dependent on the effectiveness of the blending agent in scavenging radicals formed during LTC, which further extends to the high temperature reactions. Therefore, once the LTC reactivity is fully suppressed, the effect of octane booster addition becomes linear (Singh et al., 2018). Singh's findings agree with data published from numerous studies that reported synergistic blending behavior for RON from different octane boosters. Synergistic blending refers to the phenomenon where the addition of these compounds results in higher RON values than what would be expected based on a linear-blending model. This characteristic offers a notable advantage as it allows for achieving the desired RON target with a lower volume of additive. On the contrary, some additives showed an antagonistic blending behavior, where the blend RON is less than that predicted by a linear-blending model. Fioroni et al. (Fioroni et al., 2022) showed

that DMF and 2-MF were more efficient RON boosters compared to other blendstocks including prenol, 2-methyl-2-butene (2M2B), and ethanol. DMF and 2-MF were shown to have the highest RON-boosting ability due to the rapid reaction of the OH addition products to other species that pull the OH addition equilibrium toward products. Given its importance in the marketplace, many studies examined ethanol's synergistic blending in petroleum refinery blendstocks (Anderson et al., 2012; Badra et al., 2017; McCormick et al., 2017). McCormick et al. (McCormick et al., 2017) measured the RON of 20 potential bioderived blendstocks blended into a four-component gasoline surrogate: iso-octane, toluene, *n*-heptane, and 1-hexene. Many blendstocks including alcohols, olefins, and alkylfurans blended synergistically. Foong et al. (Foong et al., 2014) showed that ethanol blended synergistically with *n*-heptane, isooctane, and their blends (PRF) but antagonistically with toluene.

The existing literature has extensively examined the influence of fuel blends on ignition properties. However, there is a relatively unexplored aspect concerning aerosol formation in the context of LTC. Formation pathways of aerosols during the second ignition stage (> 1000 K) are well understood as part of the soot-formation process. It begins with the creation of small aromatic species that form polycyclic aromatic hydrocarbons (PAHs). These PAHs, assisted by radical chain reactions, merge with other hydrocarbons to form condensable organic aerosols (OA), marking the onset of incipient soot formation (Johansson et al., 2018; Michelsen, 2017; Wang, 2011). As temperature rises, these OAs undergo a series of dehydrogenation and clustering, eventually forming Elemental Carbon (EC) or mature soot (Michelsen, 2017). The conditions under which combustion takes place govern the transition from incipient to mature soot. Notably, in the field of atmospheric science, it's important to draw attention to the equivalence of EC and black carbon (BC) - a strong light-absorbing material with significant

contribution to climate warming (Bond et al., 2013). Moreover, incipient soot, which may also possess light-absorbing properties, makes up a considerable portion of atmospheric brown carbon (BrC) (Saleh et al., 2018). Thus, the investigation of the formation and physicochemical properties of second-stage aerosol emissions has been a focal point of research for both combustion and atmospheric scientists (Cheng, Atwi, Yu, et al., 2020; El Hajj et al., 2021; Johansson et al., 2018; Saleh et al., 2018). As for first-stage OA, we recently reported a correlation between the first-stage ignition of *n*-heptane and the formation of organic aerosols (OA) we labeled 'first stage OA' that formed within the temperature range (500 – 700 K) where $RO_2$ chain branching reactions (i.e., LTHR) are prevalent (El Hajj et al., 2021). This correlation has significant implications, as it aligns with previous findings suggesting that aerosols emitted from various ACI modes, including Reactivity Controlled Compression Ignition (RCCI), are predominantly organic (Benajes et al., 2017; Curran et al., 2010; Lucachick et al., 2016; Moses-DeBusk et al., 2019; Northrop et al., 2011; Storey et al., 2017). We compared first stage OA emission profile with results from a kinetic model that describe low temperature oxidation of *n*-heptane (Mehl et al., 2011) and confirmed that first stage OA emissions are tied to an increase in fuel reactivity during chain branching reactions at LTC. In a different study, we further investigated formation pathways of first stage OA using *n*-pentane, another two-stage ignition fuel, by incorporating gas phase measurements and unveiled that cyclic ethers species produced from $RO_2$ chain branching reactions undergo $O_2$ addition to form highly oxidized intermediates which result in species of decreased volatility that can partition to the particle phase and contribute to OA formation. Additionally, our evidence highlights that this OA experiences further molecular growth via oligomerization. The formation of oligomers influences the particle phase by reducing molecular volatility. Simultaneously, it creates a condensation sink that

encourages additional monomers to condense and undergo oligomerization. This feedback mechanism ultimately supports a cycle of continuous condensational particle growth (Chapter 3). In our previous research, we focused exclusively on single-component fuels. Yet, for ACI operations, the necessity for additives that augment ignition properties by scavenging radicals generated during LTC comes into play. These additives can significantly influence first-stage OA formation. In the current study, we expand this focus by conducting controlled-combustion experiments at temperatures relevant to LTC utilizing three binary fuel mixtures, each employing *n*-heptane as the primary fuel, combined with three distinct additives known for their varying radical scavenging capabilities. We measured OA emission profiles under various temperatures and blending ratios, while also probing the impact of the additives on the chemical composition of the first-stage OA using ultra-high resolution mass spectrometry.

## 4.2. Methods

### 4.2.1. Overview

We conducted experiments to explore OA formation from the combustion of binary fuel blends with *n*-heptane as the primary fuel. We chose *n*-heptane as the primary fuel due to its high reactivity (RON = 0). We incorporated three additives that are commonly used in LTC to improve autoignition properties in ACI engines: toluene (aromatic) (Böğrek et al., 2021; Lee et al., 2019; Machrafi et al., 2008; Shibata & Urushihara, 2007; Waqas et al., 2018), ethanol (alcohol) (Lü et al., 2007; Saisirirat et al., 2011), and DMF (furan derivative) (Alexandrino, 2020; Chen et al., 2013; Liu et al., 2013). Mixtures were blended on molar basis, maintaining an equivalence ratio $\phi = 1$ and $O_2/N_2 = 0.1$. We adopt the notations $T_x$, $E_x$, and $D_x$ to denote the respective quantities (in mol%) of toluene, ethanol, and DMF, respectively, where the subscript 'x' indicates the molar percentage of the additive in the blend. The experiments were performed

at combustion temperatures ranging between 500 K and 1200 K, which span the first and second stage ignition. We carried out real-time measurements for the size and mass distributions of OA emitted from pure *n*-heptane combustion and compared these to OA emissions from the blends. For a more profound understanding of the effect of additives on OA's chemical composition, we conducted offline chemical analyses. This involved analyzing sample filters collected at select conditions, particularly at temperatures that emitted highest OA for pure *n*-heptane and blends with 30%$_{mol}$ additive content.

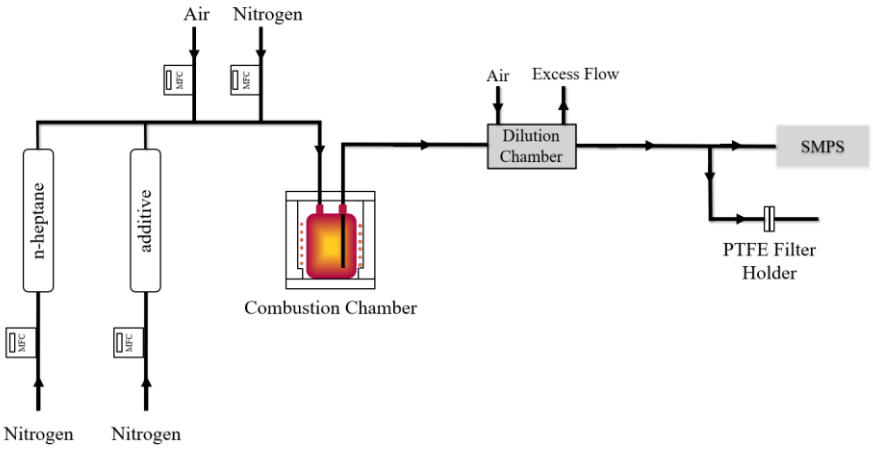


**Figure 4.1.** Schematic of the combustion system and the sampling setup

### 4.2.2. Combustion experiments

The experimental setup used for this study, which has been described in a previous work (Atwi et al., 2022; Atwi et al., 2021; Cheng, Atwi, Hajj, et al., 2020; Cheng et al., 2019; El Hajj et al., 2021; Saleh et al., 2018), was modified to enable the use of binary fuel mixtures (Fig. 4.1). The system consists of a 0.24 L quartz chamber reactor that is enclosed within an insulated heater controlled by a PID temperature controller (OMEGA, model CNi3244) using a K-type thermocouple inserted in the middle of the reactor. The fuel blend was prepared by combining *n*-heptane and the blending agent using a dual-bubbler system. Prior to entering the reactor, the

blend was mixed with clean, dry air. Ultra-high purity nitrogen ($N_2$) served as the carrier gas in each bubbler, and the desired blending ratios were achieved by controlling the flow rate of $N_2$ using mass flow controllers (GC1 Series, Dakota Instruments, NY, USA). The bubbler design ensured that the $N_2$ exiting the system was fully saturated with the fuel, as confirmed by mass transfer calculations (Cheng et al., 2019). Therefore, the molar flowrate of each fuel could be calculated from knowledge of the fuel's saturation pressure and $N_2$ flowrate. Check valves were installed at the outlet of each bubbler to prevent backflow. Throughout the experiments with varying blending ratios, a fixed equivalence ratio of $\phi = 1$ and an $O_2/N_2$ ratio of 0.1 were maintained. The total flow rate entering the reactor was set at 1 standard liter per minute (SLPM), resulting in an average residence time of approximately 14 seconds. The calculations to determine the flow rates of $N_2$ in each bubbler as well the flowrate of dilution air used in each experiment to maintain the desired blend ratio and total flowrate of 1 SLPM are given in the supporting information (SI). For each additive, blending ratios varied between $30\%_{mol}$ - $70\%_{mol}$ for toluene and ethanol, and $10\%_{mol}$ - $50\%_{mol}$ for DMF.

The exhaust sample from the reactor was diluted in a 4 L glass dilution chamber using clean dry air prior to sampling (Fig.4.1). We continuously measured the emitted aerosol particle size distribution at 90-seconds resolution at different combustion temperatures using a scanning mobility particle sizer (SMPS, TSI model 3882) in the range of 10-500 nm. The SMPS uses an electrostatic classifier (TSI, Model 3082), a long differential mobility analyzer (DMA, TSI, Model 3081A00), and an advanced aerosol neutralizer (TSI, Model 3088) along with a condensation particle counter (CPC, TSI, Model 3772). We obtained the total mass concentrations ($\mu g/m^3$) at different combustion temperatures by integrating the size distributions using an effective density of 1.3 $g/cm^3$ that we previously obtained from a tandem differential

mobility analyzer – aerosol particle sizer (tandem DMA-APM) setup (El Hajj et al., 2021; McMurry et al., 2002).

### 4.3. Results

Figure 4.2 represents the variation in organic aerosol (OA) mass concentration produced during the combustion of *n*-heptane, toluene, and their respective blends, plotted against temperature. A notable observation is that pure *n*-heptane exclusively generated first-stage aerosols, with no detectable emissions at elevated temperatures (> 800 K). In contrast, toluene, well-known for its propensity to form larger organic molecules (including PAHs and their derivatives) during high temperature combustion regimes, demonstrated a different trend, primarily emitting aerosols at the higher temperature. This indicates that first-stage aerosol emissions from two-stage ignition fuels like *n*-heptane are produced, even when higher-temperature conditions don't favor the formation of incipient soot particles. The peak OA concentration emitted for the first stage emissions of *n*-heptane is roughly 3.5 times greater than that produced by toluene at 958 K.

For the binary *n*-heptane/toluene mixtures, we observed a linear decrease in peak emissions during the first stage as the molar fraction of toluene in the blend increased. Contrariwise, the second stage OA emissions exhibited a non-linear increase with a rising proportion of toluene (as depicted in Fig. 4.2). Moreover, as the fraction of toluene in the blend increased, we observed a subtle upward shift in the temperature that corresponded to peak emissions in both stages. This shift could be associated with a delay in ignition, as the introduction of toluene raises the overall RON, thereby shifting the aerosol precursors profiles to a slightly higher temperature. The same pattern was evident for the other fuel blends as well.

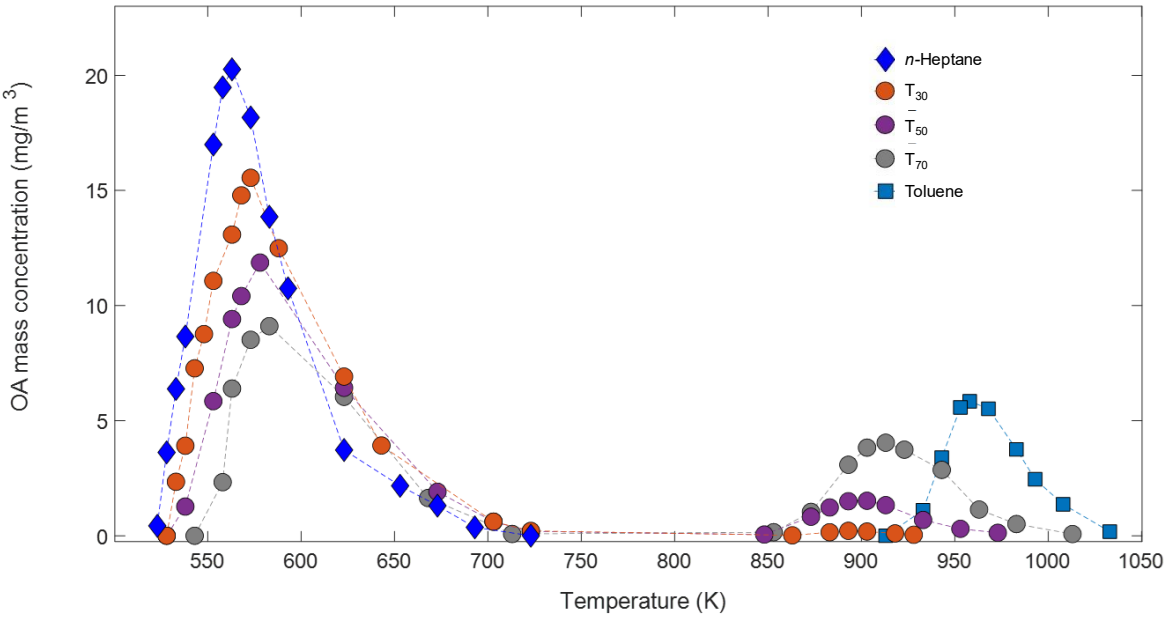


**Figure 4.2.** OA mass concentration emitted from the combustion of pure *n*-heptane (◊), toluene (■), and binary *n*-heptane/toluene blends (●) as a function of combustion temperature covering low, intermediate, and high temperature combustion regimes.

The OA emission profiles for blends of *n*-heptane with ethanol and DMF are depicted in Figures 4.3a and 4.3b, respectively. While there's an absence of aerosol emissions at high temperatures for both ethanol and DMF, their effect on emissions during the first stage is apparent. Both additives showed a higher tendency in suppressing first-stage OA compared to toluene, and unlike toluene, increasing ethanol and DMF fractions showed a non-linear decrease in first stage OA. For instance, the introduction of a $30\%_{mol}$ additive led to a significant reduction in peak emissions compared to that of toluene. Specifically, a decrease by a factor of 1.3 was observed for $T_{30}$, while $E_{30}$ and $D_{30}$ experienced a more substantial decrease by factors of 2.3 and 3, respectively. DMF demonstrated a greater efficiency in suppressing first-stage OA compared to ethanol; emissions were still observed at $E_{50}$, whereas they were almost entirely absent at $D_{50}$,

which showed a more drastic shift in temperature corresponding to peak emissions (793 K for $D_{50}$ and 583 K for $E_{50}$).

The results presented here suggest that the strong inhibition effects demonstrated by DMF and ethanol during LTC (Fioroni et al., 2022) and their radical scavenging abilities eventually influence the formation of first stage OA by decreasing the abundance of OA precursors. With DMF being a more potent inhibitor, due to its OH-addition and H-abstraction reactions at LTC, it consequently results in a more significant reduction of first stage OA emissions as its proportion increases in the blend.

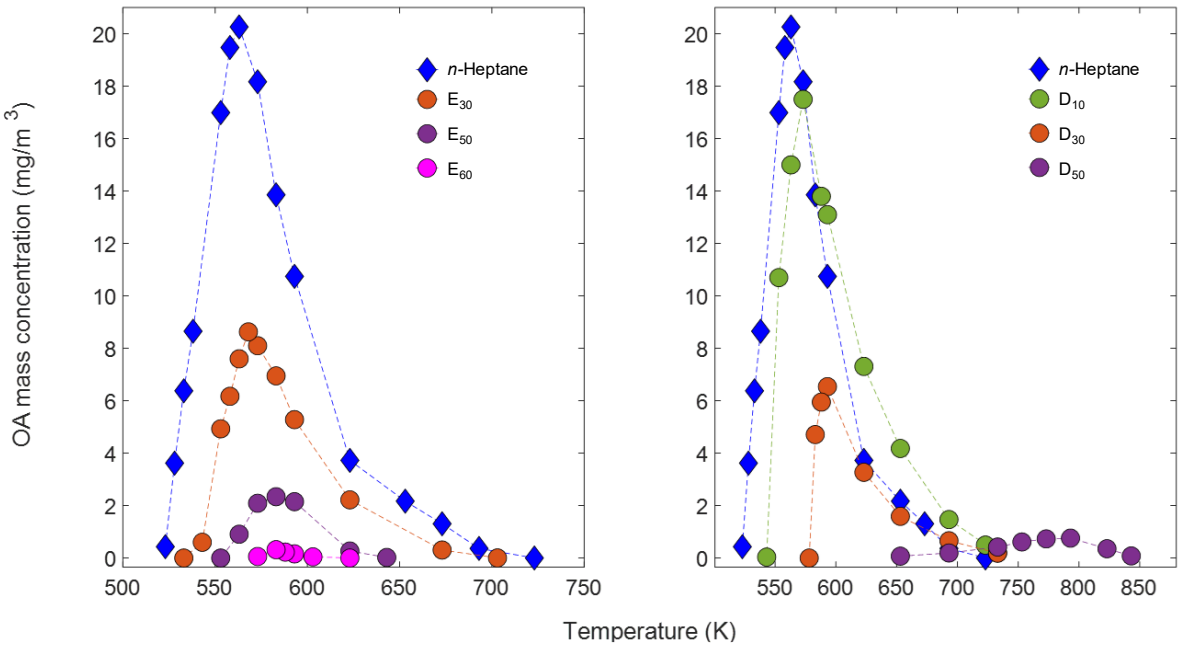


**Figure 4.3.** OA mass concentration emitted from the combustion of pure *n*-heptane (◊), and (a) binary *n*-heptane/ethanol (b) binary *n*-heptane/DMF blends (●) as a function of combustion temperature covering LTC range.

Blends of *n*-heptane and toluene exhibit a nearly linear relationship with a slight antagonistic behavior in terms of RON when mixed on a molar basis (Pera & Knop, 2012; Yuan et al., 2020; Yuan et al., 2017). This indicates that toluene has a near-linear effect in scavenging the radicals

that cause LTHR during LTC. Figure 4.4 illustrates how the influence of toluene on first-stage OA emissions is reflected, where the peak OA concentrations from Fig. 4.3a are plotted against toluene fraction in the blend. The peak emissions of *n*-heptane/toluene blends show a nearly linear decrease, with slightly higher concentrations compared to the linear-mixing model. These slightly elevated concentrations are indicative of the slight antagonistic effect exhibited by toluene (Yuan et al., 2020). Furthermore, the *n*-heptane/ethanol and *n*-heptane/DMF blends, known for their radical scavenging ability during LTC, exhibit a strong synergistic blending behavior in terms of RON. This synergistic effect is also observed in the emissions of first-stage OA, as depicted in Figure 4.4. The peak OA concentrations for these blends are lower than what would be expected based on the linear-mixing model. Among the two additives, DMF demonstrates a greater impact in reducing the peak OA concentrations due to its superior radical scavenging ability, as previously demonstrated by Fioroni *et al*. (Fioroni et al., 2022).

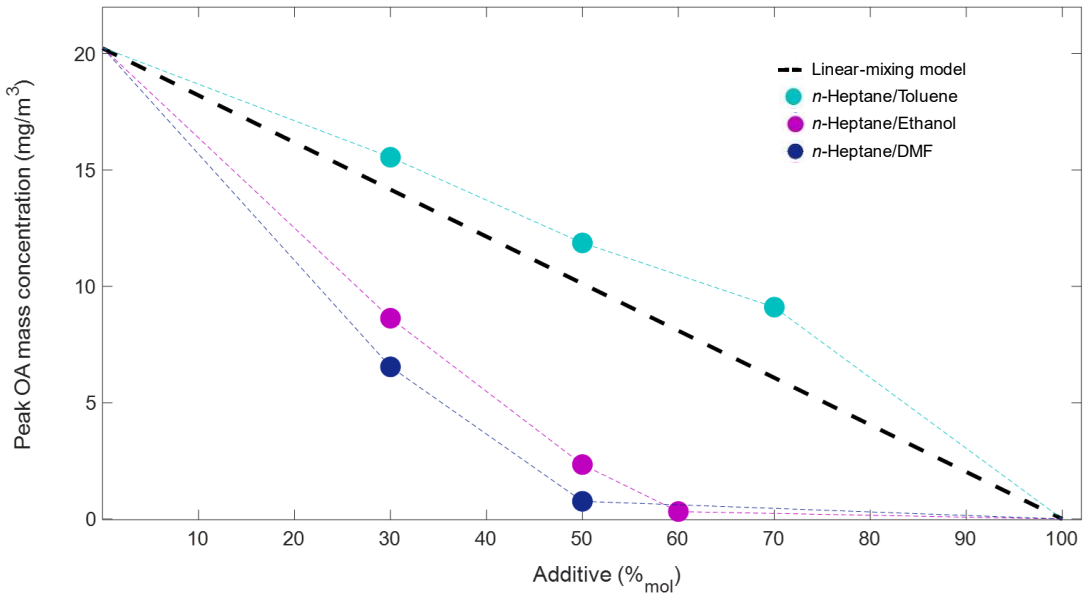


**Figure 4.4.** Peak first-stage OA mass concentration from Fig. 4.3 as a function of additive fraction ($\%_{mol}$) in the blend. The dashed line corresponds to a linear-mixing model, which signifies the expected linear decline in first-stage OA concentration observed in pure *n*-heptane.

### 4.4. Conclusions

In this investigation, we employed three distinct binary fuel combinations, using *n*-heptane as the main component, to explore the influence of additives on first-stage OA formation during LTC. These additives are known to enhance autoignition and provide better control in combustion phasing in ACI engines. We measured OA emissions emitted from controlled-combustion experiments at a fixed equivalence ratio and temperatures known to instigate LTHR in *n*-heptane using three different additives at varying blending ratios. The observations from our study concurred with prior research illustrating that additives which efficiently scavenge radicals and demonstrate a synergistic effect on RON are better in suppressing first-stage OAs than those which exhibit a weaker, more antagonistic effect. For instance, ethanol and DMF, recognized for their synergistic blending behavior, demonstrated a non-linear reduction in first-stage OA as their proportion increased. Conversely, toluene, known for its slight antagonism when mixed with *n*-heptane, revealed an almost linear, albeit slightly elevated, first-stage OA pattern compared to a linear decay. These results represent the first evidence of the impact of fuel additives, used to enhance the operational range of ACI engines, on OA formation during LTC. The study underscores the necessity of expanding research to encompass a broader array of additives and fuel blends. This will provide a more comprehensive understanding of pollutant formation, which is crucial for assessing the environmental impact of new development in internal combustion engines that employ ACI strategies.

## References


Alexandrino, K. (2020). Comprehensive review of the impact of 2, 5-Dimethylfuran and 2-Methylfuran on soot emissions: Experiments in diesel engines and at laboratory-scale. *Energy & Fuels*, *34*(6), 6598-6623.

Anderson, J. E., Leone, T. G., Shelby, M. H., Wallington, T. J., Bizub, J. J., Foster, M., Lynskey, M. G., & Polovina, D. (2012). *Octane numbers of ethanol-gasoline blends: measurements and novel estimation method from molar composition* (0148-7191).

Atwi, K., Cheng, Z., El Hajj, O., Perrie, C., & Saleh, R. (2022). A dominant contribution to light absorption by methanol-insoluble brown carbon produced in the combustion of biomass fuels typically consumed in wildland fires in the United States. *Environmental Science: Atmospheres*, *2*(2), 182-191.

Atwi, K., Mondal, A., Pant, J., Cheng, Z., El Hajj, O., Ijeli, I., Handa, H., & Saleh, R. (2021). Physicochemical properties and cytotoxicity of brown carbon produced under different combustion conditions. *Atmospheric Environment*, *244*, 117881.

Badra, J., AlRamadan, A. S., & Sarathy, S. M. (2017). Optimization of the octane response of gasoline/ethanol blends. *Applied Energy*, *203*, 778-793.

Benajes, J., García, A., Monsalve-Serrano, J., & Boronat, V. (2017). An investigation on the particulate number and size distributions over the whole engine map from an optimized combustion strategy combining RCCI and dual-fuel diesel-gasoline. *Energy Conversion and Management*, *140*, 98-108.

Böğrek, A., Haşimoğlu, C., Calam, A., & Aydoğan, B. (2021). Effects of n-heptane/toluene/ethanol ternary fuel blends on combustion, operating range and emissions in premixed low temperature combustion. *Fuel*, *295*, 120628.

Bond, T. C., Doherty, S. J., Fahey, D. W., Forster, P. M., Berntsen, T., DeAngelo, B. J., Flanner, M. G., Ghan, S., Kärcher, B., & Koch, D. (2013). Bounding the role of black carbon in the climate system: A scientific assessment. *Journal of Geophysical Research: Atmospheres*, *118*(11), 5380-5552.

Burke, U., Somers, K. P., O'Toole, P., Zinner, C. M., Marquet, N., Bourque, G., Petersen, E. L., Metcalfe, W. K., Serinyel, Z., & Curran, H. J. (2015). An ignition delay and kinetic modeling study of methane, dimethyl ether, and their mixtures at high pressures. *Combustion and Flame*, *162*(2), 315-330.

Chen, B., Liu, P., Xu, Q., Wang, Z., Roberts, W. L., & Pitsch, H. (2022). Low temperature oxidation of toluene in an n-heptane/toluene mixture. *Combustion and Flame*, *242*, 112200.

Chen, G., Shen, Y., Zhang, Q., Yao, M., Zheng, Z., & Liu, H. (2013). Experimental study on combustion and emission characteristics of a diesel engine fueled with 2, 5-dimethylfuran–diesel, n-butanol–diesel and gasoline–diesel blends. *Energy*, *54*, 333-342.

Cheng, Z., Atwi, K., Hajj, O. E., Ijeli, I., Fischer, D. A., Smith, G., & Saleh, R. (2020). Discrepancies between brown carbon light-absorption properties retrieved from online and offline measurements. *Aerosol Science and Technology*, 1-12.

Cheng, Z., Atwi, K., Onyima, T., & Saleh, R. (2019). Investigating the dependence of light-absorption properties of combustion carbonaceous aerosols on combustion conditions. *Aerosol Science and Technology*, *53*(4), 419-434.

Cheng, Z., Atwi, K. M., Yu, Z., Avery, A., Fortner, E. C., Williams, L., Majluf, F., Krechmer, J. E., Lambe, A. T., & Saleh, R. (2020). Evolution of the light-absorption properties of

combustion brown carbon aerosols following reaction with nitrate radicals. *Aerosol Science and Technology*, *54*(7), 849-863. https://doi.org/10.1080/02786826.2020.1726867

Chevalier, C., Warnatz, J., & Melenk, H. (1990). Automatic generation of reaction mechanisms for the description of the oxidation of higher hydrocarbons. *Berichte der Bunsengesellschaft für physikalische Chemie*, *94*(11), 1362-1367.

Curran, H. J., Pitz, W. J., Westbrook, C. K., Callahan, G., & Dryer, F. L. (1998). Oxidation of automotive primary reference fuels at elevated pressures. Symposium (International) on Combustion,

Curran, S., Prikhodko, V., Cho, K., Sluder, C. S., Parks, J., Wagner, R., Kokjohn, S., & Reitz, R. D. (2010). *In-cylinder fuel blending of gasoline/diesel for improved efficiency and lowest possible emissions on a multi-cylinder light-duty diesel engine* (0148-7191).

Dagaut, P., Daly, C., Simmie, J. M., & Cathonnet, M. (1998). The oxidation and ignition of dimethylether from low to high temperature (500–1600 K): Experiments and kinetic modeling. Symposium (International) on Combustion,

Dec, J. E., & Hwang, W. (2009). Characterizing the development of thermal stratification in an HCCI engine using planar-imaging thermometry. *SAE International Journal of Engines*, *2*(1), 421-438.

Dec, J. E., Hwang, W., & Sjöberg, M. (2006). An investigation of thermal stratification in HCCI engines using chemiluminescence imaging. *SAE Transactions*, 759-776.

El Hajj, O., Atwi, K., Cheng, Z., Koritzke, A., Christianson, M., Dewey, N., Rotavera, B., & Saleh, R. (2021). Two-stage aerosol formation in low-temperature combustion. *Fuel*, *304*, 121322.

Emdee, J., Brezinsky, K., & Glassman, I. (1992). A kinetic model for the oxidation of toluene near 1200 K. *The Journal of Physical Chemistry*, *96*(5), 2151-2161.

Epping, K., Aceves, S., Bechtold, R., & Dec, J. E. (2002). *The potential of HCCI combustion for high efficiency and low emissions* (0148-7191).

Fioroni, G. M., Rahimi, M. J., Westbrook, C. K., Wagnon, S. W., Pitz, W. J., Kim, S., & McCormick, R. L. (2022). Chemical kinetic basis of synergistic blending for research octane number. *Fuel*, *307*, 121865.

Foong, T. M., Morganti, K. J., Brear, M. J., da Silva, G., Yang, Y., & Dryer, F. L. (2014). The octane numbers of ethanol blended with gasoline and its surrogates. *Fuel*, *115*, 727-739.

Gauthier, B., Davidson, D. F., & Hanson, R. K. (2004). Shock tube determination of ignition delay times in full-blend and surrogate fuel mixtures. *Combustion and Flame*, *139*(4), 300-311.

Griffiths, J., MacNamara, J., Sheppard, C., Turton, D., & Whitaker, B. (2002). The relationship of knock during controlled autoignition to temperature inhomogeneities and fuel reactivity. *Fuel*, *81*(17), 2219-2225.

Hanson, R. M., Kokjohn, S. L., Splitter, D. A., & Reitz, R. D. (2010). An experimental investigation of fuel reactivity controlled PCCI combustion in a heavy-duty engine. *SAE international journal of engines*, *3*(1), 700-716.

Hashimoto, K. (2007). *Effect of Ethanol on the HCCI Combustion* (0148-7191).

Herrmann, F., Jochim, B., Oßwald, P., Cai, L., Pitsch, H., & Kohse-Höinghaus, K. (2014). Experimental and numerical low-temperature oxidation study of ethanol and dimethyl ether. *Combustion and Flame*, *161*(2), 384-397.

Johansson, K., Head-Gordon, M., Schrader, P., Wilson, K., & Michelsen, H. (2018). Resonance-stabilized hydrocarbon-radical chain reactions may explain soot inception and growth. *science*, *361*(6406), 997-1000.

Lee, C.-f., Wu, Y., Wu, H., Shi, Z., Zhang, L., & Liu, F. (2019). The experimental investigation on the impact of toluene addition on low-temperature ignition characteristics of diesel spray. *Fuel*, *254*, 115580.

Liu, H., Xu, J., Zheng, Z., Li, S., & Yao, M. (2013). Effects of fuel properties on combustion and emissions under both conventional and low temperature combustion mode fueling 2, 5-dimethylfuran/diesel blends. *Energy*, *62*, 215-223.

Lü, X., Hou, Y., Zu, L., & Huang, Z. (2006). Experimental study on the auto-ignition and combustion characteristics in the homogeneous charge compression ignition (HCCI) combustion operation with ethanol/n-heptane blend fuels by port injection. *Fuel*, *85*(17-18), 2622-2631.

Lü, X., Ji, L., Zu, L., Hou, Y., Huang, C., & Huang, Z. (2007). Experimental study and chemical analysis of n-heptane homogeneous charge compression ignition combustion with port injection of reaction inhibitors. *Combustion and Flame*, *149*(3), 261-270.

Lucachick, G., Curran, S., Storey, J., Prikhodko, V., & Northrop, W. F. (2016). Volatility characterization of nanoparticles from single and dual-fuel low temperature combustion in compression ignition engines. *Aerosol Science and Technology*, *50*(5), 436-447.

Machrafi, H. (2008). Experimental validation of a kinetic multi-component mechanism in a wide HCCI engine operating range for mixtures of n-heptane, iso-octane and toluene: Influence of EGR parameters. *Energy Conversion and Management*, *49*(11), 2956-2965.

Machrafi, H., Cavadias, S., & Gilbert, P. (2008). An experimental and numerical analysis of the HCCI auto-ignition process of primary reference fuels, toluene reference fuels and diesel fuel in an engine, varying the engine parameters. *Fuel processing technology*, *89*(11), 1007-1016.

Maurya, R. K., Maurya, R. K., & Luby. (2018). *Characteristics and control of low temperature combustion engines*. Springer.

McCormick, R. L., Fioroni, G., Fouts, L., Christensen, E., Yanowitz, J., Polikarpov, E., Albrecht, K., Gaspar, D. J., Gladden, J., & George, A. (2017). Selection criteria and screening of potential biomass-derived streams as fuel blendstocks for advanced spark-ignition engines. *SAE International Journal of Fuels and Lubricants*, *10*(2), 442-460.

McMurry, P. H., Wang, X., Park, K., & Ehara, K. (2002). The relationship between mass and mobility for atmospheric particles: A new technique for measuring particle density. *Aerosol Science & Technology*, *36*(2), 227-238.

Mehl, M., Pitz, W. J., Westbrook, C. K., & Curran, H. J. (2011). Kinetic modeling of gasoline surrogate components and mixtures under engine conditions. *Proceedings of the Combustion Institute*, *33*(1), 193-200.

Michelsen, H. (2017). Probing soot formation, chemical and physical evolution, and oxidation: A review of in situ diagnostic techniques and needs. *Proceedings of the Combustion Institute*, *36*(1), 717-735.

Moses-DeBusk, M., Curran, S. J., Lewis, S. A., Connatser, R. M., & Storey, J. M. (2019). Impacts of Air-Fuel Stratification in ACI Combustion on Particulate Matter and Gaseous Emissions. *Emission Control Science and Technology*, *5*(3), 225-237.

Northrop, W. F., Madathil, P. V., Bohac, S. V., & Assanis, D. N. (2011). Condensational growth of particulate matter from partially premixed low temperature combustion of biodiesel in a compression ignition engine. *Aerosol Science and Technology, 45*(1), 26-36.

Pera, C., & Knop, V. (2012). Methodology to define gasoline surrogates dedicated to auto-ignition in engines. *Fuel*, *96*, 59-69.

Ranzi, E., Gaffuri, P., Faravelli, T., & Dagaut, P. (1995). A wide-range modeling study of n-heptane oxidation. *Combustion and Flame, 103*(1-2), 91-106.

Reitz, R. D., & Duraisamy, G. (2015). Review of high efficiency and clean reactivity controlled compression ignition (RCCI) combustion in internal combustion engines. *Progress in Energy and Combustion Science*, *46*, 12-71.

Ribaucour, M., Minetti, R., Sochet, L., Curran, H., Pitz, W., & Westbrook, C. (2000). Ignition of isomers of pentane: an experimental and kinetic modeling study. *Proceedings of the Combustion Institute, 28*(2), 1671-1678.

Rodriguez, A., Frottier, O., Herbinet, O., Fournet, R., Bounaceur, R., Fittschen, C., & Battin-Leclerc, F. (2015). Experimental and modeling investigation of the low-temperature oxidation of dimethyl ether. *The Journal of Physical Chemistry A, 119*(28), 7905-7923.

Saisirirat, P., Foucher, F., Chanchaona, S., & Mounaïm-Rousselle, C. (2010). Spectroscopic measurements of low-temperature heat release for homogeneous combustion compression ignition (HCCI) n-heptane/alcohol mixture combustion. *Energy & Fuels, 24*(10), 5404-5409.

Saisirirat, P., Togbé, C., Chanchaona, S., Foucher, F., Mounaïm-Rousselle, C., & Dagaut, P. (2011). Auto-ignition and combustion characteristics in HCCI and JSR using 1-butanol/n-heptane and ethanol/n-heptane blends. *Proceedings of the Combustion Institute*, *33*(2), 3007-3014.

Saleh, R., Cheng, Z., & Atwi, K. (2018). The brown–black continuum of light-absorbing combustion aerosols. *Environmental Science & Technology Letters, 5*(8), 508-513.

Shibata, G., Oyama, K., Urushihara, T., & Nakano, T. (2005). *Correlation of low temperature heat release with fuel composition and HCCI engine combustion* (0148-7191).

Shibata, G., & Urushihara, T. (2007). Auto-ignition characteristics of hydrocarbons and development of HCCI fuel index. *SAE Transactions*, 304-323.

Singh, E., Shankar, V. S. B., Tripathi, R., Pitsch, H., & Sarathy, S. M. (2018). 2-Methylfuran: A bio-derived octane booster for spark-ignition engines. *Fuel*, *225*, 349-357.

Splitter, D., Hanson, R., Kokjohn, S., & Reitz, R. D. (2011). *Reactivity controlled compression ignition (RCCI) heavy-duty engine operation at mid-and high-loads with conventional and alternative fuels* (0148-7191).

Stanglmaier, R. H., & Roberts, C. E. (1999). Homogeneous charge compression ignition (HCCI): benefits, compromises, and future engine applications. *SAE Transactions*, 2138-2145.

Storey, J. M., Curran, S. J., Lewis, S. A., Barone, T. L., Dempsey, A. B., Moses-DeBusk, M., Hanson, R. M., Prikhodko, V. Y., & Northrop, W. F. (2017). Evolution and current understanding of physicochemical characterization of particulate matter from reactivity controlled compression ignition combustion on a multicylinder light-duty engine. *International Journal of Engine Research*, *18*(5-6), 505-519.

Tanaka, S., Ayala, F., & Keck, J. C. (2003). A reduced chemical kinetic model for HCCI combustion of primary reference fuels in a rapid compression machine. *Combustion and Flame*, *133*(4), 467-481.

Tanaka, S., Ayala, F., Keck, J. C., & Heywood, J. B. (2003). Two-stage ignition in HCCI combustion and HCCI control by fuels and additives. *Combustion and Flame*, *132*(1-2), 219-239.

Wang, H. (2011). Formation of nascent soot and other condensed-phase materials in flames. *Proceedings of the Combustion Institute, 33*(1), 41-67.

Waqas, M. U., Masurier, J.-B., Sarathy, M., & Johansson, B. (2018). *Blending octane number of toluene with gasoline-like and PRF fuels in HCCI combustion mode* (0148-7191).

Westbrook, C. K. (2000). Chemical kinetics of hydrocarbon ignition in practical combustion systems. *Proceedings of the Combustion Institute*, *28*(2), 1563-1577.

Yuan, H., Chen, Z., Zhou, Z., Yang, Y., Brear, M. J., & Anderson, J. E. (2020). Formulating gasoline surrogate for emulating octane blending properties with ethanol. *Fuel*, *261*, 116243.

Yuan, H., Yang, Y., Brear, M. J., Foong, T. M., & Anderson, J. E. (2017). Optimal octane number correlations for mixtures of toluene reference fuels (TRFs) and ethanol. *Fuel*, *188*, 408-417.

Zhao, F., Asmus, T. N., Assanis, D. N., Dec, J. E., Eng, J. A., & Najt, P. M. (2003). *Homogeneous charge compression ignition (HCCI) engines*.

# CHAPTER 5

# CONCLUSION

This dissertation sets out to elucidate the properties and formation processes of 'first-stage' organic aerosols that accompany the first ignition phase of two-stage ignition fuels, a comprehension that is essential when assessing the possible atmospheric impacts of forthcoming engine technologies. Organized around three core pursuits, the dissertation examines: a) the disparity in physicochemical traits between first and second-stage aerosols as unveiled by controlled-combustion experiments; b) formation pathways, prevalence in engine emissions, and potential implications for urban atmospheres of first-stage aerosols; and c) the impact of additives, employed to enhance ignition properties in ACI, on the evolution and attributes of first-stage aerosols.

The initial combustion experiments shed light on the emergence of organic aerosols linked to first-stage ignition in two-stage ignition fuels. The experiments spanned the LTC temperature range where first-stage OA were identified during *n*-heptane combustion, a fuel known for its LTHR properties; However, this phenomenon was absent with toluene. A kinetic model replicating our experimental conditions confirmed the connection between first-stage OA and LTHR. It highlighted that the fuel reactivity intensified in sync with the elevation of first-stage OA concentrations.

In our expanded research, we incorporated the analysis of gas-phase species emitted during *n*-pentane's LTC, an additional fuel exhibiting two-stage ignition. This broader examination, together with a detailed chemical characterization of first-stage OA, facilitated our understanding

of the chemical pathways leading to the formation of first-stage OA. Additionally, we identified the existence of OxyPOA, which exhibit chemical properties akin to SOA. Notably, our research furnished proof of OxyPOA presence within the emissions of gasoline and Advanced Compression Ignition (ACI) engines.

Finally, understanding the need for fuel additives in ACI engines, which serve to suppress radical formation and enhance autoignition timing, we furthered our research by incorporating three distinct additives known for their various radical inhibiting capabilities. These were combined with *n*-heptane to observe how they might influence the production of first-stage OA. What we found was that the additives that were more effective at inhibiting radicals also more effectively suppressed the formation of first-stage OA. Additionally, each additive revealed a unique impact on the chemical composition of the resultant first-stage OA.

# APPENDIX A

## CHAPTER 2 SUPPORTING INFORMATION

## TWO-STAGE AEROSOL FORMATION IN LOW-TEMPERATURE COMBUSTION

**Table S2.1. Summary of experimental conditions and emission factors.**

| Fuel | Bubbler flowrate (LPM)* | Air flowrate (LPM) | Additional $N_2$ flowrate (LPM) | Combustion Temperature (˚C) | Emission Factor (mg/Kg.Fuel) | | |
|---|---|---|---|---|---|---|---|
| | | | | | Exp. 1 | Exp. 2 | Exp. 3 |
| *n*-Heptane | 0.18 | 0.2 | 0.4 | 1035 | 37.7 | 41.1 | 38.1 |
| | | | | 1000 | 14.6 | 0.7 | 0.6 |
| | | | | 950 | 0.0 | 0.0 | 0.0 |
| | | | | 900 | 0.0 | 0.0 | 0.0 |
| | | | | 800 | 0.0 | 0.0 | 0.0 |
| | | | | 700 | 0.0 | 0.0 | 0.0 |
| | | | | 600 | 0.0 | 0.0 | 0.0 |
| | | | | 500 | 0.0 | 0.0 | 0.0 |
| | | | | 400 | 0.0 | 0.0 | 0.0 |
| | | | | 390 | 2.9 | 0.0 | 0.0 |
| | | | | 380 | 4.5 | 0.7 | 0.7 |
| | | | | 365 | 17.4 | 9.7 | 9.7 |
| | | | | 350 | 53.4 | 43.7 | 34.2 |
| | | | | 330 | 106.5 | 88.0 | 88.7 |
| | | | | 300 | 213.5 | 190.9 | 188.8 |
| | | | | 290 | 223.0 | 219.6 | 219.6 |
| | | | | 280 | 196.6 | 165.9 | 190.7 |
| | | | | 270 | 126.3 | 76.4 | 122.5 |
| | | | | 260 | 33.0 | 7.6 | 37.9 |
| | | | | 255 | 5.8 | 0.0 | 9.5 |
| | | | | 245 | 0.0 | 0.0 | 0.0 |
| Toluene | 0.307 | 0.19 | 0.25 | 1035 | 789.8 | 798.7 | 798.7 |
| | | | | 1000 | 169.6 | 181.6 | 183.3 |
| | | | | 950 | 28.8 | 25.8 | 40.2 |
| | | | | 900 | 9.9 | 7.3 | 17.7 |
| | | | | 850 | 10.3 | 7.9 | 18.0 |
| | | | | 800 | 6.2 | 4.3 | 8.3 |
| | | | | 750 | 0.4 | 0.2 | 0.9 |
| | | | | 700 | 0.0 | 0.0 | 0.0 |
| | | | | 650 | 0.0 | 0.0 | 0.0 |
| | | | | 600 | 0.0 | 0.0 | 0.0 |
| | | | | 550 | 0.0 | 0.0 | 0.0 |
| | | | | 500 | 0.0 | 0.0 | 0.0 |
| | | | | 450 | 0.0 | 0.0 | 0.0 |

| | | | | | | | |
|---|---|---|---|---|---|---|---|
| | | | | 400 | 0.0 | 0.0 | 0.0 |
| | | | | 350 | 0.0 | 0.0 | 0.0 |
| | | | | 300 | 0.0 | 0.0 | 0.0 |
| | | | | 250 | 0.0 | 0.0 | 0.0 |

***** $N_2$ was used to carry the fuel (in the bubbler) in the toluene experiments, while air was used to carry the fuel in the *n*-heptane experiments.

**Table S2.2. Summary of optical properties data at select combustion temperatures.**

| Fuel | Combustion Temperature (˚C) | Imaginary part of the refractive index | | | | Mass absorption cross-section ($m^2/g$) | | |
|---|---|---|---|---|---|---|---|---|
| | | measurement # | $k_{422}$ | $k_{532}$ | $k_{782}$ | $MAC_{422}$ | $MAC_{532}$ | $MAC_{782}$ |
| Toluene | 1035 | 1 | 0.13 | 0.04 | 0.02 | 2.40 | 0.60 | 0.19 |
| | | 2 | 0.12 | 0.04 | 0.02 | 2.33 | 0.60 | 0.19 |
| | | 3 | 0.12 | 0.04 | 0.02 | 2.31 | 0.56 | 0.18 |
| | | 4 | 0.12 | 0.04 | 0.02 | 2.35 | 0.60 | 0.19 |
| | | 5 | 0.12 | 0.04 | 0.02 | 2.36 | 0.60 | 0.21 |
| | | 6 | 0.13 | 0.04 | 0.02 | 2.42 | 0.62 | 0.21 |
| | | 7 | 0.12 | 0.04 | 0.02 | 2.35 | 0.60 | 0.20 |
| | | 8 | 0.11 | 0.03 | 0.02 | 2.01 | 0.48 | 0.14 |
| | | 9 | 0.11 | 0.03 | 0.02 | 2.01 | 0.48 | 0.15 |
| | | 10 | 0.12 | 0.04 | 0.02 | 2.15 | 0.52 | 0.16 |
| | | 11 | 0.11 | 0.03 | 0.02 | 2.08 | 0.50 | 0.15 |
| | | 12 | 0.11 | 0.04 | 0.02 | 2.09 | 0.54 | 0.18 |
| | | 13 | 0.11 | 0.04 | 0.02 | 2.06 | 0.52 | 0.17 |
| | | 14 | 0.11 | 0.04 | 0.02 | 2.06 | 0.53 | 0.17 |
| | | 15 | 0.11 | 0.04 | 0.02 | 2.04 | 0.52 | 0.17 |
| *n*-Heptane | 1035 | 1 | 0.09 | 0.01 | 0.00 | 1.52 | 0.20 | 0.03 |
| | | 2 | 0.10 | 0.02 | 0.00 | 1.58 | 0.21 | 0.03 |
| | | 3 | 0.10 | 0.02 | 0.00 | 1.67 | 0.22 | 0.03 |
| | | 4 | 0.09 | 0.01 | 0.00 | 1.43 | 0.19 | 0.03 |
| | | 5 | 0.10 | 0.02 | 0.00 | 1.66 | 0.22 | 0.03 |
| | | 6 | 0.10 | 0.02 | 0.00 | 1.63 | 0.22 | 0.03 |
| | | 7 | 0.10 | 0.02 | 0.00 | 1.61 | 0.21 | 0.03 |
| | | 8 | 0.08 | 0.01 | 0.00 | 1.39 | 0.18 | 0.03 |
| | | 9 | 0.10 | 0.02 | 0.00 | 1.57 | 0.21 | 0.03 |
| | | 10 | 0.09 | 0.01 | 0.00 | 1.51 | 0.20 | 0.03 |
| | | 11 | 0.10 | 0.02 | 0.00 | 1.57 | 0.21 | 0.03 |
| | | 12 | 0.09 | 0.01 | 0.00 | 1.48 | 0.19 | 0.03 |

| | | | | | | | | |
|---|---|---|---|---|---|---|---|---|
| | | 13 | 0.09 | 0.01 | 0.00 | 1.46 | 0.19 | 0.03 |
| | | 14 | 0.09 | 0.01 | 0.00 | 1.52 | 0.20 | 0.03 |
| | | 15 | 0.09 | 0.01 | 0.00 | 1.51 | 0.20 | 0.03 |
| | 290 | 1 | 0.01 | - | - | 0.19 | - | - |
| | | 2 | 0.01 | - | - | 0.21 | - | - |
| | | 3 | 0.01 | - | - | 0.19 | - | - |
| | | 4 | 0.01 | - | - | 0.18 | - | - |
| | | 5 | 0.01 | - | - | 0.21 | - | - |
| | | 6 | 0.01 | - | - | 0.21 | - | - |
| | | 7 | 0.01 | - | - | 0.19 | - | - |
| | | 8 | 0.01 | - | - | 0.21 | - | - |
| | | 9 | 0.01 | - | - | 0.26 | - | - |
| | | 10 | 0.01 | - | - | 0.26 | - | - |
| | | 11 | 0.01 | - | - | 0.23 | - | - |
| | | 12 | 0.01 | - | - | 0.21 | - | - |
| | | 13 | 0.01 | - | - | 0.25 | - | - |
| | | 14 | 0.01 | - | - | 0.16 | - | - |
| | | 15 | 0.01 | - | - | 0.15 | - | - |

# APPENDIX B

# CHAPTER 3 SUPPORTING INFORMATION

# ALKYLPEROXY RADICALS ARE RESPONSIBLE FOR THE FORMATION OF OXYGENATED PRIMARY ORGANIC AEROSOL

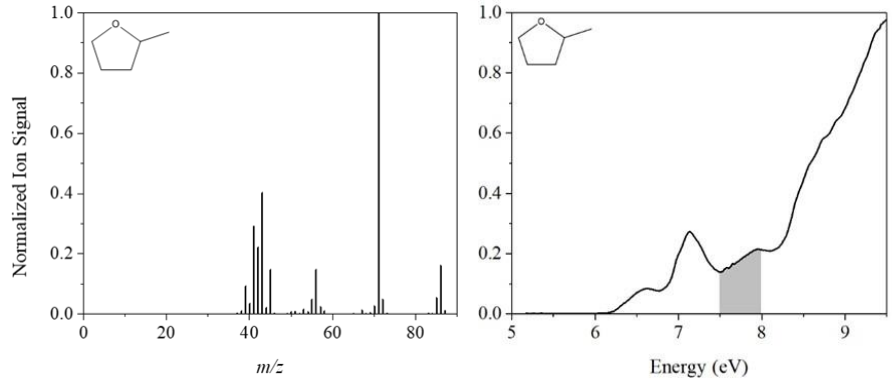


**Figure S3.1.** Normalized mass spectra and corresponding VUV absorption spectra of 2-methyltetrahydrofuran ($C_5H_{10}O$), detected in first-stage combustion of *n*-pentane.

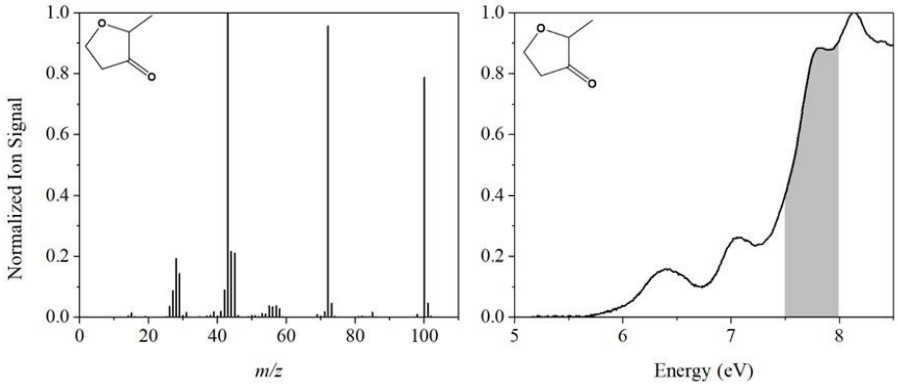


**Figure S3.2.** Normalized mass spectra and corresponding VUV absorption spectra of 2-methyltertahydrofuran-3-one (C5H8O2), detected in first-stage combustion of n-pentane.

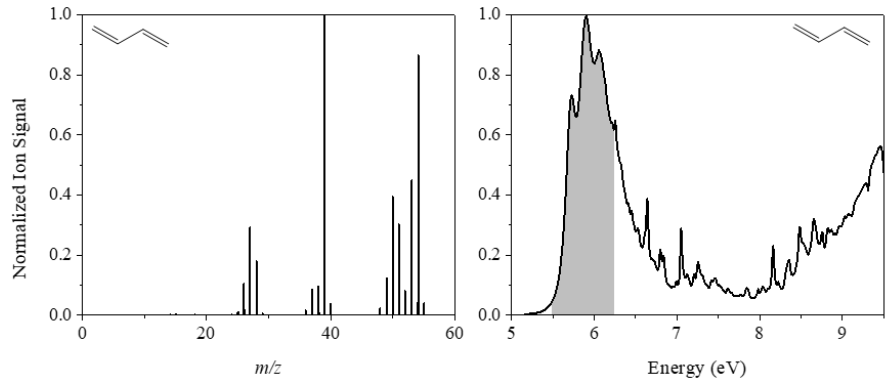


**Figure S3.3.** Normalized mass spectra and corresponding VUV absorption spectra of 1,3-Butadiene ($C_4H_6$), detected in second-stage combustion of *n*-pentane.

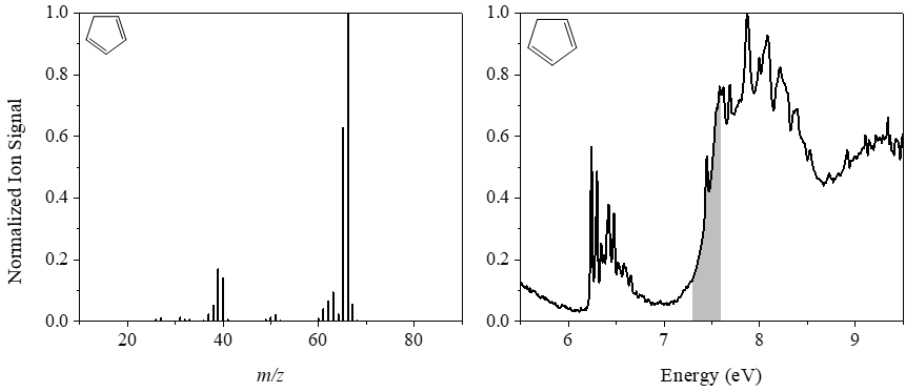


**Figure S3.4.** Normalized mass spectra and corresponding VUV absorption spectra of Cyclopentadiene ($C_5H_6$), detected in second-stage combustion of *n*-pentane.

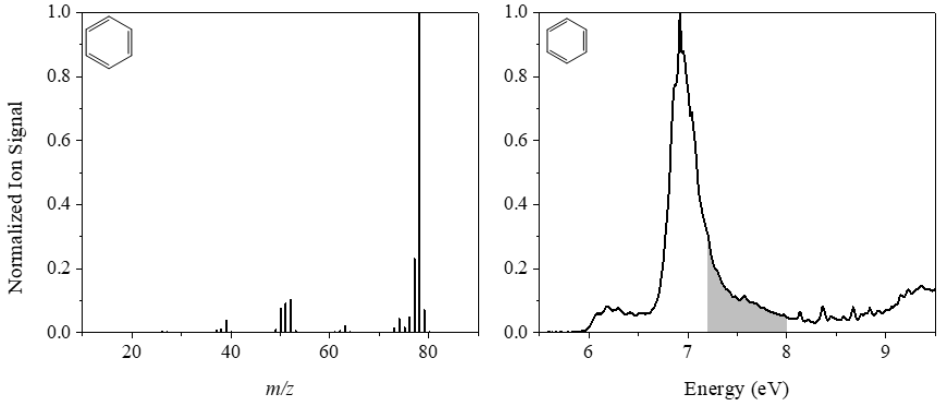


**Figure S3.5.** Normalized mass spectra and corresponding VUV absorption spectra of Benzene ($C_5H_6$), detected in second-stage combustion of *n*-pentane.

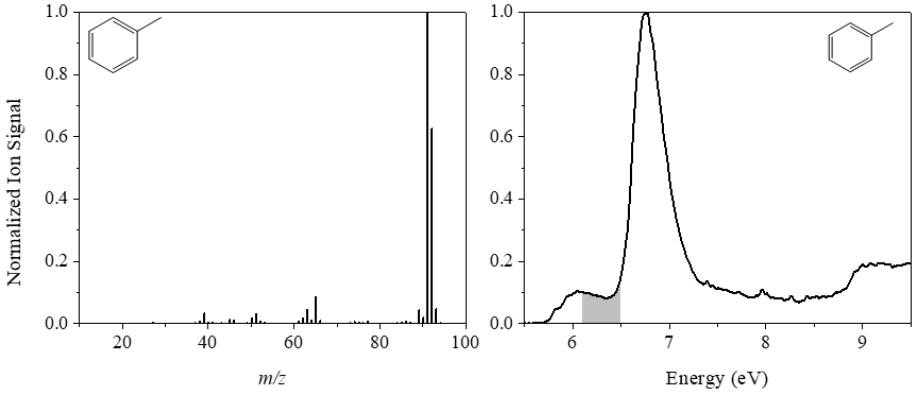


**Figure S3.6.** Normalized mass spectra and corresponding VUV absorption spectra of Toluene ($C_7H_8$), detected in second-stage combustion of *n*-pentane.

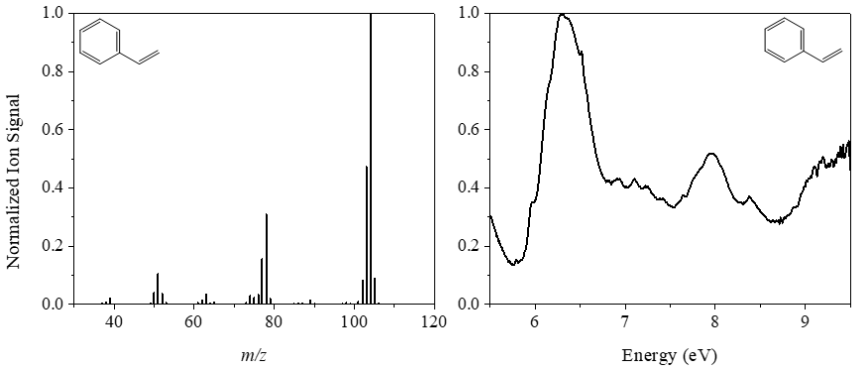


**Figure S3.7.** Normalized mass spectra and corresponding VUV absorption spectra of Styrene ($C_8H_8$), detected in second-stage combustion of *n*-pentane.

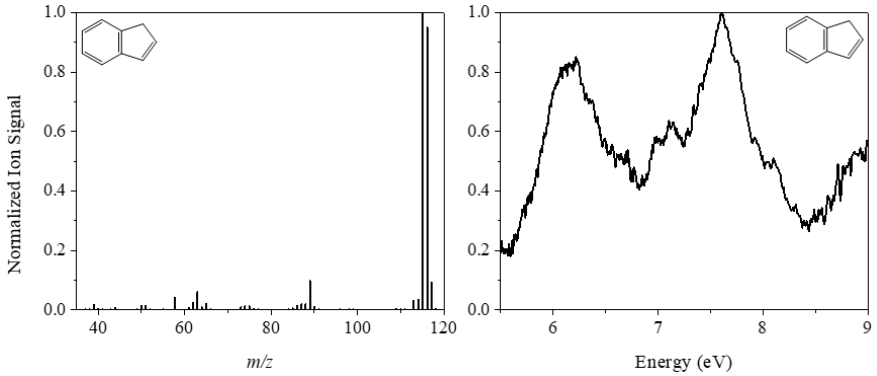


**Figure S3.8.** Normalized mass spectra and corresponding VUV absorption spectra of Indene ($C_9H_8$), detected in second-stage combustion of *n*-pentane.

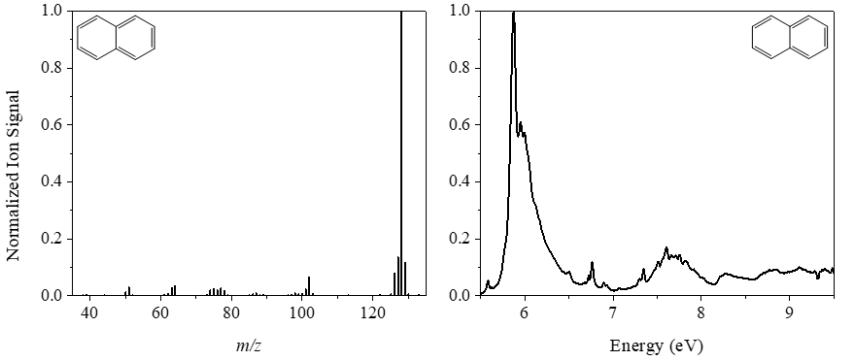


**Figure S3.9.** Normalized mass spectra and corresponding VUV absorption spectra of Naphthalene ($C_{10}H_8$), detected in second-stage combustion of *n*-pentane.

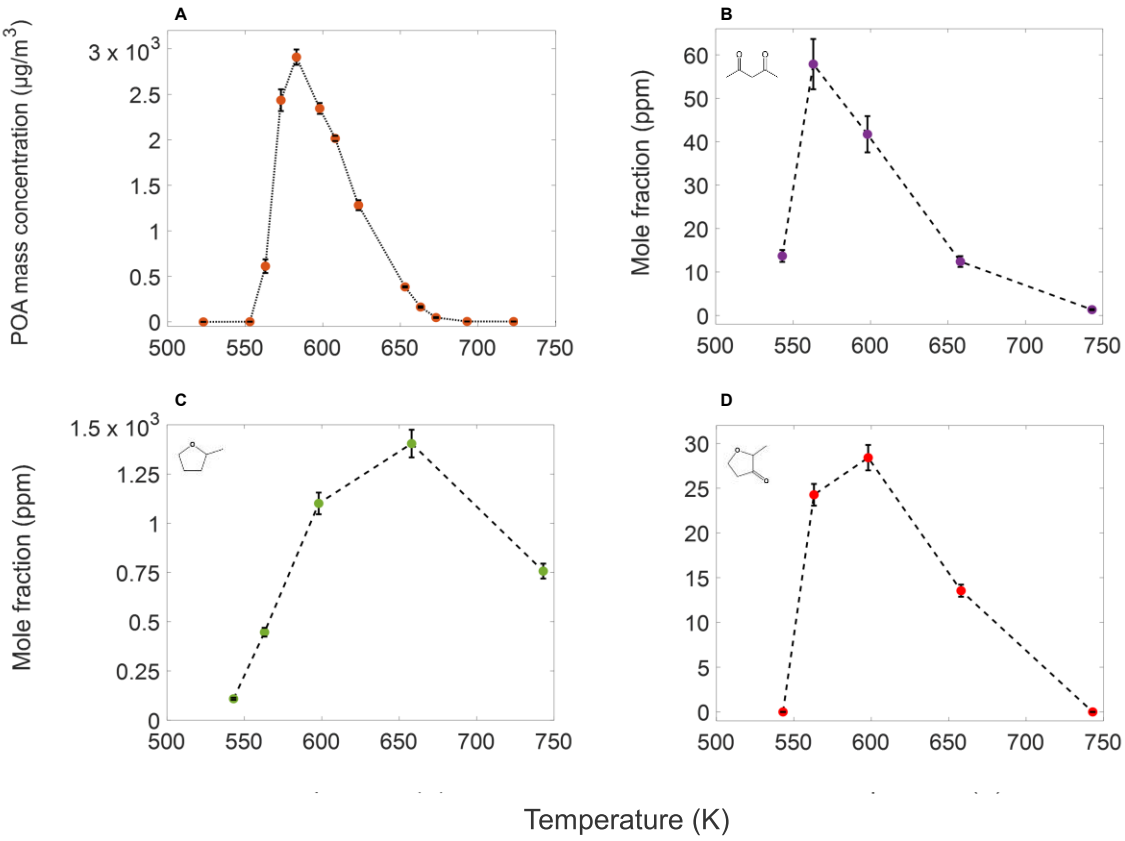


**Figure S3.10.** Temperature-dependent concentration profiles of different species during first-stage combustion. (**A**) OxyPOA. (**B**) Acetylacetone ($C_5H_8O_2$). (**C**) 2-methyltetrahydrofuran ($C_5H_{10}O$). (**D**) 2-methyltertahydrofuran-3-one ($C_5H_8O_2$). For figs. (**B**), (**C**), and (**D**) error bars in concentration of ±10% are applied to account for experimental repeatability and uncertainties in species cross-sections.

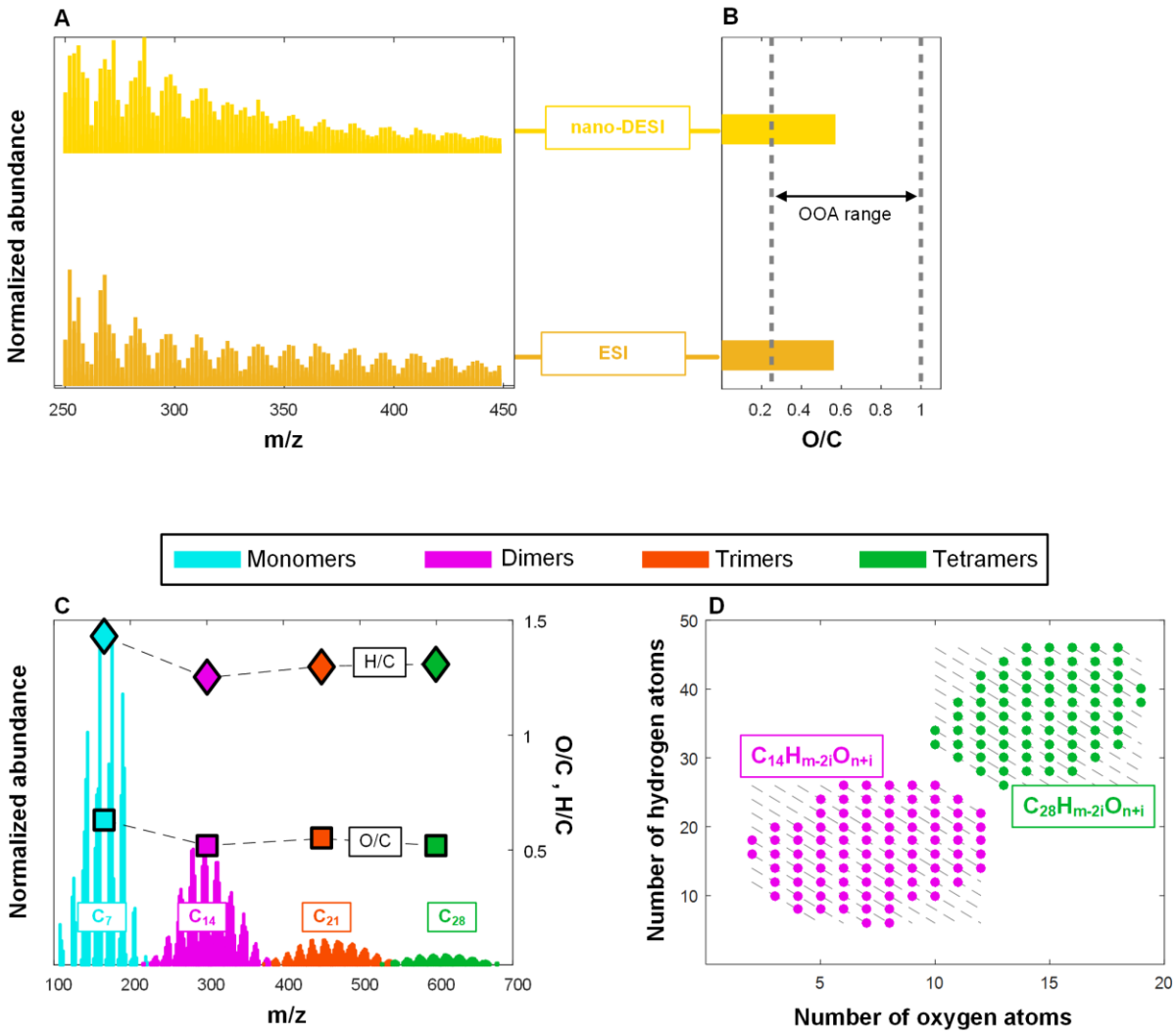


**Figure S3.11.** Mass spectrometry analysis of *n*-heptane OxyPOA. **(A)** Mass spectra obtained using nano-DESI-HRMS (top) and ESI-FTICR-MS (bottom). **(B)** Average O/C of the molecules detected by nano-DESI-HRMS (top) and ESI-FTICR-MS (bottom). **(C)** $C_7$ monomers and oligomers with carbon numbers that are multiples of 7 isolated from the nano-DESI-HRMS spectra. Also shown are the average H/C and O/C of the monomers and the oligomers. **(D)** Number of hydrogen atoms versus number of oxygen atoms of the dimers and tetramers detected by nano-DESI-HRMS.

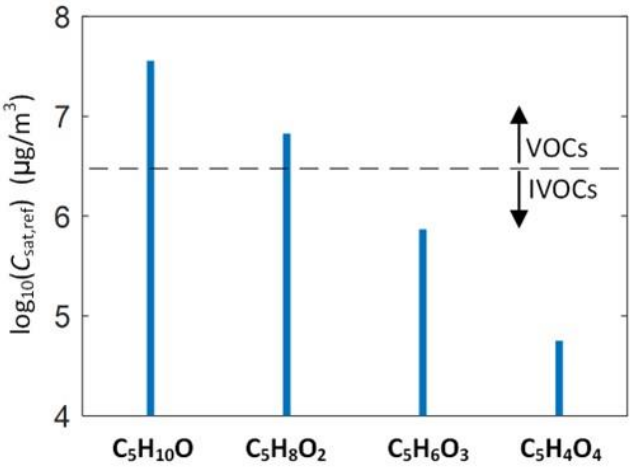


**Figure S3.12.** Saturation concentrations at 300 K ($C_{sat,ref}$) of molecules shown in Fig. 2 of the main text, estimated using the parameterization of Li *et al*. (*83*). Also shown is the cutoff for volatile organic compounds (VOCs) and intermediate-volatility organic compounds (IVOCs). Notably, each oxygen addition leads to a decrease in $C_{sat,ref}$ by an order of magnitude. $C_5H_{10}O$ and $C_5H_8O_2$ were detected in the gas phase in the first-stage *n*-pentane combustion (fig. S3 and fig. S4). $C_5H_4O_4$ had volatility low enough to partition to the particle phase and was detected by ESI-MS. Likely due to its relatively low $C_{sat}$, $C_5H_6O_3$ was not detected in the gas phase, but was also too volatile to appreciably partition to the particle phase.

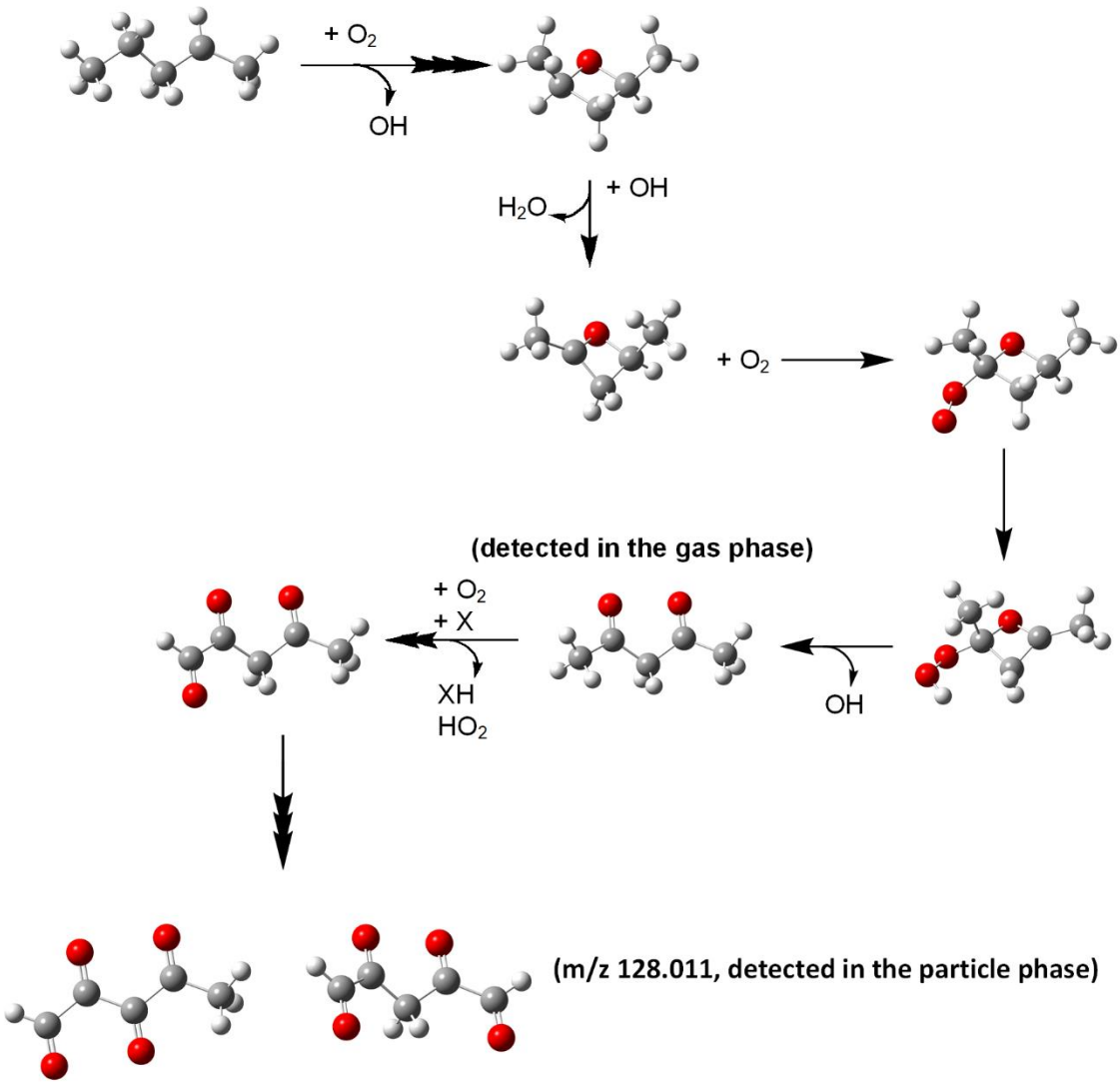


**Figure S3.13.** Reaction pathway to linear, multi-functional intermediates produced from *n*-pentane combustion. $O_2$-addition to of *syn*-2,4-dimethyloxetan-2-yl proceeds through a QOOH-mediated reaction scheme leading via ring-opening to 2,4-pentanedione (*36*). Subsequent H-abstraction reactions of the dicarbonyl yield only resonance-stabilized carbon-centered radicals, e.g. 2,4-pentandion-1-yl, which upon reaction with $O_2$ yields 2,4-dioxopentanedial + $HO_2$. Continued oxidation of the tricarbonyl produces species with sufficiently low volatility leading to the detection of m/z 128.011 ($C_5H_4O_4$) in the particle phase.

# APPENDIX C

## CHAPTER 4 SUPPORTING INFORMATION

## EFFECTS OF FUEL ADDITIVES ON FIRST-STAGE ORGANIC AEROSOLS

To get the volumetric flowrates of air and nitrogen flowing through bubblers, we derived and solved three equations. First equation was derived based on $O_2/N_2$ ratio as following:

$$\left(\frac{P_{sat,n-heptane}}{R_U\,T_{bubbler}}\right)\left(\dot{V}_{n-heptane}\right)^2\left(F_x-1\right)\;+\;F_x\left(\frac{P_{sat,x}}{R_U\,T_{bubbler}}\right)\;\dot{V}_x{}^2\;=\;0 \qquad \text{(S1)}$$

Where $P_{sat}$ is the fuel saturation pressure (kPa) (subscript *x* denotes the additive fuel), $\dot{V}_{n-heptane}$ and $\dot{V}_x$ ($m^3/s$) are the volumetric flowrates of nitrogen passing through the *n*-heptane and additive bubblers, respectively. $F_x$ is the fraction of the blendstock, $R_U$ is the universal gas constant (J/mol·K), and $T_{bubbler}$ is the bubblers' temperature (K). Second equation was derived from the equivalence ratio ($\phi$) combining both fuels as:

$$\left(\frac{P_{sat,n-heptane}}{R_U T_{bubbler}}\right)\dot{V}_{n-heptane}+\left(\frac{P_{sat,x}}{R_U T_{bubbler}}\right)\;-\;0.21*\phi*\left(F/A\right)_{st}*\left(\frac{P_{atm}}{R_U T_{atm}}\right)\;=0 \qquad \text{(S2)}$$

Where $(F/A)_{st}$ is the stoichiometric fuel-to-air ratio for a complete combustion of the two fuel components. The final equation used is the sum of all flowrates exiting the combustion chamber ($\dot{V}_{total}$):

$$\dot{V}_{total}=\;\dot{V}_{n-heptane}+\dot{V}_x+\dot{V}_A+\dot{V}_{N_2} \qquad \text{(S3)}$$

Where $\dot{V}_A$ is the volumetric flowrates of air entering the combustion chamber. For each mixing ratio, we chose the fraction of the additive ($F_x$) while keeping $\phi$, $O_2/N_2$, and $\dot{V}_{total}$ at constant values, then calculated all the required flowrates using the equations above.